

Monolithic integrated dual-wavelength laser for millimeter-wave generation

Citation for published version (APA):

Corradi, A. (2015). *Monolithic integrated dual-wavelength laser for millimeter-wave generation*. [Phd Thesis 1 (Research TU/e / Graduation TU/e), Electrical Engineering]. Technische Universiteit Eindhoven.

Document status and date:

Published: 01/01/2015

Document Version:

Publisher's PDF, also known as Version of Record (includes final page, issue and volume numbers)

Please check the document version of this publication:

- A submitted manuscript is the version of the article upon submission and before peer-review. There can be important differences between the submitted version and the official published version of record. People interested in the research are advised to contact the author for the final version of the publication, or visit the DOI to the publisher's website.
- The final author version and the galley proof are versions of the publication after peer review.
- The final published version features the final layout of the paper including the volume, issue and page numbers.

[Link to publication](#)

General rights

Copyright and moral rights for the publications made accessible in the public portal are retained by the authors and/or other copyright owners and it is a condition of accessing publications that users recognise and abide by the legal requirements associated with these rights.

- Users may download and print one copy of any publication from the public portal for the purpose of private study or research.
- You may not further distribute the material or use it for any profit-making activity or commercial gain
- You may freely distribute the URL identifying the publication in the public portal.

If the publication is distributed under the terms of Article 25fa of the Dutch Copyright Act, indicated by the "Taverne" license above, please follow below link for the End User Agreement:

www.tue.nl/taverne

Take down policy

If you believe that this document breaches copyright please contact us at:

openaccess@tue.nl

providing details and we will investigate your claim.

Monolithic integrated dual-wavelength laser for millimeter-wave generation

Monolithic integrated dual-wavelength laser for millimeter-wave generation

Antonio Corradi

Antonio Corradi

ISBN: 978-90-386-3950-5

Invitation

Monolithic
integrated
dual-wavelength
laser for
millimeter-wave
generation

Monday
2 November 2015
at 16:00

Collegezaal 4
Auditorium TU/e

Antonio Corradi

Monolithic integrated dual-wavelength laser for millimeter-wave generation

PROEFSCHRIFT

ter verkrijging van de graad van doctor aan de Technische Universiteit Eindhoven,
op gezag van de rector magnificus prof.dr.ir. F.P.T. Baaijens,
voor een commissie aangewezen door het College voor Promoties, in het openbaar
te verdedigen op maandag 2 november 2015 om 16:00 uur

door

Antonio Corradi

geboren te Modena, Italië

Dit proefschrift is goedgekeurd door de promotoren en de samenstelling van de promotiecommissie is als volgt:

voorzitter: prof.dr.ir. A.C.P.M. Backx
1^e promotor: prof.dr.ir. M.K. Smit
copromotor(en): dr. E.A.J.M. Bente
leden: prof.dr.ir. P.G.M. Baltus
dr. G. Carpintero del Barrio (Universidad Carlos III de Madrid)
prof.dr. J. Danckaert (Vrije Universiteit Brussel)
prof.dr. D. Lestra
adviseur(s): dr. C. Renaud (University College London)

Het onderzoek of ontwerp dat in dit proefschrift / proefontwerp wordt beschreven is uitgevoerd in overeenstemming met de TU/e Gedragscode Wetenschapsbeoefening.

This research was supported by the European Community's Seventh Framework Program FP7 / 2007-2013 through the iPHOS project and was carried out in the Photonic Integration group (PhI, formerly OED) at the department of Electrical Engineering of the Eindhoven University of Technology.

Monolithic integrated dual-wavelength laser for millimeter-wave generation, by Antonio Corradi

A catalogue record is available at the Eindhoven University of Technology (TU/e) Library

ISBN: 978-90-386-3950-5

Copyright ©2015 Antonio Corradi

Cover design: Antonio Corradi

Printed & Lay Out by: Proefschriftmaken.nl || Uitgeverij BOXPress

Published by: Uitgeverij BOXPress, 's-Hertogenbosch

“Ci sono soltanto due possibili conclusioni: se il risultato conferma le ipotesi, allora hai appena fatto una misura; se il risultato è contrario alle ipotesi, allora hai fatto una scoperta.”

Enrico Fermi

Contents

1	Introduction	1
1.1	Millimeter waves	1
1.2	Dual-wavelength laser and millimeter-wave generation techniques	2
1.3	AWG-based lasers	4
1.3.1	Arrayed waveguide grating	4
1.3.2	Basic AWG-based lasers	6
1.3.3	AWG-based dual-wavelength lasers	6
1.4	AWG-based dual-wavelength laser in iPHOS project	7
1.4.1	Framework of iPHOS project	7
1.4.2	Requirements for the development of dual-wavelength lasers in iPHOS	7
1.4.3	One common SOA for two wavelengths	9
1.5	Thesis outline	11
2	Integration technology	17
2.1	Introduction	17
2.2	Fabrication technology	18
2.2.1	Active-passive wafers	18
2.2.2	Active-passive process flow	20
2.3	Fabrication issues	24
2.3.1	Top InP cladding	25
2.3.2	InGaAsP etch-stop layer	25
2.3.3	Doping in the passive waveguides	25
2.3.4	InP etch-stop layer in the waveguide core	26
2.3.5	Critical dimension loss	26
2.3.6	Planarization	27
2.3.7	Metallization and plating	29
2.4	Cleaving, mounting and wire-bonding of the chips for characterization	31
	Appendix to Chapter 2	34
3	Design choices	41
3.1	Linear laser configuration	41
3.2	Ring laser configuration	43
3.3	Laser model: tuning and power balance control	44
3.4	Monitoring photodetectors and feedback control	48

4	Ring laser	57
4.1	Wafers and active-passive layout	57
4.2	Ring laser design	59
4.3	Components characterizations	64
4.3.1	SOA characterization	64
4.3.2	AWG characterization	66
4.3.3	MZIs and PHMs characterization	67
4.4	Basic characterization of the ring laser	69
4.4.1	Dual-wavelength operation and analysis below threshold	72
4.5	Ring laser analysis	75
4.6	Ring laser linewidth and stability	83
4.7	Conclusions	88
5	Linear laser	91
5.1	Linear laser design	91
5.2	Basic characterization of the linear laser	95
5.2.1	AWG characterization	95
5.2.2	Single mode operation	97
5.2.3	Monitoring PDs	99
5.3	Dual mode operation and stability of the laser	102
5.3.1	Dual mode operation	102
5.3.2	Linewidth and stability of the linear laser	104
5.4	Conclusions	107
6	Conclusions and outlook	109
6.1	Conclusions	109
6.2	Second generation of AWG-based dual-wavelength lasers	112
6.2.1	Configuration A of the second generation device	112
6.2.2	Configuration B of the second generation device	114
6.3	Dual-wavelength laser based on asymmetric Mach-Zehnder interferometers	116
	Summary	119
	Acknowledgments	121
	Curriculum Vitae	125
	Publications	127

CHAPTER 1

Introduction

Abstract – Millimeter wave generation is increasingly attracting attention and efforts both for the possible applications and for the current lack of sources. In this chapter the motivations and the framework of the thesis are described. The state of the art of the optical-based millimeter wave generation techniques is presented. Afterwards, the requirements specified within the iPHOS project for the development of dual-wavelength lasers based on Arrayed Waveguide Grating (AWG) are listed. The choice to design devices with one common Semiconductor Optical Amplifier (SOA) for two longitudinal modes is explained and motivated. Finally, the outline of the thesis concludes the chapter.

1.1 Millimeter waves

The development and deployment of wireless communication systems for a range of applications has been growing together with the need for higher data rates. Wireless data rates have doubled every eighteen months over the last three decades and a further and continuous improvement is required to satisfy future applications [1]. The most straightforward and cost efficient way to achieve higher data rates in wireless communications is to increase the carrier frequency [2]. Higher carrier frequencies will allow for fast transmission of larger amounts of data [1]. The increased directionality and propagation absorption by air and buildings of the high frequency radiation makes the millimeter wave range attractive for point to point secure communications as well as for the development of picocells with high frequency reuse. The fact that these frequency ranges have been released to the public, with well-defined regulations for their use, makes them even more attractive to companies [3].

In this context, industries involved in the development of broadband wireless communication systems have shown great interest in millimeter-wave frequencies (30 GHz - 300 GHz) because these can support short range communications with data rates above 1 Gbit/s [4, 5]. Furthermore, millimeter waves have proven to be promising for many different applications as defense and security [6], spectroscopic and chemical sensing [7], automotive radar [8], and micro-crack detection in concrete structures [9].

Nevertheless, the development of new applications of millimeter waves (mmWs) and terahertz (THz) radiations faces a lack of sources: this frequency range is known in literature as the “terahertz gap” [7]. Product development in the field of millimeter wave generation is still in an early stage compared to the advanced stage of other technologies e.g., microwave and mid-infrared [10]. Because of this, millimeter wave radiation is currently being exploited mainly outside telecommunication applications. This is due to the more stringent requirements on the spectral properties of the radiation in data and telecommunication applications. As the technology develops

and increasingly favorable spectrum policies are being endorsed [11], there is now an opportunity to create essential components, in particular transmitters with low phase noise.

For the generation of millimeter waves, photonic techniques are considered to be superior in terms of tunability and phase noise to conventional electronic techniques based on frequency multiplying chains of microwave oscillators. An additional advantage for the optical system is that optical fibers can be used to transport sub-terahertz signals over long distances [12].

1.2 Dual-wavelength laser and millimeter-wave generation techniques

Several techniques based on photonics to generate millimeter waves have been reported in literature [13]. These methods are all based on generating an optical carrier with amplitude and/or phase modulation at the required millimeter wave frequency. In most systems, this light is then modulated with the data to be transmitted and directed towards a high speed photodiode (Fig. 1.1). The photodiode rectifies the optical signal and the resulting millimeter wave signal can then be amplified electronically and coupled to a transmitting antenna [7]. Although one of the advantages of the photonic approach is the option to use optical amplifiers (replacing the bandwidth limited electronic amplifiers), the possibility to amplify the signal electronically should not be discarded since the power handling and bandwidth of the photodiode used to rectify the signal are generally still an issue considering the state-of-the-art technology.



Fig. 1.1. Block scheme of an optical millimeter wave generator.

We report here the main techniques used in the past to create optical dual-wavelength sources and/or optics based sub-Terahertz generation systems that do not require an RF input and that are suitable for integration on a chip.

1) Mode-locked lasers. Mode-locked lasers have been used successfully to create RF carrier waves. The generation of a 58.8 GHz carrier has been demonstrated exploiting the beating of optical modes on a photodetector [14]. However, in order to obtain improved phase noise characteristics of the RF signal, typically, electro-optic stabilization schemes are required [15]. Although monolithic semiconductor mode-locked laser systems can have excellent phase noise characteristics [16], the tunability of their repetition rate is quite limited, typically up to several percent. This presents an issue in manufacturing mode-locked devices for precisely defined frequencies. With optical mixing of two single frequency lasers (λ_1 and λ_2) a much larger tuning of the amplitude modulation frequency is relatively easy to achieve.

2) Optical mixing of two distributed feedback (DFB) lasers. Two separate laser sources can be mixed in order to obtain an RF carrier wave with a frequency equal to the difference in frequency

between the lasing wavelength of the first laser (λ_1) and that of the second laser (λ_2). This technique provides a wide frequency tuning range. The limitation of this method is that the phase noise of the generated sub-THz signal is determined by the linewidth of the lasers used and, without an external phase noise reduction system, it is typically orders of magnitude larger than purely electrical sources. Therefore, special narrow linewidth lasers need to be used to produce beats of acceptable purity. For high spectral purity and absolute frequency stability, the phase fluctuations of the two lasers need to be correlated. Optical injection phase-lock loop (OIPLL) can be used to lock the slave laser to a master laser modulation sideband. Millimeter wave signal generation with low phase noise (-93 dBc/Hz at 10kHz from the carrier) and large tuning range (4-60 GHz) has been demonstrated, but the technique is complex and the complete system is bulky [17].

3) Monolithic integration of two DFB lasers. Monolithic integration of two laser sources combined by couplers and provided with modulators has the advantage of being a more compact solution than two separate lasers. Furthermore, the two lasers sources on the same chip encounter the same temperature and mechanical fluctuations [18]. Because of this, the frequency difference is inherently more stable. Millimeter-wave generation (146 GHz) and data transmission at 1 Gbit/s have been demonstrated using two free-running DFB lasers monolithically integrated on the same chip [19]. DFB lasers have been chosen for their compactness and their narrow linewidth [18]. Integration of the two lasers allows for devices with more capabilities as well. The integration of two DFB lasers that are in-line and connected through an optical phase modulator has been reported [20]. The center wavelengths of the two lasers are chosen such that their separation is larger than the combined stop bandwidth of the two lasers. As a consequence, both lasers are transparent for each other, which is required for the beat signal generation. Both lasers can be individually tuned in wavelength by integrated heaters. The phase of the mm-wave signal can be controlled by the phase modulator between the two DFB lasers. Dual-wavelength operation with a side mode suppression ratio (SMSR) better than 42 dB and the generation of a tunable (from 210 GHz to 390 GHz) sub-THz carrier wave have been demonstrated with this approach [20]. In a recent study [21], a distributed Bragg reflector (DBR) section is integrated between two DFB lasers. The DBR structure is inserted to create a weak coupling between the two lasers while maintaining each laser in single mode operation. A tunable RF signal from 15 GHz up to 50 GHz with a linewidth of 2.22 MHz has been generated through different combinations of bias currents of the two DFB lasers.

4) Dual-wavelength laterally coupled DFB lasers. Among the various reported configurations, simultaneous emission from two modes within the same laser cavity is very appealing due to its compactness, stability, and spectral quality [22]. One approach is to design a DFB laser with two different grating periods, one on each sidewall [23]. The difference between the periods determines the difference between λ_1 and λ_2 . As a result, the two modes are affected by much the same electrical, thermal and mechanical fluctuations. Stable dual-wavelength operation, with SMSR around 28 dB, has been observed and a 22.5 GHz beat signal has been reported. However, the correlation between the two modes depends on their degree of spatial overlap. In this approach the two modes have different transversal distributions that only partially overlap. As a consequence, the relative power of the two modes in a coupled fiber depends on its position in front of the facet.

5) Dual-wavelength DBR lasers. The common approach of integrating and combine two laser outputs in order to achieve dual-wavelength emission from a single output waveguide can lead to large and complex chip design. Dual-wavelength operation has been reported on asymmetric cladding DBR lasers which exploit two separate uniform gratings operation with fixed mode separations. The different periods of the gratings define the wavelength separation between mode pairs [24]. Two optical modes coexist in the same cavity: only the single gain section has to be biased to produce lasing. Once dual-wavelength operation is achieved by biasing the gain section, injection of current into the front DBR section results in wavelength tuning. Tunable mode pair separations as small as 0.3 nm and as large as 6.9 nm have been achieved [25].

6) Slotted waveguide lasers. A modification can be applied to a multi-wavelength Fabry-Pérot laser by introducing additional reflections in the cavity through the introduction of index variations on the waveguide. These index variations are typically slots in the waveguide ridge. It has been demonstrated that such lasers can be designed and fabricated in such a way that dual-wavelength operation can be achieved. Experimental measurements of a dual-wavelength semiconductor FP lasers with a primary mode spacing in the THz regime have been published. However, theoretical investigations show that the minimum reachable spacing between the two modes is between 460 and 920 GHz [26].

7) Dual-wavelength Arrayed Waveguide Grating based lasers. Instead of grating structures such as DFB lasers or DBRs, AWGs can be used as a wavelength selective element to support two wavelengths in a laser. It has been shown that AWG-based on-chip filtered optical feedback can be used to balance the effective gain of selected longitudinal modes, leading to simultaneous emission of two of them. One advantage of the proposed scheme is that the wavelength selection components are placed outside the laser cavity. However, the SOAs use to select the longitudinal modes are further sources of noise and the laser structure does not allow for continuous tuning. Nevertheless, dual-wavelength operation with a frequency difference of around 1 nm and 2.5 nm has been shown [27, 28]. Dual-wavelength AWG-based lasers have been demonstrated with a performance suitable for sub-THz wave generation. The generation of a 95 GHz signal with 250 kHz linewidth has been demonstrated through the mixing of two modes of an AWG-based laser [29].

In this thesis a specific approach for a dual-wavelength AWG laser is investigated. The AWG-based approach is explained in detail in section 1.4 whereas the principle of operation of this component is explained in section 1.3.1.

1.3 AWG-based lasers

1.3.1 Arrayed waveguide grating

An AWG is a planar device based on an array of waveguides with both imaging and dispersive properties. It can be used as a (de-)multiplexer in telecommunication systems and wavelength-division multiplexing (WDM) networks. The AWG was first reported by Smit [30] and later by Takahashi [31] and Dragone [32]. Although it is known under different names, such as Phased

Array (PHASAR) and Waveguide Grating Router (WGR), the acronym AWG is the most commonly used nowadays. The AWG is exploited frequently in Indium Phosphide technology [33-36] but this component can be fabricated also in several other integration technologies (silica-on-silicon [37], silicon-on-insulator [38], lithium niobate [39], polymer [40]).

A schematic picture of an AWG is shown in Fig. 1.2(a). The basic operating principle is explained in the following. A waveguide is connected to a Free Propagation Region (FPR). When the light propagates from the waveguide into the FPR, it is not laterally confined anymore and the beam becomes divergent. The light at the input aperture is coupled into the waveguide array. Each arrayed waveguide is designed in such a way that the optical path length difference between two adjacent waveguides equals an integer multiple of the central wavelength λ_c of the AWG. The light propagates through the individual arrayed waveguides and reaches the output aperture. Only for the light at λ_c , the fields in the individual waveguides reach the output aperture with the same phase ($2n\pi$ differences where n is an integer number); for this wavelength, the field distribution at the output aperture reproduces the one at the input aperture. In the second FPR, the light becomes convergent and interferes constructively in the image plane. The light at λ_c interferes constructively at the center of the image plane. The linear increase of the length of the arrayed waveguides results in a wavelength-dependent tilt of the beam at the output aperture (dispersion property of the AWG). Consequently, wavelengths different from λ_c interfere constructively at different positions along the image plane. Receiver waveguides placed at proper position along the image plane allow for spatially separating different wavelengths into the corresponding output channels simultaneously [41].

An example of the transmission spectrum of a 4-channel AWG is depicted in Fig. 1.2(b). The difference in frequency between the maxima of two adjacent channels is commonly designed to be a constant and it is called channel spacing (Δf). The response of an AWG is periodic: the period in wavelength (or in frequency) domain is the Free Spectral Range (FSR) of the AWG. Other important parameters of an AWG are the insertion loss and the crosstalk. The insertion loss only affects the efficiency of the laser whereas the crosstalk can have a major impact on the behavior and consequently on the control of the device. The crosstalk is the contribution of undesired signals in a channel i.e., the amount of light coupled in a channel despite the fact that this light has a wavelength different from the ones that ideally should be coupled in the channel. Usually the biggest contribution is the adjacent-channel crosstalk. Further discussion on crosstalk is given in section 4.4.

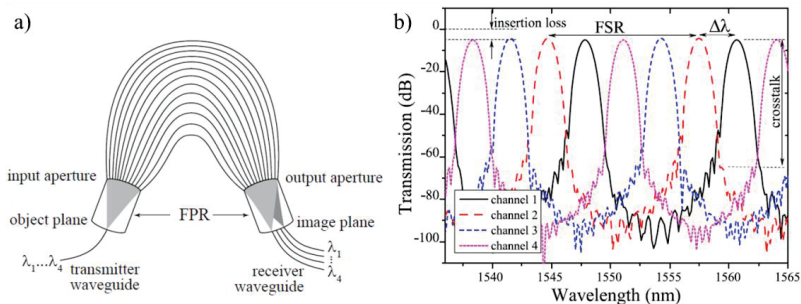


Fig. 1.2. Schematic (a) and transmission spectrum (b) examples of an AWG [36].

1.3.2 Basic AWG-based lasers

In the last decade the AWG has been extensively used in photonic integration. In particular, it is the key component of several tunable lasers [35] and multi-wavelength lasers [36, 42]. Many different configurations have been explored. The most simple and common design of an AWG-laser (AWGL) is reported in Fig. 1.3. It represents a linear laser in which the mirrors of the cavities are formed by the cleaved facets of the chip. An AWG is used as intra-cavity filter. The AWG has two main functions. Firstly, it connects the individual channels to a common channel of the device. Each individual channel is provided with an SOA: when one (or more) SOA(s) is (are) biased, the AWG allows the delivery of light at the available wavelengths (simultaneously) into the same output waveguide. Secondly, the AWG also determines the coarse tuning of the difference between the wavelengths (corresponding to the channel spacing of the AWG). The wavelength selection results from the combination of the transmission spectrum of the AWG, the gain spectrum of the SOA and the laser cavity modes.

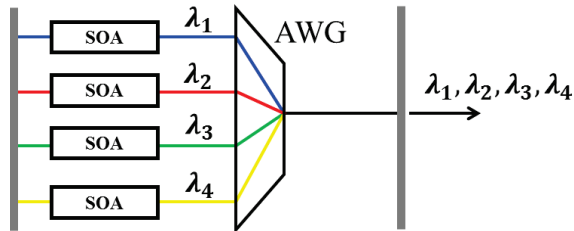


Fig. 1.3. Example of simple schematic of an AWG-based laser.

Many variations to this basic configuration can be made. The reflectivity of the mirrors can be modified, for example, by applying a high reflective (HR) coating to one facet of the chip. Alternatively, different types of on-chip reflectors can be used such as DBRs [43], loop reflectors [44] and multimode interference reflectors (MIR) [45]. Furthermore, ring cavities can be designed.

Different components can be added to the design depending on the requirements and the applications of the AWG-based laser. An SOA can be placed in the common arm or outside the laser cavity in order to increase the output power [36]. Phase-shifters can be placed, for example, in the individual channels of the laser in order to fine tune the lasing mode. Multi-Mode Interferometers (MMIs) can be used to split the light into different waveguides and manipulate it separately or to combine individual channels.

1.3.3 AWG-based dual-wavelength lasers

Fig. 1.3 shows the schematic of an AWG laser in which four individual channels provided with SOAs are combined through the intra-cavity AWG in a common output arm (provided with SOA too). While simultaneously biasing the SOAs in the individual channels, dual-wavelength operation can be achieved and a dual-wavelength spectrum can be observed from the common output waveguide. This approach has been used to demonstrate the generation of a 95 GHz signal (with 250 kHz linewidth) by mixing the two modes on a photodiode [29]. In that case, an SOA has been

added to the common arm in order to increase the output power. However, since this common SOA is inside the laser cavity, it also affects the behavior of the laser and it reduces the stable dual-wavelength operation regions due to competition of the two modes in the common SOA [12].

1.4 AWG-based dual-wavelength laser in iPHOS project

1.4.1 Framework of iPHOS project

The interest in microwave photonic technologies is especially strong in relation to a growing number of applications utilizing the millimeter wave frequency range (30 – 300 GHz) [46]. Pushing the boundaries in millimeter wave wireless applications was the objective of the European Commission funded project iPHOS (Integrated photonic transceivers at sub-terahertz wave range for ultra-wideband wireless communications). This project connected photonic-enabled millimeter wave technologies and photonic integration efforts to support advanced wireless communications in the E-band (60 - 90 GHz) and F-band (90 - 140 GHz). The aim of the project is to explore the possibilities of development of a compact and low-cost system for the generation and the transmission of millimeter waves. Thus, the project tasks include the realization of dual-wavelength laser sources, a fast-photodiode for mixing the two modes, an antenna to send the generated millimeter wave signal, an antenna to receive the signal and a Schottky diode for decoding the data.

In the project, led by Universidad Carlos III De Madrid, the following partners were involved: University College London, University of Cambridge, III-V Labs, Universität Duisburg-Essen, Technische Universität Berlin, ACTS, and Thales Systèmes Aéroportés.

The first application field targeted by iPHOS is future on-board flight entertainment systems, an effort led by partner Thales. Nevertheless, the iPHOS impact strategy includes channeling the designs and devices obtained through licensing design libraries within the European manufacturing platforms of JePPIX, opening up the possibility for other companies and consortiums to incorporate the mmW sources in other fields of applications.

In the framework of iPHOS project, Eindhoven University of Technology had the tasks of developing and fabricating dual-wavelength laser sources based on an AWG. As discussed previously, the straight-forward solution of combining two discrete single-wavelength laser sources does not produce a beat tone of sufficient purity, requiring the use of stabilization schemes to reduce the linewidth. This is mainly due to the linewidth of the two uncorrelated laser signals and to the relative wavelength fluctuation between them. The approach required by the project is to fabricate a monolithically integrated dual-wavelength laser source.

1.4.2 Requirements for the development of dual-wavelength lasers in iPHOS

As a partner in the iPHOS project, Eindhoven University of Technology had the task to explore the feasibility of realizing monolithically integrated AWG-based dual-wavelength lasers suitable for millimeter wave generation. The goal was then to design and fabricate on an active/passive InP chip, a laser which can deliver simultaneously two lasing modes from the same output waveguide. Furthermore, the device had to exploit the filter function of an AWG.

The target frequency differences between the two lasing wavelength (the frequencies of the mm-waves that can be generated by beating the two modes) are 70 GHz and 120 GHz. We have designed and fabricated devices aiming for both frequencies.

The laser must be suitable for the generation of sub-THz carrier waves through mixing of the two lasing modes on a fast photodiode. The most important requirement for the generation of millimeter waves is the phase noise of the generated signal which determines the purity of the carrier wave. The target phase noise performance < -90 dBc/Hz at 100 kHz offset from the millimeter wave signal is specified in the Description of Work of iPHOS project [47].

If the two modes at λ_1 and λ_2 are generated by two independent lasers, the linewidth of the output millimeter wave is determined by the sum of the linewidth of these modes [29]. In a mixing configuration which utilizes two DFB lasers, an opto-electronic phase-locking system is needed to increase the frequency stability of the generated millimeter wave [17]. An example is reported in [7]: without any further stabilization, the phase noise of the DFB-mixing millimeter wave source is -75 dBc/Hz at an offset frequency of 100 MHz and the frequency drift is more than 10 MHz/hour.

In order to fulfill the phase noise requirement, an Optical Phase Locked Loop (OPLL) based stabilization technique has been proposed within the iPHOS consortium by University College London. In this OPLL, the mmW signal generated on the photodiode is mixed with a higher harmonic signal from a stable electronic RF generator. The mixing product is then used to derive a control signal for the optical frequency of one of the DFB lasers. The target phase error variance is 0.03 rad² [47, 48]. For a simulation implemented to show that the target can be achieved with this technique, it is assumed that λ_1 and λ_2 are generated by two independent lasers and that the sum of the two optical linewidths is 0.5 MHz. In Fig. 1.4, which originates from deliverable D4.3 of iPHOS project [47, 48], the phase noise spectral density of the free-running lasers (summed linewidth) is compared with the one that can be obtained with a first-order OPLL.

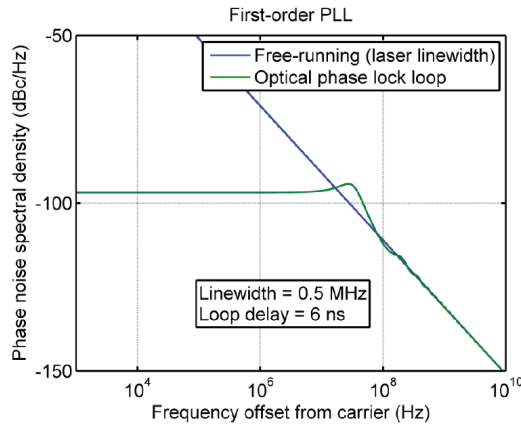


Fig. 1.4. Phase noise spectral density for a summed linewidth of 0.5 MHz (blue line) and with a first-order OPLL-based stabilization technique (green line). Figure is from Deliverable D4.3[48] of iPHOS project and it is reproduced here with the kind permission of Dr. Martyn Fice from University College of London who is the author of the graph.

Using such a stabilization technique, the maximum phase noise spectral density associated with the Lorentzian linewidth is expected to be below -90 dBc/Hz at 100 kHz. However, in case the low-frequency phase noise is non-Lorentzian, the phase noise spectral density at frequencies below 100 kHz would be higher. For the specific case reported in Fig. 1.4, the required loop gain is 123 Mrad/s, the loop delay is 6 ns and the loop noise bandwidth is 70 MHz [48, 49].

1.4.3 One common SOA for two wavelengths

The basic idea behind the work presented here is to investigate photonic integrated dual-wavelength lasers in which the frequency fluctuations of the two wavelengths λ_1 and λ_2 are correlated. This can be obtained using a dual-wavelength laser in which both wavelengths are generated and amplified by one common semiconductor optical amplifier (SOA). Being amplified by the same SOA, the two modes share the same variations caused by changes in refractive index due to changes in temperature and variations in carrier concentration. The carrier concentration fluctuations are due to intensity variations in the laser as well as fluctuations in the electrical current supplied. As a consequence, the variations in the laser longitudinal cavity mode structure for each of the two modes are strongly correlated. The instantaneous deviations in frequency of λ_1 and λ_2 due to thermal changes and changes in the carrier density can be close to identical if the laser cavity length for both laser modes is similar.

The physical limit for the linewidth of semiconductor lasers at full-width half-maximum (FWHM) is given by a modified Schawlow Townes [50] formula, as first demonstrated by Henry [51]:

$$\Delta\nu_{laser} = \frac{\pi h\nu(\Delta\nu_c)^2}{P_{out}}(1 + \alpha^2) \quad (1.1)$$

where: h is the Planck constant, ν is the central frequency of the laser, $\Delta\nu_c$ is the bandwidth of the laser cavity, P_{out} is the output power of the laser and α is the linewidth enhancement factor. The 1 in the term in brackets originates directly from the spontaneous emission in the amplifier which adds to the total field in the cavity. The term α^2 is due to the coupling between the gain and the refractive index in the amplifier [52]. Spontaneous emission events produce fluctuations in the light intensity in the cavity and therefore in the gain, resulting finally in fluctuations of the refractive index in the amplifier. The consequence of this is a phase change in the optical fields [51]. These phase changes are slightly different for the two wavelengths and they affect the mode frequency of the cavities for λ_1 and λ_2 . If the cavity length is the same for both modes, then the frequency variations of the two wavelengths will be smaller by approximately a factor of $(\lambda_1 - \lambda_2) / \lambda_1$ (assuming $(\lambda_1 - \lambda_2) / \lambda_1 \ll 1$). Most lasers operate far above the fundamental Schawlow-Townes limit because the technical noise generated by other sources (such as the current supply or mechanical vibrations) dominates the system. In principle, the contribution to the enlargement of the linewidth given by the factor α^2 and many of the contributions from the technical noise are nearly equal for λ_1 and λ_2 when the two wavelengths are amplified at the same time by the same SOA.

In order to achieve simultaneous lasing on two modes with wavelengths λ_1 and λ_2 supported by a single SOA, accurate control of the roundtrip loss in the cavity is required. As it is shown below, the requirement on the power ratio between the two wavelengths to have high mmW output power

is not particularly strict. The total electric field of the superposition of two longitudinal modes on the mixing photodiode is:

$$E_{tot} = A_1 \sin(2\pi ft) + A_2 \sin(2\pi ft + 2\pi\Delta ft) \quad (1.2)$$

where A_1 and A_2 are the amplitudes of the electric fields of the two modes, f is the frequency of the first mode and Δf is the frequency difference between the two modes. In the photodiode, the carrier generation depends on the optical power which is described by the envelope of E_{tot} :

$$\langle E_{tot} \rangle^2 = \langle [A_1 \sin(2\pi ft) + A_2 \sin(2\pi ft + 2\pi\Delta ft)]^2 \rangle \quad (1.3)$$

In this equation the $\langle E_{tot} \rangle$ operator stands for a time average over an optical cycle. The square term can be expanded to:

$$\langle E_{tot} \rangle^2 = \langle A_1^2 \sin^2(2\pi ft) + A_2^2 \sin^2(2\pi ft + 2\pi\Delta ft) + 2A_1A_2 \sin(2\pi ft) \sin(2\pi ft + 2\pi\Delta ft) \rangle \quad (1.4)$$

In equation (1.4) the product term can be rewritten to the sum of two cosines:

$$\langle E_{tot} \rangle^2 = \langle A_1^2 \sin^2(2\pi ft) + A_2^2 \sin^2(2\pi(f + \Delta f)t) - 2A_1A_2 \cos(2\pi(2f + \Delta f)t) + 2A_1A_2 \cos(2\pi\Delta ft) \rangle \quad (1.5)$$

The cycle average over the first three terms leads to a DC term that corresponds to the DC current in the photodiode. The modulation depth of the carrier generation in the photodiode is then determined by the last term $2A_1A_2 \sin(2\pi\Delta ft)$. Therefore, the AC current at the frequency Δf is proportional to the product of the intensities of the electric fields of the two waves A_1A_2 . This product corresponds to:

$$A_1A_2 = \sqrt{P_1}\sqrt{P_2} \quad (1.6)$$

where P_1 and P_2 are the power of the first and the second mode respectively. The total output power provided by the dual-mode laser system, indicated with P_{tot} , does not depend on the distribution between the two modes. If we set P_{tot} to the unit value (100%) we can write:

$$P_{tot} = P_1 + P_2 \quad \text{and} \quad R = P_1/P_2 \quad (1.7)$$

where R is the ratio between the power of the two modes. P_1 and P_2 can then be written in terms of R :

$$P_1 = \frac{P_{tot}}{1+1/R} \quad \text{and} \quad P_2 = \frac{P_{tot}}{1+R} \quad (1.8)$$

In the ideal case, P_{tot} is equally divided between P_1 and P_2 ($R = 1$). Consequently, if P_{tot} is set to 1, the product of A_1A_2 is:

$$A_1A_2 = \sqrt{P_1}\sqrt{P_2} = 0.5 \quad (1.9)$$

However, if P_1 is twice as large as P_2 ($R = 2$), then the product of A_1A_2 becomes:

$$A_1A_2 = \sqrt{P_1}\sqrt{P_2} = 0.471 \quad (1.10)$$

which is equal to 94% of the value of A_1A_2 when $P_1 = P_2$. In other words, a 3 dB difference between the power of λ_1 and λ_2 leads to a difference frequency modulation depth of 94% of the modulation depth at the ideal power ratio of 1.

A consequence of the power balance requirement is that part of the cavity for λ_1 must be separated from the cavity for λ_2 . A control system must be added to the parts of the cavities which are not shared in order to be able to control independently the losses of the cavities and consequently the power of λ_1 and λ_2 . Of course, this control system introduces a technical noise source which is different for the two wavelengths, thus, keeping any technical noise originating from these parts at a minimum is critical.

The fact that two modes share a common SOA can lead to instabilities. There are theoretical predictions that even if the laser cavity allows dual-mode lasing operation, the gain medium nonlinearity can forbid simultaneous emission of the two modes. According to Chusseau [53] a stable dual-wavelength regime is possible only when the coupling factor between the modes is weak enough. The physical origin of the mode coupling is the short intraband relaxation time that strongly couples the carrier populations [53]. The quantum well (QW) based laser model presented by Chusseau shows that dual-wavelength operation can only occur in a small range of applied injection currents and temperatures. Therefore, Chusseau et al. suggest that stable dual-wavelength operation can most likely not be achieved experimentally if the two modes are separated by less than the homogeneous linewidth of the gain medium which is approximately 1.6 THz [53, 54]. In the same studies, the use of a quantum dot (QD) based gain material is proposed to overcome the problem because of weaker mode coupling between quantum dots.

In this thesis, the choice to work with QW gain material is explained in section 4.1. An important result in this thesis is therefore the demonstration of experimental dual-mode operation of QW based devices with a single SOA. This is presented in sections 4.4.1 and 5.3.1.

1.5 Thesis outline

The outline of the chapters in the thesis that follow this introduction is described below:

- In **Chapter 2**, the active-passive integration technology process used to fabricate the devices presented in Chapters 4 and 6 of this thesis is explained. The fabrication is based on the standardized generic integration technology developed at COBRA. Minor variations that were made to the standardized process flow are discussed. The last section of Chapter 2 describes the mounting and the wire-bonding of the chips implemented in order to simplify the characterization of the devices in the lab.
- In **Chapter 3**, the main design choices for the devices presented in Chapter 4 and Chapter 5 are presented. Both linear and ring configurations are discussed. The advantages of exploiting an AWG as intra-cavity filter are listed. Constructions based on voltage controlled electro-optic phase modulators are used for fine tuning and for controlling the power of the two modes. On chip photodetectors are designed to monitor the power of λ_1 and λ_2 . A feedback control circuit which exploits the signals extracted from the photodetectors is proposed.

- A series of dual mode ring lasers has been designed based on the calculations presented in Chapter 3 and has been fabricated by the author. In **Chapter 4**, we focus on the experimental results obtained from one of these dual mode ring lasers. In order to analyze the performance of the laser it was necessary to develop the theoretical description of the laser further.
- A linear AWG-based dual wavelength laser has been designed and fabricated in a Multi-Project Wafer run. **Chapter 5** focuses on the characterization results of this linear laser. Dual wavelength operation is demonstrated. The advantages and disadvantages of this configuration compared to the ring laser presented in Chapter 4 are described and discussed.
- In **Chapter 6**, the results obtained from the devices presented in Chapter 4 and 5 are summarized. Two design configurations of new generation AWG-based devices are presented. The goal of the new generation devices is to combine the advantages of the linear and the ring laser presented in the previous chapters. Finally, an alternative design based on asymmetric MZIs instead of an AWG is presented.

References

- [1] T. Kleine-Ostmann and T. Nagatsuma, "A review on terahertz communications research", *Journal of Infrared Millimeter and Terahertz Waves*, vol. 32, no. 2, pp. 143-171, 2011.
- [2] A. Hirata, T. Kosugi, H. Takahashi, R. Yamaguchi, F. Nakajima, T. Furuta, H. Ito, S. Member, H. Sugahara, Y. Sato, and T. Nagatsuma, "120-GHz-band millimeter-wave photonic wireless link for 10-Gb/s data transmission", *IEEE transactions on microwave theory and techniques*, vol. 54, no. 5, May 2006.
- [3] Prasanna Adhikari, "Understanding Millimeter Wave Wireless Communication", White Paper, Loea Corporation, 2008.
- [4] G. Fettweis, "WIGWAM: System concept for 1Gbit/s and beyond", IEEE 802 plenary meeting, November 2005.
- [5] C.C. Chong, K. Hamaguchi, P.F.M. Smulders, and S.K. Yong, "Millimeter-wave wireless communication systems: theory and applications", *EURASIP Journal on Wireless Communications and Networking*, 2007.
- [6] R. Appleby and C. Cameron, "Seeing hidden objects with millimeter waves", *Physics World*, pp. 35-39, January 2012.
- [7] T. Nagatsuma, H. Ito, and T. Ishibashi, "High-power RF photodiodes and their applications", *Laser & Photon. Rev.* 3, No. 1-2, pp. 123-137, 2009.
- [8] H. Iizuka, K. Sakakibara, T. Watanabe, K. Sato, and K. Nishikawa, "Millimeter-wave microstrip array antenna with high efficiency for automotive radar systems", *R&D Review of Toyota CRDL*, vol. 37, no. 2 pp. 7-12, 2002.
- [9] S. Oka S. Mochizuki, H. Togo, and N. Kukutsu, "Inspection of concrete structures using millimeter-wave imaging technology", *NTT Technical review*, vol. 7, no. 3, pp. 1-6, March 2009.
- [10] H.B. Liu, H. Zhong, N. Karpowicz, Y. Chen, and X.C. Zhang, "Terahertz spectroscopy and imaging for defense and security applications", *Proceedings of the IEEE*, vol. 95, no. 8, pp. 1514-1527, August 2007.
- [11] US Federal Communications Commission, "Allocations and service rules for the 71-76 GHz, 81-86 GHz and 92-95 GHz bands", 69 FR 3257, pp. 3257-3268, January 2004.
- [12] G. Carpintero, K. Balakier, Z. Yang, R.C. Guzmán, A. Corradi, A. Jimenez, G. Kervella, M.J. Fice, M. Lamponi, M. Chitoui, F. van Dijk, C.C. Renaud, A. Wonfor, E.A.J.M. Bente, R.V. Penty, I.H. White, and A.J. Seeds, "Microwave photonic integrated circuits for millimeter-wave wireless communications", *Journal of Lightwave technology*, vol. 32, no. 20, pp. 3495-3501, August 2014.

-
- [13] T. Nagatsuma, A. Hirata, N. Shimizu, H.J. Song, and N. Kukutsu, "Photonic Generation of Millimeter and Terahertz Waves and Its Applications", 19th Int. Conf. on Applied Electromagnetics and Communications (ICECom), 2007.
- [14] A. Stöhr, S. Babieli, P.J. Cannard, B. Charbonnier, F. van Dijk, S. Fedderwitz, D. Moodie, L. Pavlovic, L. Ponnampalam, C.C. Renaud, D. Rogers, V. Rymanov, A. Seeds, A.G. Steffan, A. Umbach, and M. Weiss, "Millimeter-wave photonic components for broadband wireless systems", IEEE transactions on microwave theory and techniques, vol. 58, no. 11, November 2010.
- [15] Van-Dijk, F.; Enard, A.; Akrouf, A.; Guang-Hua Duan; Lelarge, F., "Optimization of a 54.8 GHz coupled opto-electronic oscillator through dispersion compensation of a mode-locked semiconductor laser", International topical meeting on Microwave photonics, 2008; jointly held with the 2008 asia-pacific microwave photonics conference. mwp/apmp 2008; pp.279-282, Sept. 9 2008-Oct. 3 2008.
- [16] D. Mandridis, I. Ozdur, F. Quinlan, M. Akbulut, J.J. Plant, P.W. Juodawlkis, and P.J. Delfyett, "Low-noise, low repetition rate, semiconductor-based mode-locked laser source suitable for high bandwidth photonic analog-digital conversion", Applied Optics, vol. 49, no. 15, pp. 2850-2857, 2010.
- [17] L.A. Johansson and A.J. Seeds, "Generation and transmission of millimeter-wave data-modulated optical signals using an optical injection phase lock loop", Journal of Lightwave Technology, vol. 21, no. 2, pp. 511-520, February 2003.
- [18] F. van Dijk, A. Accard, A. Enard, O. Drisse, D. Make, F. Lelarge, "Monolithic dual wavelength DFB lasers for narrow linewidth heterodyne beat-note generation", Proceedings of the 2011 IEEE MWP.
- [19] M.J. Fice, E. Rouovalis, F. van Dijk, A. Accard, F. Lelarge, C.C. Renaud, G. Carpintero, and A.J. Seeds, "146-GHz millimeter-wave radio-over-fiber photonic wireless transmission system", Optics express, vol. 20, no. 2, January 2012.
- [20] T. Göbel, D. Stanze, R.J.B. Dietz, H. Roehle, M. Schlak, B. Sartorius and M. Schell, "Next generation continuous wave photomixing THz system", 36th International Conference on Infrared, Millimeter and Terahertz Waves (IRMMW-THz), October 2011.
- [21] Y.-H. Lo, Y.-C. Wu, S.-C. Hsu, Y.-C. Hwang, B.-C. Chen, and C.-C. Lin, "Tunable microwave generation of a monolithic dual-wavelength distributed feedback laser", Optics Express, vol. 22, no. 11, June 2014.
- [22] M. Tani, O. Morikawa, S. Matsuura and M. Hangyo, "Generation of terahertz radiation by photomixing with dual- and multiple-mode lasers", Semiconductor Science and Technology, vol. 20, no. 7, pp.S151-S163, 2005.
- [23] F. Pozzi, R.M. De La Rue, and M. Sorel, "Dual-wavelength InAlGaAs-InP laterally coupled distributed feedback laser", IEEE PTL, vol. 18, no. 24, December 2006.
- [24] S.D. Roh, K.E. Lee, J.S. Hughes, and J.J. Coleman, "Single and tunable dual-wavelength operation of an InGaAs-GaAs Ridge Waveguide Distributed Bragg Reflector Laser", IEEE Transactions on photonics letters, vol. 12, no. 1, January 2000.
- [25] S.D. Roh, T.S. Yeoh, R.B. Swint, A.E. Huber, C.Y. Woo, J.S. Hughes, and J.J. Coleman, "Dual-wavelength InGaAs-GaAs ridge waveguide distributed Bragg reflector lasers with tunable mode separation", IEEE PTL, vol. 12, no. 10, October 2000.
- [26] S. O'Brien, S. Osborne, K. Buckley, R. Fehse, A. Amann, E. P. O'Reilly, L. P. Barry, P. Anandarajah, J. Patchell, and J. O'Gorman, "Inverse scattering approach to multiwavelength Fabry-Perot laser design", Phys. Rev. A, vol.74, no. 6, December 2006.
- [27] M. Khoder, G. Verschaffelt, R. M. Nguimbo, J. Bolk, X. J. M. Leijtens, and J. Danckaert, Digitally tunable dual wavelength emission from semiconductor ring lasers with filtered optical feedback, Laser Phys. Lett. 10, 2013.
- [28] M. Khoder, G. Verschaffelt, R. M. Nguimbo, J. Bolk, X. J. M. Leijtens, and J. Danckaert, Controlled multi-wavelength emission using semiconductor ring lasers with on-chip filtered optical feedback, Opt. Lett. 38, 2608-2610, 2013.

- [29] G. Carpintero, E. Rouvalis, K. Lawniczuk, M. Fice, C.C. Renaud, X.J.M. Leijtens, E.A.J.M. Bente, M. Chitoui, F. van Dijk, and A.J. Seeds, "95 GHz millimeter wave signal generation using an arrayed waveguide grating dual wavelength semiconductor laser", *Optic Letters*, vol. 37, no. 17, September 2012.
- [30] M. Smit, "New focusing and dispersive planar component based on an optical phased array", *Electronics Letters*, vol. 24, no. 7, pp. 385-386, March 1988.
- [31] H. Takahashi, S. Suzuki, K. Kato, and I. Nishi, "Arrayed-waveguide grating for wavelength division multi/demultiplexer with nanometer resolution", *Electronics Letters*, vol. 26, pp. 87-88, January 1990.
- [32] C. Dragone, "An $N \times N$ optical multiplexer using a planar arrangement of two star couplers", *IEEE Photon. Technol. Lett.*, vol. 3, pp. 812-815, September 1991.
- [33] C. van Dam, "InP-based polarization independent wavelength demultiplexers", PhD thesis, Delft University of Technology, The Netherlands, 1997.
- [34] Y. Barbarin, X. Leijtens, E. Bente, C. Louzao, J. Kooiman, and M. Smit, "Extremely small AWG demultiplexer fabricated on InP by using double-etch process," in *Tech. Digest Integr. Photon. Res. (IPR '04)*, p. IThG4, San Francisco, USA, June-July 2004.
- [35] B.W. Tilma, "Integrated tunable quantum-dot laser for optical coherence tomography in the 1.7 μm wavelength region," PhD thesis, Technische Universiteit Eindhoven, The Netherlands, 2011.
- [36] K. Ławniczuk, "Multiwavelength transmitters in generic photonic integration technologies," PhD thesis, Technische Universiteit Eindhoven, The Netherlands, 2014.
- [37] C. Richard Doerr and K. Okamoto, "Advances in Silica Planar Lightwave Circuits," *Journal of Lightwave Technology*, Vol. 24, No. 12, December 2006.
- [38] P. Dumon, W. Bogaerts, D. Van Thourhout, G. Morthier, R. Baets, P. Jaenen, S. Beckx, J. Wouters, T. Farrell, N. Ryan, E. Grivas, E.; Kyriakis-Bitzaros, E.; Halkias, G.; McKenzie, I., "A nanophotonic 4 x 4 wavelength router in silicon-on-insulator," *Optical Fiber Communication Conference, 2006 (OFC '06)*, 5-10 March 2006.
- [39] H. Okayama and M.Kawahara, "Waveguide array grating demultiplexer on LiNbO_3 ," in *Technical Digest Integr. Photon. Res. (IPR '95)*, pp. 296-298, Dana Point, CA, 1995.
- [40] M. Diemeer, L. Spiekman, R. Ramsamoedj, and M. Smit, "Polymeric phased array wavelength multiplexer operating around 1550 nm," *Electron. Lett.*, vol. 32, pp. 1132-1133, June 1996.
- [41] Xaveer J. M. Leijtens, Berndt Kuhlow and M.K. Smit, "Arrayed Waveguide Gratings," chapter 4 in D.H. Venghaus ed., *Wavelength Filters in Fibre Optics*, Springer Berlin Heidelberg, 2006.
- [42] J.H. den Besten, "Integration of Multiwavelength Lasers with Fast Electro-Optical Modulators," PhD thesis, Technische Universiteit Eindhoven, The Netherlands, 2004.
- [43] B. Docter, "Deeply-etched DBR mirrors for photonics integrated circuits and tunable lasers," PhD thesis, Technische Universiteit Eindhoven, The Netherlands, 2004.
- [44] P. Munoz, R. Garcia-Olcina, C. Habib, L. R. Chen, X. J. M. Leijtens, J. D. Domenech, M. Rius, J. Capmany, T. De Vries, M. J. R. Heck, L. Augustin, R. Notzel, and D. Robbins, "Multi-wavelength laser based on an arrayed waveguide grating and sagnac loop reflectors monolithically integrated on InP," *IET Optoelectronics*, vol. 5, 2011.
- [45] E. Kleijn, M. Smit, and X. Leijtens, "Multimode Interference Reflectors: a new class of components for photonics integrated circuits," *J. Lightw. Technol.*, vol. 31, no. 18, pp.3055-3063, 2013.
- [46] A. Stöhr, "Pushing the Boundaries", *IEEE Microwave Magazine*, vol. 10, no. 4, pp. 106-115, 2009, invited paper.
- [47] iPHOS project website, <http://www.iphos-project.eu>.
- [48] Deliverable D4.3 of iPHOS project, "Phase noise spectral density for first-order loop".
- [49] K. Balakier, M.J. Fice, L. Ponnampalam, A.J. Seeds, C. Renaud, "Monolithically Integrated Optical Phase Lock Loop for Microwave Photonics" *Journal of lightwave technology*, vol. 32, no. 20, 15 October 2014.

- [50] A.L. Schawlow and C.H. Townes., “Infrared and Optical Masers”, *Physical Review*, vol. 112, pp. 1940-1949, 15 December 1958.
- [51] C.H. Henry, “Theory of the linewidth of semiconductor lasers”, *IEEE Journal of quantum electronics*, vol. qe-18, no. 2, February 1982.
- [52] F. Riehle, “Frequency standards – Basics and applications”, Weinheim: WILEY-VCH verlag, 2004, ISBN 3-527-40230-6.
- [53] L. Chusseau, F. Philippe, P. Viktorovitch and X. Letartre, “Mode competition in a dual-mode quantum-dot semiconductor microlaser”, *Physical Review A*, vol. 88, no. 1, 015803, July 2013.
- [54] L. Chusseau, F. Philippe, and F. Disanto, “Montecarlo modeling of the dual-mode regime in quantum-well and quantum-dot semiconductor lasers”, *Optics Express*, vol. 22, no. 5, 2014.

CHAPTER 2

Integration technology

Abstract – In this chapter, the active-passive integration technology process used to fabricate the devices presented in Chapters 4 and 6 of this thesis is explained. The fabrication is based on the standardized generic integration technology developed at COBRA. Minor variations that were made to the standardized process flow are discussed. The last section of this chapter describes the mounting and the wire-bonding of the chips implemented in order to simplify the characterization of the devices in the lab.

2.1 Introduction

Semiconductor technology allows for integrating several different components on a single chip. The fabrication of a monolithically integrated circuit results in many advantages compared to the use of discrete components: compactness, lower power consumption, higher operation speed, reproducibility, and potentially lower costs. In our case, in particular, small size and low power consumption are fundamental requirements since the devices are designed to be part of a compact mm-wave generation system.

Nowadays many photonic integration technologies are available. These technologies are based on different material systems such as Silicon (Si) [1], Gallium-Arsenide (GaAs) [2] and Indium-Phosphide (InP) [3] or on hybrid integration systems [4]. Furthermore, different integration approaches have been developed among the different fabrication platforms based on the same material system [3]. Each of these technologies has its own capabilities.

InP has already been used during the last decades for the integration of light sources in the C band (1530 - 1565 nm) [3]. The main advantage of the InP-based integration technology is the possibility to monolithically integrate active components (e.g., SOAs) with passive components. For this reason an integration process based on InP/InGaAsP technology was developed at COBRA. The possibility to integrate active and passive components on the same InP-wafer originates from the fact that an $\text{In}_{1-x}\text{Ga}_x\text{As}_y\text{P}_{1-y}$ layer can be grown lattice matched on InP, provided that specific values of x and y are used (Vegard's Law [5, 6]). As a result, in this system different layers with a controllable direct band gap can be combined to create optical amplifiers and waveguides that operate in the 1550 nm telecom wavelength region. Different types of active material structures available for InP integration technology are able to generate light in the C band. The InP-based integration technology allows for the use of quantum well [6], bulk semiconductor [6] or quantum dot or dash based gain materials [6, 7]. The most commonly used material for optical amplifiers is based on QWs because of its electrical efficiency and high small-signal gain. At COBRA, the standard amplifier structure used for the device fabrication is based on a 4-QW structure. As explained in Chapter 4, such a structure is suitable for the dual wavelength devices.

The devices presented in Chapters 4 and 6 of this thesis have been fabricated by the author using the standardized fabrication process developed at COBRA. This process for the fabrication of InP/InGaAsP-based PICs operating in the 1550 nm wavelength region has been tested and improved over the last decade. COBRA active-passive technology allows for integrating on the same chip components that can generate, amplify or absorb light (e.g., (SOAs), photodetectors (PDs)) with components that are transparent around 1550 nm and are used to manipulate light (e.g., shallow and deep passive waveguides, arrayed waveguide gratings, phase modulators (PHMs)).

In section 2.2 the growth of the active-passive wafers is described together with the explanation of the main fabrication steps of the technology process used. In section 2.3 the adaptations made to the standardized COBRA integration technology are presented and the fabrication issues faced during the device fabrication are discussed. Section 2.4 completes the chapter with a description of the mounting system used for the measurements.

2.2 Fabrication technology

The fabrication of a PIC includes two main stages: the growth of the active-passive semiconductor wafer with a specific layerstack and the process used to create the PIC on the wafer. In the first part of this section, the main steps of the fabrication of the wafer are described and the resulting layerstack is presented. In the second part, the process flow used to fabricate the devices on wafer is explained in detail.

2.2.1 Active-passive wafers

Different techniques can be used to grow wafers suitable for the integration of both active and passive components. Among the others (e.g., selective area growth [8], QW intermixing [9], offset active region [10]), the butt-joint coupling method [11] shows better performance in terms of flexibility in material growth and device design, such as layer thickness, layer composition and doping concentration [12]. The weak point of this technique is the difficulty to control the defect density in the passive areas and the quality of the active-passive interface. Issues with the quality of the active-passive transition lead to undesired optical reflections in waveguides at the interface. However, the problem can be solved by using appropriate angles between the waveguide and the active-passive transition [13].

The wafers used in the fabrication described in this chapter were grown through multi-wafer low pressure organometallic vapor phase epitaxy (LP-MOVPE) at 650 °C using trimethyl alkyls of gallium (TMGa) and Indium (TMIn), together with pure arsine (AsH₃) and pure phosphine (PH₃) as precursors. Hydrogen sulphide (H₂S), diluted to 1% in hydrogen, and diethyl zinc (DEZn) were employed to bring in n-type and p-type dopants, respectively. Palladium-diffused hydrogen was used as carrier gas [14]. The growth process has been performed at the MiPlaza division of Philips Research according to the following process flow:

- a) First epitaxial growth. A 500 nm thick InP waveguide bottom cladding (layers E1-1 and E1-2 in Table 2.1) is grown on an n-doped InP substrate (E1-0). Then, the 500 nm thick InGaAsP waveguide core (Q1.25) is grown. Four InGaAs QWs are sandwiched between the Q1.25 material layers (E1-6). The waveguide core contains also a 10 nm non-intentionally-doped

- (n.i.d.) etch-stop layer (E1-4) to be used in the etch-back process of the next fabrication step. This epitaxial growth ends with a 20 nm n.i.d. InP layer (E1-8).
- Etch-back step. By means of a photolithography process, the active regions are defined in a SiN_x layer deposited with plasma-enhanced chemical vapor deposition (PECVD). The SiN_x is used as hard mask while the uncovered areas are etched-back to the etch-stop layer embedded in the waveguide core.
 - Second epitaxial growth. After a cleaning step performed using bromine-methanol, the passive layerstack is grown on the etched-back regions. A 20 nm n.i.d. InP layer (E2-2) is grown on top of a 320 nm InGaAsP waveguide core layer (E2-1).
 - Third epitaxial growth. The SiN_x layer is removed and a 1480 nm p-InP layer (E3-1, E3-2, E3-3) is grown with increasing doping concentration to complete the waveguide top cladding. Finally, the contact layer is grown: 40 nm of p-InGaAsP (E3-4 and E3-5) followed by a 280 nm p-InGaAsP layer.

		Passive Layerstack				Active Layerstack				
	Layer	Material	Doping (cm^{-3})	Thickness (nm)	Color code	Color code	Thickness (nm)	Doping (cm^{-3})	Material	Layer
Epi-3	E3-6	p-InGaAs	$1.5 \cdot 10^{19}$	280			280	$1.5 \cdot 10^{19}$	p-InGaAs	E3-6
	E3-5	p-Q1.4	$7.2 \cdot 10^{18}$	10			10	$7.2 \cdot 10^{18}$	p-Q1.4	E3-5
	E3-4	p-Q1.2	$4.7 \cdot 10^{18}$	10			10	$4.7 \cdot 10^{18}$	p-Q1.2	E3-4
	E3-3	p-InP	$1 \cdot 10^{18}$	1000			1000	$1 \cdot 10^{18}$	p-InP	E3-3
	E3-2	p-InP	$5 \cdot 10^{17}$	300			300	$5 \cdot 10^{17}$	p-InP	E3-2
	E3-1	i-InP	n.i.d.	180			180	n.i.d.	i-InP	E3-1
Etch-back and Epi-2	E2-2	i-InP	n.i.d.	20			20	n.i.d.	i-InP	E1-8
							120	n.i.d.	Q1.25	E1-7
							4x20	n.i.d.	InGaAs/Q1.25	E1-6
	E2-1	i-Q1.25	n.i.d.	320			120	n.i.d.	Q1.25	E1-5
Epi-1	E1-4	i-InP	n.i.d.	10			10	n.i.d.	i-InP	E1-4
	E1-3	i-Q1.25	n.i.d.	170			170	n.i.d.	Q1.25	E1-3
	E1-2	i-InP	n.i.d.	70			70	n.i.d.	i-InP	E1-2
	E1-1	n-InP	$5 \cdot 10^{17}$	430			430	$5 \cdot 10^{17}$	n-InP	E1-1
	E1-0	n-InP	$1 \cdot 4 \cdot 10^{18}$	substrate			substrate	$1 \cdot 4 \cdot 10^{18}$	n-InP	E1-0

Table 2.1: Schematic description of the active-passive layerstack. The thick lines separate the different growth steps. Firstly, the active layerstack is grown on the substrate (first epitaxial growth: E1-layers). Secondly, the designed passive areas are etched-back to the InP etch-stop layer (E1-4). Then, the layers of the passive layerstack are grown during the second epitaxial growth (E2-layers). Finally, the common top cladding layers and the contact layers are grown in the third epitaxial growth (E3-layers).

Before starting the second part of the fabrication, the actual structure of the layerstack is verified during the so-called layerstack determination process. Knowing the exact thickness of the different layers is a fundamental requirement in order to be able to fabricate successfully a photonic integrated circuit (PIC) since the depth of the etching steps depends on the thickness of the layers of the wafer. Deviations of up to 10% of the thickness of a layer are acceptable for continuing with the device fabrication. The layerstack determination is done through a selective wet chemical etching process, using a diluted $\text{H}_2\text{SO}_4:\text{H}_2\text{O}_2$ solution to etch ternary and quaternary materials and a diluted $\text{H}_3\text{PO}_4:\text{HCl}$ solution to etch InP. The area to be etched is opened in a 50 nm SiN_x layer deposited on

the wafer. After each etch step, the etch depth is measured by scanning the surface of the wafer with a Tencor surface profiler. This process can be performed on a twin-wafer (a wafer grown during the same process of the one used for the actual fabrication), on a cleaved strip of the wafer, or selectively on a small area of the wafer. However, the last option may cause nonuniformities (in the areas beside the one used for layerstack determination) in the thickness of photoresist used afterwards for the optical waveguide lithography.

2.2.2 Active-passive process flow

Five types of waveguide structures have been integrated in the fabricated devices using the active-passive integration technology available at COBRA. The five structures are: passive shallow waveguides, passive deep waveguides, isolation sections, PHMs, and SOAs. Also PDs are integrated in the devices, however SOAs and PDs are considered as a single waveguide structure since they have the same cross-section. SOAs (and PDs), PHMs and isolation sections are shallowly etched. A shallowly etched structure has a low contrast ridge waveguide and a trench beside the waveguide ridge is etched down to 100 nm into the waveguide core. The trench beside a deeply etched waveguide is etched down to 200 nm below the waveguide core, as shown in Fig. 2.1.

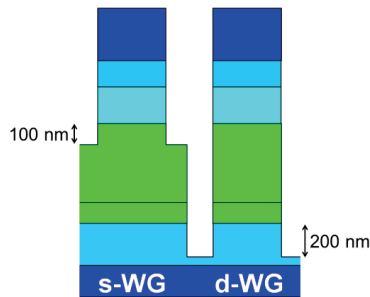


Fig. 2.1. Cross-section of a shallowly etched waveguide (left) and a deeply etched waveguide (right). The trench beside a shallow waveguide ridge is etched down to 100 nm into the waveguide core whereas the trench beside a deep waveguide is etched down to 200 nm below the waveguide core. The dimensions of the structures are not consistently scaled. The color code is the same of Table 2.1.

The main fabrication steps are listed and discussed in detail in the following. The cross-sections of the waveguide structures during the different fabrication steps are presented in Fig. 2.2. From left to right: SOA, shallow waveguide, deep waveguide, isolation section, PHM. The dimensions in the pictures are not consistently scaled.

- 1) **Optical waveguide lithography** - A 600 nm thick SiN_x layer is deposited on the wafer using a PECVD process. The optical waveguide pattern is defined in a 750 nm thick layer of positive photoresist HPR504 using vacuum-contact photolithography. The vacuum-contact mode allows for obtaining the maximum resolution possible with the Süss Mask Aligner MA6: 0.6 μm . The waveguide pattern is transferred to the SiN_x layer using a dry CHF_3 Reactive-Ion Etching (RIE) process. After removal of the photoresist, the optical waveguide pattern remains in the 600nm SiN_x layer which is used as a hard-mask in the following Inductively Coupled

Plasma (ICP) etch steps. In our technology, all the waveguides (both passive and active) are defined between trenches in the lithography mask: this means that not only does the pattern of the actual waveguides have to be transferred to the SiN_x layer, but also all the areas that are not part of the trenches. In other words, the SiN_x layer is etched away only in the areas corresponding to the trenches. The use of trenches makes the surface of the wafer more uniform, simplifying the planarization process and the etch-back step of the polyimide (see section 2.3.6).

- 2) **Deep areas lithography** - The areas where the waveguides have to be deeply etched are defined in a 3 μm thick layer of positive photoresist AZ4533 using hard-contact photolithography. The hard-contact mode provides a lower resolution than the vacuum-contact mode, but still suitable for all the lithography steps apart from the optical waveguide lithography. The use of hard-contact mode reduces the risk of damaging the photoresist layer. The photoresist is hard-baked and used as a mask (together with the SiN_x layer) in the first InP ICP etch step.
- 3) **First InP ICP etch step** - In the first InP ICP dry etch step, the depth difference between the bottom levels of the shallow and deep waveguide trenches is defined using an optimized CH_4/H_2 ICP dry etch process. The etching is done in cycles that are alternated by the O_2 -descum process used to clean the sample from polymers that are deposited on the surface during the etching process.

In the calculation of the number of etching cycles that are required to achieve the etch depth we are aiming for, the contact layer is considered to be a uniform 300 nm InGaAs layer and the 20 nm of InGaAsP layers (E3-4 and E3-5 in Table 2.1) are considered as 20 nm of InGaAs. The reason for this approximation lies on the fact that during the layerstack determination it is not possible to discriminate between InGaAs and InGaAsP in the contact layer. Similarly, the 10 nm of InP etch-stop layer embedded in the waveguide core (E1-4) are considered to be 10 nm of InGaAsP (see section 2.3.4). These approximations lead to changes in etching time that are well within the uncertainty of the etching rate.

The etch depth aimed for in the first ICP etch step is 520 nm. This etching goes through 300 nm of contact layer and 220 nm of top cladding. This initial etch depth leads to a depth difference of 600 nm between the bottom levels of the shallow and deep waveguide trenches. This increase of depth is due to the difference in etching rate of the various layers. These values do not take into account the lag effect which is discussed below (second ICP etch step). Further details on the etching depth and etching time calculation are presented in the Appendix to Chapter 2.

- 4) **Second ICP etch step** - After the first InP ICP etch step, the hard-baked photoresist is removed using an oxygen plasma process. In the second InP ICP dry etch step, the height difference between the top of the isolation sections and the bottom of the shallow waveguide trenches is defined using the same etching process as the one used at point 3. The etching rate is slightly lower in the areas directly beside a ridge waveguide than in the areas further from the waveguides where the etch depth is actually measured. This issue is known as lag effect and it is taken into account in the calculation of the etching time of the second ICP etch step.

Preliminary tests have been done by the author in order to estimate the impact of the lag effect before starting the fabrication of the devices. The lag effect impact has been estimated to be approximately 80 nm. The etch depth aimed for in the second ICP etch step is 320 nm. This etch, from the top of the wafer, consists of 300 nm thick contact layer and 20 nm of top cladding. It results in a step height of 500 nm after all the dry etch steps (320 nm of top cladding, 100 nm of waveguide core, and further 80 nm of waveguide core to compensate the lag effect).

- 5) **Isolation section lithography** - In this step, the SiN_x mask is removed from the areas where the isolation sections have to be made. First, the isolation sections are defined in a 3 μm thick layer of positive photoresist AZ4533 using hard-contact photolithography. Then, the SiN_x layer is etched away using the RIE dry etch process presented at point 1.
- 6) **Third ICP etch step** - After photoresist removal, in the third InP ICP etch step, the height difference between the top of the passive waveguides and the top of the isolation sections is defined using the same ICP etch process presented at point 3. During the third ICP etch step 1080 nm of the top cladding is etched.
- 7) **Contact layer removal lithography** - In this step the SiN_x mask is removed from the passive waveguides that do not need the InGaAs contact layer for metal contacting. The SiN_x mask remains only on areas where a metal contact needs to be formed, i.e. the SOAs and PHMs. First, the contact areas are defined in a 3 μm thick layer of positive photoresist AZ4533 using hard-contact photolithography. Then, the SiN_x layer is etched away using the RIE dry etch process presented at point 1.
- 8) **Fourth ICP etch step** - After photoresist removal, in the fourth InP ICP etch step the height difference between the top of the contact layer and the top of the passive waveguides is defined using the same ICP etch process presented at point 3. The targeted etch depth of the fourth ICP etch step is 580 nm (400 nm of top cladding, 100 nm of waveguide core, and further 80 nm of waveguide core that compensate the lag effect) that corresponds to 400 nm etched at the top of the shallow waveguides (300 nm contact layer and 100 nm of top cladding layer). With this step, the final etch depth of all the waveguide structures is achieved: 100 nm (plus lag effect) into the waveguide core for the active and passive shallow waveguides and for the isolation sections; 200 nm (plus lag effect) below the waveguide core for the deep waveguides. At the same time, the contact layer is etched away from the passive waveguides. After wet chemical removal of the remaining SiN_x mask through the use of a buffered hydrofluoric acid (BHF) solution, the final waveguide topography is defined.
- 9) **Planarization** - The wafer is planarized using photo-sensitive polyimide PI2723. After spinning a first layer of polyimide, the sample is heated to a temperature of 325 °C for an hour to cure the PI2723. Afterwards, the polyimide is etched back using a CHF_3/O_2 RIE dry etch process to 100 nm below the top of the contact layer (a). After spinning a second layer of polyimide, photolithography is used to open only the areas where the metal contacts have to be made (b). Finally, the curing process is repeated.

10) Metallization - Firstly, a 120 nm thick layer of silicon oxide (SiO_2) is deposited using PECVD process. The only goal of this layer is to improve the adhesion of the metal layer which would be very poor if the metal was deposited directly on polyimide. Secondly, the contact areas are opened in a 3 μm thick layer of positive photoresist AZ4533 using photolithography. Thirdly, a wet chemical etching process in a BHF solution is used to remove the SiO_2 from the contact areas. In this wet etching step, the photoresist acts as a mask.

The metallization pattern is defined using photolithography in a 2.5 μm thick layer of negative photoresist MaN-440. The profile of this photoresist layer is suitable for a lift-off process. In order to improve the adhesion of the metal, the surface of the contact layer has to be clean. This is obtained through wet chemical etching of the top 100 nm layer of InGaAs (using highly diluted $\text{H}_2\text{SO}_4:\text{H}_2\text{O}_2:\text{H}_2\text{O}$ solution). Afterwards, the Ti/Pt/Au 60/75/600 nm p-metal contacts are deposited using e-beam evaporation followed by the lift-off process in acetone. One common n-metal contact on the backside of the wafer is created by evaporating Ti/Pt/Au 60/75/200 nm.

The remaining SiO_2 layer is removed using the dry etch RIE process presented at point 1 and the wafer is annealed at 325 °C for 90 s. If the SiO_2 is not completely removed, the wafer could be destroyed because of decomposition of the polyimide during the annealing.

In the COBRA integration technology process, the thickness of the p-metal contacts on the SOAs is increased (by approximately 1.7 μm) using an Au-electroplating process. However, no plating has been performed during the fabrication of the devices presented here. For further details, see section 2.3.7.

11) Cleaving - The fabrication process is completed with the cleaving of the 360 μm thick wafer. It is important that the cleaving areas are free from polyimide. Cleaving tests through areas covered with polyimide show that it is better to keep the cleaving areas free from polymer. The reason is that parts of polyimide could stick out over the edge of the chip covering the facet of the output waveguides: this would make the characterization of the PIC impossible.

After cleaving, the fabricated chips are mounted on an aluminum submount using an electrical and thermal conductive epoxy resin. Section 2.4 presents in detail the mounting system used for the characterization of all the devices presented in this thesis.

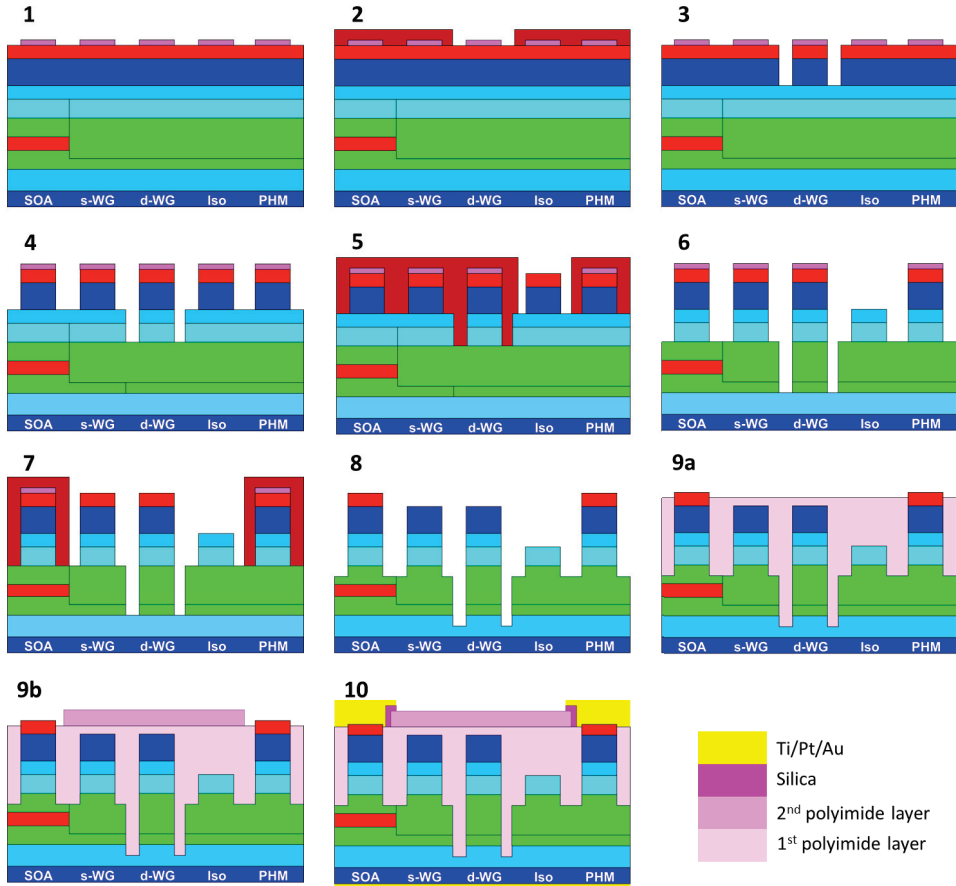


Fig. 2.2. Cross-section of the different waveguide structures during different fabrication steps. From left to right: SOA (or PD), shallow waveguide, deep waveguide, isolation section, PHM. The dimensions of the structures are not consistently scaled. Apart from the four materials indicated, the color code is the same of Table 2.1. The 10 nm of InP etch-stop layer embedded in the waveguide core are considered to be 10 nm of InGaAsP in this figure.

(1) Optical waveguide lithography, (2) Deep areas lithography, (3) First InP ICP etch step, (4) Second InP ICP etch step, (5) Isolation section lithography, (6) Third InP ICP etch step, (7) Contact layer removal lithography, (8) Fourth InP ICP etch step, (9a) First polyimide layer etched-back, (9b) Second polyimide layer lithography, (10) Metallization.

2.3 Fabrication issues

The active-passive layerstack and the processing steps that have been used to fabricate the devices presented in Chapters 4 and 6 are described in the previous section. In this section two further fabrication related topics are discussed. Firstly, the differences in fabrication with the

standardized COBRA fabrication process are presented. Secondly, a number of issues that came up during the device fabrication are described.

2.3.1 Top InP cladding

In the active-passive layerstack used in the MPW runs at COBRA, the first epitaxial growth ends with 200 nm p-doped ($3 \cdot 10^{17} \text{ cm}^{-3}$) InP layer above the InGaAsP waveguide core [15]. The p-doping in this InP layer is included to improve the conductivity through the active waveguides (SOAs).

In the active-passive layerstack growth process of the wafers used to fabricate the devices presented in Chapters 4 and 6, the first epitaxial growth ends with a 20 nm n.i.d. InP layer (E1-8 in Table 2.1) on top of the InGaAsP waveguide core layer (E1-7 in Table 2.1). The thickness of this InP layer has been chosen to be as small as possible to minimize the total height of the layers grown during the second epitaxial growth and consequently minimize the height variations between the active and the passive regions at the butt-joint interfaces.

In the third epitaxial growth, a further 180 nm of n.i.d. InP are grown (E3-1 in Table 2.1): as a result, both active and passive regions have a 200 nm n.i.d. InP layer (E1-8 plus E3-1 for the active regions and E2-2 plus E3-1 for the passive regions, in Table 2.1). These InP layers are designed to be n.i.d. in order to minimize the optical losses in the waveguides. The choice of the level of doping in the different layers is a tradeoff between minimizing optical losses and maximizing electrical conductivity. Since in this work we have chosen to have n.i.d. InP layers above the quaternary waveguide core, the voltage over the amplifiers of the devices we fabricated can be slightly higher than that of the devices fabricated with the standardized COBRA layerstack. Similar design choices were made for the layerstack in the devices presented in [16].

2.3.2 InGaAsP etch-stop layer

In the standardized COBRA passive layerstack, a 20 nm thick InGaAsP layer is present 200 nm above the waveguide core. This InGaAsP layer in the COBRA layerstack can be used as an etch-stop layer to create isolation sections through wet chemical etching. Since at the moment all the InP etching steps are performed by means of dry ICP etching, this InGaAsP etch-stop layer is present in the standardized COBRA passive layerstack only because of historical reasons. The InGaAsP layer is not present in the layerstack presented here (Table 2.1).

2.3.3 Doping in the passive waveguides

For the passive regions, the choice of the level of doping in the different layers is a tradeoff between minimum waveguide losses and maximum phase shift efficiency in the PHMs. On one hand, because of higher carrier effects, a PHM with an n-doped waveguide core has higher phase modulation efficiency than one with n.i.d. quaternary material [12, 17]. On the other hand, the n-doping in the waveguide core causes an increase in the optical losses due to the increased carrier absorption. In the COBRA layerstack, the InGaAsP core has an n-doping level of $6 \cdot 10^{16} \text{ cm}^{-3}$. However, since the increase in the phase modulation efficiency is marginal [12], we have chosen to keep the doping of the waveguide core (E2-1 in Table 2.1) as low as possible (n.i.d.).

In our wafer, the first two InP layers on top of the InGaAsP core are also n.i.d. (E2-2 and E3-1 in Table 2.1). In the COBRA layerstack, n-doping is applied to the InGaAsP etch-stop layer and to the 200 nm InP layer on top of the waveguide core. This doping should compensate for the diffusion of the p-doping from the layers above. In our wafer, this compensation doping has not been applied in order to reduce the concentration of impurities. The devices presented here have large AWGs and long passive waveguides, thus it is important to keep the passive waveguide losses as low as possible.

2.3.4 InP etch-stop layer in the waveguide core

During the active-passive wafer fabrication, after the first epitaxial growth, the layers from E1-8 down to E1-5 are etched-back outside the masked active areas (section 2.2.1). The etch-back process is performed using a wet chemical etch. In order to obtain uniform and precisely defined profile and surface in the etched-back areas, a 10 nm InP etch-stop layer (E1-4 in Table 2.1) is embedded in the waveguide core in order to stop the etching process at the desired level (120 nm below the lower QW). Since the InP etch-stop layer is only 10nm thick, it might be removed in the passive areas during the bromine-methanol cleaning step prior to the second epitaxial growth (selective area re-growth). The layerstack determination process showed that, indeed, in some wafers the etch-stop layer was removed whereas it is present in other wafers. The influence of this layer is assumed to be negligible for both the optical field and the electrical properties of the wafer.

2.3.5 Critical dimension loss

In the standardized COBRA integration technology, the widths of the ridges of shallow waveguides and deep waveguides are designed to be respectively 2.0 μm and 1.5 μm . In order to obtain the desired values, in the mask designs of the PICs fabricated previously at COBRA, the shallow waveguides were drawn 2.2 μm and 1.7 μm wide for the shallow and deep waveguides respectively. The difference between the value designed for the actual waveguides and the value in the mask design is called Critical Dimension Loss (CDL). The origin of this loss in the width of the waveguides from the mask design to the actual waveguides is twofold. The supplier of the masks used previously at COBRA specifies a loss in width that occurs while writing the pattern on the mask plate (by means of electron beam). This loss is estimated to be approximately 0.2 μm . Furthermore, recently at COBRA, a loss of width was noticed while transferring the waveguide pattern from the photoresist HPR504 to the SiN_x hard-mask layer (most probably, the photoresist is attacked slightly by the plasma).

At the time of fabrication of the devices presented here, very little experience was developed with the new supplier of masks. In our mask design, the CDL was chosen equal to 0.25 μm to compensate for both causes of width loss. Unfortunately, the loss of width from the mask design to the mask plate appeared to be negligible. This means that the width of the shallow (deep) waveguides is 2.25 μm (1.75 μm) in the mask plate. As a result, the width of the openings between the arrayed waveguides at the edge of the FPR of the AWG is reduced to 0.55 μm instead of matching the designed value ($gap_a = 0.8 \mu\text{m}$). These are the smallest openings on the mask (and consequently the most critical) and it is pivotal for the functioning of the AWG that they are open on the wafer. Since, according to specification, the best resolution that one can obtain with the Süss

Mask Aligner MA6 is $0.6\ \mu\text{m}$, in order to be able to open $0.55\ \mu\text{m}$ wide strips the photoresist has been over exposed. This, obviously, has result in thinner waveguide patterns in the resist layer.

Furthermore, the width loss occurring during the transfer of the pattern from the photoresist to the SiO_x hard mask has been larger than expected (however, no CDL scanning electron microscope (SEM) measurements have been done).

The final consequence is that the actual shallow (deep) waveguides of the devices presented here are $1.8\ \mu\text{m}$ ($1.3\ \mu\text{m}$) wide instead of $2.0\ \mu\text{m}$ ($1.5\ \mu\text{m}$). The impact of this effect on the performance of the PIC is discussed in Chapter 4.

2.3.6 Planarization

After the fourth InP ICP etch step, the waveguide topography is defined and the wafer needs to be planarized with polyimide before metal evaporation. The polyimide supports the metal pads that are wider than the width of the waveguides. The planarization of the devices presented here has been done according to the standardized integration technology COBRA process (point 9 of section 2.2.2). However, this process is different from the one followed for some devices previously fabricated at COBRA, as presented in [16, 18]. The planarization step for those devices was done by spinning six layers of polyimide alternated with curing and surface treatment.

The use of the six layers of polyimide was justified by two reasons. The first one concerns the uniformity of the surface. The waveguides of the devices fabricated at COBRA until the COBRA 4 run (year 2010) were not designed in trenches. This means that, apart from the waveguides and the deeply etched areas, all the regions on the wafer were etched down to the level of the bottom of the ridge of the shallow waveguides. As a consequence, the average level of the surface of the wafer could vary substantially from one area to another if the distribution of waveguides was not uniform around the wafer. In such a case, the height variations are reduced to approximately $150\ \text{nm}$ after the spinning of six layers of polyimide whereas variations higher than $500\ \text{nm}$ can be present if only two layers of polyimide are used. However, when the waveguides are designed in trenches, the areas of the wafer that are not occupied by waveguides or trenches have the same vertical structure as the passive waveguides. This results in a much more uniform height profile. As a consequence, one layer of polyimide is sufficient to obtain height variations lower than $200\ \text{nm}$ which is the limit value to be able to open all contacts approximately at the same time when etching back the polyimide (the spinning and the lithography of the second layer of polyimide are done after the etch-back step).

The second reason for the use six layers was the roughness of the polyimide after the etch-back step. When the devices were planarized with six layers of polyimide, the COBRA process flow did not included the SiO_2 deposition step after the planarization process. This means that the metal had to stick to the surface of the polyimide. In order to be able to make a good adhesion between the metallization and the polyimide, the surface of the polyimide has to be rough. Indeed, the etch-back process of 6 layers of polyimide (~ 35 minutes) resulted in a much more rough surface than the etch-back of only one layer (~ 5 minutes with trenches, ~ 2 minutes without trenches) since the roughness of the surface is proportional to the etch-back time. However, thanks to the SiO_2 deposition step, in the current fabrication process, the metal is not evaporated on the polyimide surface, but on the SiO_2 layer, solving the adhesion issue.

If the polyimide has been contaminated by particles or if there are particles on the surface of the wafer, there is a high risk that no polyimide will be present around these particles after the spinning process [18]. Depending on their position, these holes in the polyimide layer can affect the performance of the device. If, after spinning the first layer of polyimide, a hole is present in an area where a contact opening has to be made (e.g. where an SOA or a PHM is designed), then it is necessary to remove the polyimide by means of oxygen plasma and repeat the spinning step. The reason is that, because of the hole, the contact area between the semiconductor material and the evaporated metal would be not only the top of the ridge of the waveguide (i.e. the contact layer) but the whole area of the hole. This means that the metal would cover the whole height of the waveguide ridge increasing dramatically the optical losses. If the holes are present only in areas where passive components are located, the fabrication can continue. However, it is necessary to verify that the second layer of polyimide covers all the holes in order to avoid metal deposition on passive components.

The use of two layers of polyimide simplifies and speeds up the fabrication process especially because four curing steps are avoided. Considering the curing time and the time required to cool down the vacuum oven, each curing cycle takes approximately 8 hours.

After spinning and curing the polyimide, areas appeared where the polyimide was much thicker than expected. This happened in both test fabrication runs and the actual fabrication runs for devices. The anomalies were positioned on some FPRs of AWGs on a wafer in which the waveguides were not in trenches as well as on large areas with no waveguides in a fabrication run in which the waveguides were in trenches. Fig 2.3a shows one of these anomalies on a FPR.

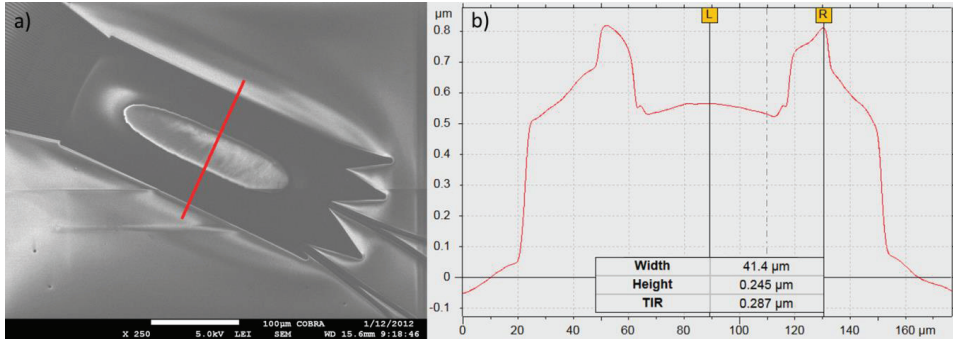


Fig. 2.3. Unexpected thicker areas have been noticed in the polyimide profile after spinning and curing. These anomalies have been found, for example, on FPRs of AWGs (a) in wafer used for a fabrication test run. A surface profiler has been used to analyze the topography of these areas. The profile depicted in (b) corresponds to the red straight line shown in (a). The height difference between the top of these anomalies and the normal level of polyimide is around 245 nm. The origin is still uncertain, but it is predicted that there is no significant impact on the performance of the PICs.

The topography of such a structure has been analyzed, scanning the surface of the wafer with a Tencor surface profiler (Fig. 2.3b). The height difference between the top of these anomalies and the normal level of the polyimide is around 245 nm. After etching back completely the polyimide on a test wafer, the surface has been scanned, showing a regular profile of the III-V material. This demonstrates that these anomalies are indeed in the polyimide layers and not in the semiconductor

material. Consequently, no significant impact on the performance of the PICs is expected. The origin of this behavior of the polyimide is still uncertain, although we suspect it is related to outgassing.

In the standardized COBRA process, the SiO₂ layer has a thickness of 200 nm. During the fabrication of the devices presented here, however, a 120 nm SiO₂ layer has been deposited. A 200 nm thick SiO₂ layer has a color that is hard to differentiate from that of InP and InGaAs whereas a 120 nm SiO₂ layer is blue and thus it that can clearly be distinguished. This clear distinction is important to easily verify that the SiO₂ layer has been removed from the openings in the photoresist on the contact areas at the end of the wet chemical etching step. The thickness of the SiO₂ layer has no impact on the performance of the PICs since the SiO₂ is simply used as an adhesion layer for the metal pads.

2.3.7 Metallization and plating

In the standardized integration technology COBRA process, Ti/Pt/Au 60/75/300 nm p-metal contacts are deposited using e-beam-based evaporation followed by lift-off process in acetone. Afterwards, the thickness of the contacts on the SOAs is increased (by approximately 1.7 μm) using Au-electroplating process. This is done in order to optimize the current distribution and minimize the electrical losses in the contact [19]. The main steps of the electroplating process are:

- sputtering of a Ti/Au 50/100 nm seed layer on the surface of the wafer;
- definition of the plating areas in a positive photoresist layer (AZ4533) using photolithography;
- thickening of the metal layer through electroplating in a gold bath;
- removal of the photoresist;
- wet chemical etching of the undesired seed layer (between the different metal pads) by means of potassium cyanide (KCN) solution.

The electroplating process is complex, risky and time consuming. The possible problems that one might face during the electroplating process are several and they could result in non-uniform thickness and poor adhesion of the gold [18]. The tests that we have performed show that the wet chemical etching by means of KCN solution is the most critical part of the plating process. During this last step, under-etch of the seed layer can occur between the evaporated metal layer and the layer of gold deposited via electroplating process. This under-etch can be enhanced by the presence of impurity in the titanium of the seed layer. It is hard to estimate how deep the under-etch can be without cleaving through the interested area. However, it is clear that this under-etch limits the benefits of the electroplating because it compromises the electrical performance of the metal contact and, in particular, the uniformity of current distribution. The delamination process can be enhanced by film stress in the plated gold layer. This stress depends on several parameters: plating current, pulse duty cycle, time, temperature, and geometry (Faraday's second law [20, 21]). If the width of the metal contact is narrow, a pronounced under-etch of the titanium of the seed layer combined with tensile stress in the plated gold can lead to the complete separation of the plated layer from the evaporated metal contact, as shown in Fig 2.4. In Fig. 2.4a, it can be noticed that gold strips have torn off and are not in contact with the corresponding evaporated metal. The width of these metal contacts is 20 μm. In the larger metal pads (180 μm large), the gold sticks to the evaporated metal underneath because the under-etch is much smaller than the width of the pads. Fig. 2.4b shows in

detail that indeed the gold tears off exactly where the metal pad becomes more narrow. A new plating process flow is under development at COBRA in order to solve this problem.

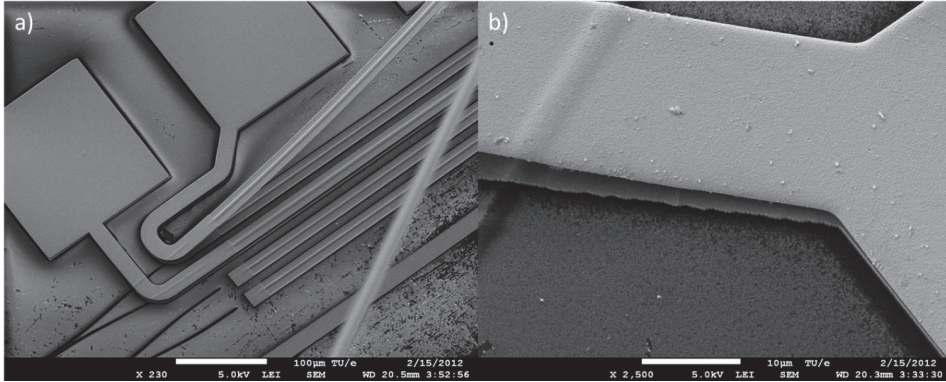


Fig 2.4. (a) 20 μm large strips of gold (previously deposited via electroplating process) do not stick to the corresponding evaporated metal because of under-etch of the seed layer during wet chemical KCN-based etching process. (b) The gold tears off exactly where the metal pad becomes more narrow: if the pad is larger than the under-etch, the gold (partially) sticks to the evaporated metal.

Furthermore, wire-bonding is preferably done on non-plated pads due to the fact that plated gold contains contaminants, enclosures or can have a poor structure. These effects can make the adhesion of a wire-bonding on plated gold more difficult.

For these reasons, no plating has been performed on the pads of the devices presented here. However, instead of evaporating Ti/Pt/Au 60/75/300 nm, the layer of gold has been increased to 600 nm (Ti/Pt/Au 60/75/600 nm) in order to reduce the electrical losses in the contacts. The evaporation of a thicker layer of metal does not cause any further risk since the average thickness of the negative photoresist used for the metal pads definition (MaN-440) is 2 μm . In order to be able to perform the lift-off process, the thickness of the photoresist has to be larger than the total thickness of the evaporated metal pads in every area of the wafer surface. This metallization method shortens the fabrication process time since one photolithography step and all the plating-related steps are avoided. A standardized annealing process ($T = 325\text{ }^\circ\text{C}$, $t = 90\text{ s}$) has been applied.

Also another metallization process flow has been explored on test-devices. This method is convenient in case the photoresist thickness is not sufficiently thick to evaporate Ti/Pt/Au 60/75/600 nm in a single evaporation step. The process flow consists of two cycles of the following steps: photolithography, Ti/Pt/Au 60/75/300 nm evaporation, lift-off. The result is a Ti/Pt/Au/Ti/Pt/Au 60/75/300/60/75/300 nm metal layer structure, in short: 2x(Ti/Pt/Au 60/75/300 nm). However, probably due to the presence of a further layer of titanium, the 2x(Ti/Pt/Au) 60/75/300 nm contacts show slightly worse performances (higher contact resistance) than the Ti/Pt/Au 60/75/600 nm contacts.

2.4 Cleaving, mounting and wire-bonding of the chips for characterization

At the end of the fabrication, the different chips are cleaved out from the wafer. In order to optimize the use of the wafer area, the size of cells of our mask design has been customized and varies from chip to chip.

Each device presented in this thesis requires a certain number of voltage and current sources in order to be controlled. The number of components that require voltage or current control varies from 22 to 26 depending on the chip. Two laser systems are present on some of the chips. In order to reduce the risk of damage caused by direct probing on the metal pads of the chip, a wire-bonding connection method has been used for the devices presented in this thesis.

The mounting system used during the characterization of the PICs is depicted in Fig. 2.5a. It consists of four parts: (1) an aluminum submount, (2) an aluminum block with a PCB on top which holds standard electrical connectors and has a row of wire-bonding pads, (3) a water-cooled copper chuck, (4) an aluminum base block.

The PIC is glued on the aluminum submount using an electrically and thermally conductive epoxy resin. The width of submount can be chosen to be equal to or slightly smaller than the width of the chip under test. In this way both sides of the PIC can be approached with lensed fibers or lenses. The submount is screwed to the PCB-block. The metal pads on the chip are connected individually through wire-bonding to the metal pads on the PCB. Each pad of a SOA is connected to one pad of the PCB through double or triple wire-bonding in order to optimize the uniformity of the current density in the SOA. A D-25 connector is present in the PCB-block to connect the PIC to the electronics (voltage and current suppliers). Metal strips connect the D-subminiature to the wire-bonding metal pads that are positioned to the edge of the PCB beside the PIC. Pin-1 of the D-subminiature is used as common ground. It is electrically connected to the aluminum of the PCB-block and consequently to the n-side metallization of the PIC. The PCB-block (2) and the aluminum submount with the wire-bonded chip (1) form a unit that can be handled easily, is convenient to connect and can be stored safely.

The PCB-block can be provided also with RF-pads connected to SMA connectors. A more complex version of this block is available especially for chips with a high number of metal pads. In this version (called “butterfly”) two PCBs are present (one at each side of the chip) in order to make the wire-bonding process easier (Fig. 2.5b). The PCB frequency response capabilities have not been tested separately.

The PCB-block is screwed to the aluminum base block in such a way that the submount is placed on the water-cooled copper chuck. The water-cooling system is used to remove the heat generated in the chip. Thermal grease is spread between the submount and the water-cooled copper chuck in order to facilitate the thermal dissipation. The mounting system is fixed on an optical table.

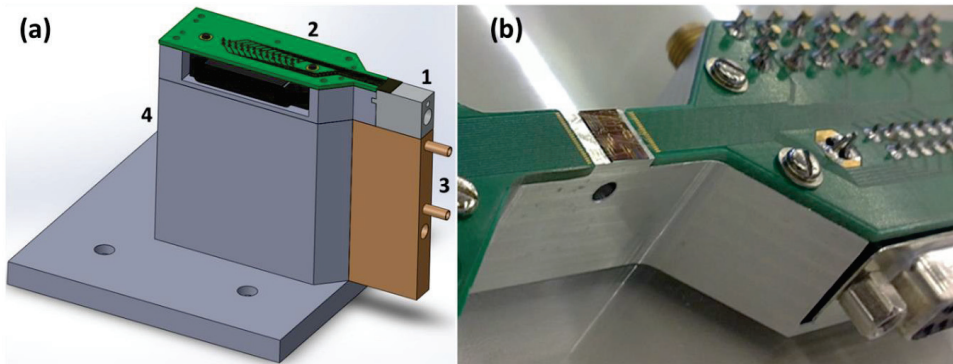


Fig. 2.5. (a) Schematic of the mounting system used during measurements. The four parts are numbered: (1) aluminum submount where the chip is glued, (2) PCB-block provided with D-connector, (3) water-cooled copper chuck, (4) aluminum base block. In (b) a picture of a chip glued and wire-bonded to a “butterfly” block is shown.

The described mounting system has been used successfully for the measurements on different chips over several months. This demonstrates that this approach simplifies the characterization of the PICs (especially if a large number of electrical connections is required) and reduces the risk of damage and the mechanical stress applied to the PIC, extending considerably its lifetime.

References

- [1] B. J. and S. Fathpour, “Silicon Photonics,” *IEEE J. Lighthw. Technol.*, vol. 24, no. 12, pp. 400-4615, Dec. 2006.
- [2] N.N. Ledentsov, “Long-wavelength quantum-dot lasers on GaAs substrates: from media to device concepts,” *IEEE Journal of Selected Topics in Quantum Electronics*, vol. 8, pp. 1015-1024, 2002,
- [3] M.K. Smit, An introduction to InP-based generic integration technology, (new paper)
- [4] J. van der Tol, R. Zhang, J. Pello, F. Bordas, G. Roelkens, H. Ambrosius, P. Thijs, F. Karouta, M. Smit, “Photonic integration in indium-phosphide membranes on silicon,” *Optoelectronics, IET*, vol.5, no.5, pp. 218-225, Oct. 2011.
- [5] Yamamoto M, Yamamoto N, Nakano J. MOVPE growth of strained InAsP/InGaAsP quantum-well structures for low-threshold 1.3- μm lasers. *IEEE J Quan Electron.* 1994;9:554–561
- [6] L. Coldren, S.W. Corzine, M.L. Mashanovitch “Diode lasers and photonic integrated circuits,” 2nd edition, Chichester : Wiley, 2012. Sections 1.4, 1.5, and 4.3.
- [7] Quantum dot heterostructures / Dieter Bimberg, Marius Grundmann and Nikolai N. Ledentsov Publisher Chichester : Wiley, 1999
- [8] M. Aoki, M. Suzuki, H. Sano, T. Kawano, T. Ido, R. Taniwatari, K. Uomi, and A. Takai, “InGaAs/InGaAsP MQW electroabsorption modulator integrated with a DFB laser fabricated by band-gap energy control selective area MOCVD,” *IEEE Journal of Quantum Electronics*, vol. 29, pp. 2088-2096, 1993.
- [9] E.J. Skogen, J.W. Raring, G.B. Morrison, C.S. Wang, V. Lal, M.L. Masanovic, and L.A. Coldren, “Monolithically integrated active components: a quantum-well intermixing approach,” *IEEE Journal of Selected Topics in Quantum Electronics*, vol. 11, pp. 343-355, 2005.

- [10] B. Mason, G.A. Fish, S.P. Den Baars, and L.A. Coldren, "Ridge waveguide sampled grating DBR lasers with 22-nm quasi-continuous tuning range," *IEEE Photonics Technology Letters*, vol. 10, pp. 1211-1213, 1998
- [11] J.J.M. Binsma, P.J.A. Thijs, T. v. Dongen, E.J. Jansen, A.A.M.T. Staring, G.N. v. d. Hoven, and L.F. Tiemeijer, "Characterization of butt-joint InGaAsP waveguides and their application to 1310 nm DBR-type MQW gain-clamped semiconductor optical amplifiers," *IECE TRANSACTIONS on Electronics*, vol. E80-C, pp. 675-681, 1997.
- [12] L. Xu, "Monolithic Integrated Reflective Transceiver in Indium Phosphide," PhD thesis, Technische Universiteit Eindhoven, The Netherlands, 2009.
- [13] Y. Barbarin, E. Bente, C. Marquet, E. Leclère, T. De Vries, P. Van Veldhoven, Y. Oei, R. Nötzel, M. Smit, and J. Binsma, "Butt-joint reflectivity and loss in InGaAsP/InP waveguides," in *Proc. 12th Eur. Conf. on Int. Opt. (ECIO 2005)*, pp. 406-409, Grenoble, France, Apr. 2005.
- [14] P.J.A. Thijs, "Strained-layer InGaAs(P)/InP Quantum Well Semiconductor Lasers Grown by Organometallic Vapour Phase Epitaxy", Technische Universiteit Delft, The Netherlands, 1994.
- [15] JePPIX website <http://www.jepix.eu/>
- [16] B.W. Tilma, "Integrated tunable quantum-dot laser for optical coherence tomography in the 1.7 μm wavelength region," PhD thesis, Technische Universiteit Eindhoven, The Netherlands, 2011.
- [17] J.H. den Besten, "Integration of Multiwavelength Lasers with Fast Electro-Optical Modulators," PhD thesis, Technische Universiteit Eindhoven, The Netherlands, 2004.
- [18] Y. Jiao, "Towards a monolithically integrated swept-source optical coherence tomography system in the 1.7 μm wavelength region," PhD thesis, Technische Universiteit Eindhoven, The Netherlands, 2013.
- [19] M.J.R. Heck, "Ultrafast Integrated Semiconductor Laser Technology at 1.55 μm ," PhD thesis, Technische Universiteit Eindhoven, The Netherlands, 2008.
- [20] P.H. Lawyer and C.H. Fields, "Film stress versus plating rate for pulse-plated gold", HLR Laboratories, LCC, 2001.
- [21] Kohl, P. A. (2010) *Electrodeposition of Gold*, in *Modern Electroplating*, Fifth Edition (eds M. Schlesinger and M. Paunovic), John Wiley & Sons, Inc., Hoboken, NJ, USA.

Appendix to Chapter 2

In this appendix, the four ICP etch steps present in the fabrication process discussed in Chapter 2 are described in detail. These etch steps define the profile of the different waveguide structures integrated on chip. The calculations of the etching times are explained and the values of the expected etching depth are presented.

Etching rates and mask erosion

In the CH_4/H_2 ICP etch process used, the etching rate varies for the different materials on the wafer. The etching rates might change from one day to another, especially if maintenance operations have been performed in the meantime. However, the ratio between the different etching rates is constant. The etching rates for the ICP process presented in this thesis are:

- InP: $er_{\text{InP}} = (72 \pm 8) \text{ nm/min}$
- InGaAs: $er_{\text{InGaAs}} = (38.25 \pm 4.25) \text{ nm/min}$
- InGaAsP: $er_{\text{InGaAsP}} = (49.5 \pm 5.5) \text{ nm/min}$

In this appendix, the highest values of etching rates are used for the calculations:

- InP: $er_{\text{InP}} = 80 \text{ nm/min}$
- InGaAs: $er_{\text{InGaAs}} = 42.5 \text{ nm/min}$
- InGaAsP: $er_{\text{InGaAsP}} = 55 \text{ nm/min}$

During the etching process, a layer of SiN_x is used as hard mask. The SiN_x is slightly eroded by the ICP etching. It is important to take into account this mask erosion in order to establish the actual etch depth that has been achieved. This is due to the fact that the scanner profiler used to measure the etch depth only provides information about the relative etch depths. The mask erosion rate for the SiN_x is:

- SiN_x : $er_{\text{SiN}_x\text{mask}} = 3.5 \text{ nm/min}$

In the following calculations, the contact layers (E3-4, E3-5 and E3-6 in Table 2.1) is considered to be a uniform 300 nm InGaAs layer: the 20 nm of InGaAsP layers (E3-4 and E3-5) are considered as 20 nm of InGaAs. The reason for this approximation lies on the fact that during the layerstack determination it is not possible to discriminate between InGaAs and InGaAsP in the contact layers. For a similar reason, the 10 nm InP etch-stop layer embedded in the waveguide core is considered to be 10 nm of InGaAsP. Furthermore, the values of the etch depths are rounded to the nearest ten. These approximations lead to changes in the calculated etching times that are well within the uncertainty of the etching rate and of the surface profiler.

First InP ICP etch step

As mentioned above, the four ICP etch steps define the profile of the semiconductor material and the height differences among the various waveguide structures. In the following, h indicates a step height between two levels of the profile as it results after all the ICP etch steps. Subscripts from 1 to 4 are used to indicate the four etch steps that define each particular step height. As explained in Chapter 2 and summarized in Fig. A1:

- the first ICP etch step is used to create the difference between the bottom levels of the shallow and deep waveguide trenches (h_1);

- the second ICP etch step defines the difference between the top of the isolation sections and the bottom of the shallow waveguide trenches (h_2);
- the third ICP etch step results in the height difference between the top of the passive waveguides and the top of the isolation sections (h_3);
- the fourth ICP etch step defines the height difference between the top of the contact layer and the top of the passive waveguides (h_4).

During the first ICP etch step, the etching is performed only in the areas where the deep waveguide trenches have been designed: a SiN_x layer protects the deep waveguides. The other regions of the wafer are covered with a 3 μm thick layer of positive photoresist AZ4533.

In our technology, a shallowly etched structure has a low contrast ridge waveguide and a trench beside the waveguide ridge is etched down to 100 nm into the waveguide core. The trench beside a deeply etched waveguide is etched down to 200 nm below the waveguide core, as depicted in Fig. 2.1. Consequently, the first ICP etch step has to result in a difference of 600 nm between the bottom levels of the shallow and deep waveguide trenches:

$$h_1 = h_{1a} + h_{1b} \quad (\text{a.1})$$

where h_{1a} is a 200 nm InP layer of the bottom cladding (E1-2 and part of E1-1) and h_{1b} is a 400 nm thick InGaAsP layer of the waveguide core (E1-3, E1-4 and part of E2-1 in the passive layerstack, E1-3, E1-4, E1-5 and part of E1-6 in the active layerstack). These values do not consider the lag effect which is discussed at point 4 of section 2.2.2. The lag effect is taken into account in the calculations of the second ICP etch step.

Because of the different etching rates of the several layers, the actual depth d_1 that has to be etched from the top of the wafer when the first ICP etch step is performed, is not 600 nm. The difference between the bottom levels of the shallow and deep waveguide trenches includes 400 nm of InGaAsP (waveguide core) and 200 nm of InP (bottom cladding). Considering the etching rates listed above, the required etching time in the first ICP step is:

$$t_1 = t_{1a} + t_{1b} = \frac{h_{1a}}{er_{\text{InP}}} + \frac{h_{1b}}{er_{\text{InGaAsP}}} = \frac{200 \text{ nm}}{80 \text{ nm/min}} + \frac{400 \text{ nm}}{55 \text{ nm/min}} = (2.5 + 7.3) \text{ min} = 9.77 \text{ min} \quad (\text{a.2})$$

Thus, after etching for 9 minutes and 46 seconds, we will obtain an etch depth that after all the ICP etch steps will result in the designed difference between the bottom levels of the shallow and deep waveguide trenches.

Obviously, the etching starts at the top of the contact layer. In the following d is used for the actual depths of the etching performed during the ICP steps. The etch depths indicated with d should not be confused with step heights (h_1 , h_2 , h_3 , h_4) obtained at the end of the fabrication process.

The time necessary to etch through the whole contact layer is:

$$t_{\text{contact}} = \frac{d_{\text{contact}}}{er_{\text{InGaAs}}} = \frac{300 \text{ nm}}{42.5 \text{ nm/min}} = 7.06 \text{ min} \quad (\text{a.3})$$

where $d_{contact}$ is the total thickness of the contact layer (E3-4, E3-5 and E3-6). The etching time can be written as:

$$t_1 = t_{1a} + t_{1b} = t_{contact} + t_{1\gamma} \quad (a.4)$$

where $t_{1\gamma}$ is the time spent etching the top cladding in the first ICP etch step.

This means that after 7 minutes and 3~4 seconds, the etching reaches the top cladding. The time left for the first ICP etching is:

$$t_{1\gamma} = t_1 - t_{contact} = 2.71 \text{ min} \quad (a.5)$$

Consequently, at the end of the first ICP etch step, the part of top cladding (part of E3-3) that has been etched is:

$$d_{1\gamma} = t_{1\gamma} \cdot er_{1np} = 2.71 \text{ min} \cdot 80 \text{ nm/min} = 217 \text{ nm} \cong 220 \text{ nm} \quad (a.5)$$

which means that, in total, the etch depth from the top of the contact layer is:

$$d_1 = d_{contact} + d_{1\gamma} = 520 \text{ nm} \quad (a.6)$$

To summarize, in order to obtain a difference between the bottom levels of the shallow and deep waveguide trenches equal to 600 nm (without considering the lag effect), a etch depth of 520 nm from the top of the contact layer has to be achieved at the end of the first ICP etch step.

The etch depth is verified with a surface profiler. Since a SiN_x hard mask is used during the ICP etching process, the thickness of this layer and its erosion must be taken into account while measuring the etch depth. The initial thickness of the SiN_x is $d_{\text{SiN}_x} = 600 \text{ nm}$. The actual value is measured with the surface profiler after the dry CHF_3 RIE process (see point 1 of section 2.2.2). Considering the mask erosion, the total depth to be measured from the top of the partially eroded hard mask after the first ICP etch step is:

$$d_{profiter_1} = d_1 + d_{\text{SiN}_x} - t_1 \cdot er_{\text{SiN}_x\text{mask}} = 1086 \text{ nm} \cong 1090 \text{ nm} \quad (a.7)$$

Second InP ICP etch step

In the second ICP etch step, the height difference between the top of the isolation sections and the bottom of the shallow waveguide trenches is defined (h_2). Taking into account a lag effect h_{lag} equal to 80 nm, this etching has to result, after all the ICP etching process, in a depth equal to:

$$h_2 = h_{2a} + h_{lag} + h_{2b} = (100 + 80 + 320) \text{ nm} = 500 \text{ nm} \quad (a.8)$$

where h_{2a} is the depth of the shallow waveguide trenches into the waveguide core in case of negligible lag effect (part of E2-1 in the passive layerstack, part of E1-7 in the active layerstack) and h_{2b} is the thickness of the top cladding left on top of an isolation section (E2-2, E3-1 and part of E3-2 in the passive layerstack, E1-8, E3-1 and part of E3-2 in the active layerstack,).

The etching time is:

$$t_2 = \frac{h_{2a}}{er_{InGaAsP}} + \frac{h_{lag}}{er_{InGaAsP}} + \frac{h_{2b}}{er_{InP}} = \frac{180 \text{ nm}}{55 \text{ nm/min}} + \frac{320 \text{ nm}}{80 \text{ nm/min}} = 7.27 \text{ min} \quad (\text{a.9.})$$

The etch depth from the top of the contact layer in a shallow structure trench after the second ICP etch step is:

$$d_2 = d_{contact} + d_{2\gamma} = d_{contact} + (t_2 - t_{contact}) \cdot er_{InP} \cong 320 \text{ nm} \quad (\text{a.10})$$

where $d_{2\gamma}$ is the part of top cladding (part of E3-3) actually etched during the second ICP etch step. Taking into account the mask erosion, after the second ICP etch step, the depth to be measured in the shallow waveguide trenches is

$$d_{profiler_2} = d_2 + d_{SiN_x} - t_2 \cdot er_{SiN_xmask} \cong 890 \text{ nm} \quad (\text{a.11.})$$

In the calculations of the first ICP etch step above, h_{1a} is considered equal to 400 nm. This is due to the fact that no lag effect is taken into account. However, in the second ICP etch step, we consider a lag effect of 80 nm. As a consequence, we can recalculate the values of h_{1a} and h_{1b} .

$$h_{1b}^* = h_{1b} - h_{lag} = 320 \text{ nm} \quad (\text{a.12})$$

The new value of h_{InP_1st} can be found as:

$$h_{1a}^* = h_{1a} + h_{lag} \cdot \frac{er_{InP}}{er_{InGaAsP}} \cong 320 \text{ nm} \quad (\text{a.13})$$

In this way, we automatically compensate for the lag effect that is also present in the deep waveguides and where it is slightly larger than in the shallow ones. This means that close to the deep waveguide ridge, the bottom of the trench is around 200 nm into the bottom cladding.

If this compensation is not required, the value of h_{lag} must be taken into account in the calculations of the first ICP etch step, reducing the value of h_{1b} to 320 nm and consequently shortening t_1 .

Third InP ICP etch step

The third ICP etch step defines the height difference between the top of the passive waveguides and the top of the isolation sections (h_3). This etching goes through only one material: the InP of the top cladding (part of E3-3 and part of E3-2).

$$h_3 = d_3 = 1080 \text{ nm} \quad (\text{a.14})$$

where d_3 is the total depth etched during the third ICP etch step. The etching time is:

$$t_3 = \frac{h_3}{er_{InP}} = 13.5 \text{ min} \quad (\text{a.15.})$$

Taking into account the mask erosion, after the third ICP etch step, the depth to be measured in the shallow waveguide trenches is

$$d_{profiler_3} = d_{profiler_2} + d_3 - t_3 \cdot er_{SiNx_mask} \cong 1920 \text{ nm} \quad (\text{a.16}).$$

Fourth InP ICP etch step

The last ICP etch step defines the height difference between the top of the shallow waveguides and the top of the contact layer (e.g., the top of a PHM structure) and it corresponds to:

$$h_4 = h_{4a} + h_{4b} = 100 \text{ nm} + h_{contact} = 400 \text{ nm} \quad (\text{a.17})$$

where $h_{4b} = h_{contact} = d_{contact}$ (E3-4, E3-5 and E3-6) and h_{4a} is the top part of the top cladding (part of E3-3).

The etching time is:

$$t_4 = t_{contact} + \frac{h_{4a}}{er_{InP}} = 7.06 \text{ min} + \frac{100 \text{ nm}}{80 \text{ nm/min}} \cong 8.3 \text{ min} \quad (\text{a.18}).$$

During this last etch depth, in the shallowly etched structure trenches, the bottom part of top cladding ($d_{4\gamma} = 400 \text{ nm}$, E2-2, E3-1 and part of E3-2 in the passive layerstack, E1-8, E3-1 and part of E3-2 in the active layerstack) is etched followed by 180 nm of waveguide core (part of E2-1 in the passive layerstack, E1-7 and part of E1-6 in the active layerstack). The time spent to etch 400 nm of top cladding is:

$$t_{4\gamma} = \frac{d_{4\gamma}}{er_{InP}} = \frac{400 \text{ nm}}{80 \text{ nm/min}} = 5 \text{ min} \quad (\text{a.19}).$$

The time left (that is spent etching the waveguide core) is:

$$t_{4\delta} = t_4 - t_{4\gamma} \cong 3.3 \text{ min} \quad (\text{a.20}).$$

The amount of waveguide core etched is:

$$d_{4\delta} = t_{4\delta} \cdot er_{InGaAsP} \cong 180 \text{ nm} \quad (\text{a.21}).$$

The fact that $d_{4\delta} = h_{2a} + h_{1ag}$ means that the calculations are correct and that the target final depth for the shallowly etched structure should be reached.

Taking into account the mask erosion, after all the ICP steps, the depth to be measured in the shallow waveguide trenches is

$$d_{profiler_end} = d_{profiler_3rd} + d_{4\gamma} + d_{4\delta} - t_4 \cdot er_{SiNx_mask} \cong 2470 \text{ nm} \quad (\text{a.22})$$


which can be also written as:

$$d_{profiler_end} = d_{SiNx} + h_{contact} + h_{topclad} + h_{2a} + h_{1ag} - t_{sh_tot} \cdot er_{SiNx_mask} \quad (\text{a.23})$$

where $h_{topclad}$ is the total thickness of the top cladding and t_{sh_tot} is the total etch time for the shallow waveguide trenches:

$$t_{sh_tot} = t_2 + t_3 + t_4 \quad (a.24).$$

The etching is done in series of 1 minute cycles that are alternated by the O₂-descum process used to clean the sample from polymers that are deposited on the surface during the etching process. An etching process of 9 minutes and 16 seconds, for example, is done with 9 cycles of 1 minute plus a shorter final cycle.

In Fig. A1 the cross-sections of the five waveguide structures integrated on chip. From left to right: SOA (PD), PHM, shallow waveguide, isolation section, deep waveguide. The  columns indicate the height differences between the different structures. The corresponding etching steps and etching times are listed in the upper part of the figure. On the right hand side, the values of the height differences are presented together with the thickness of the different layers of the layerstack.

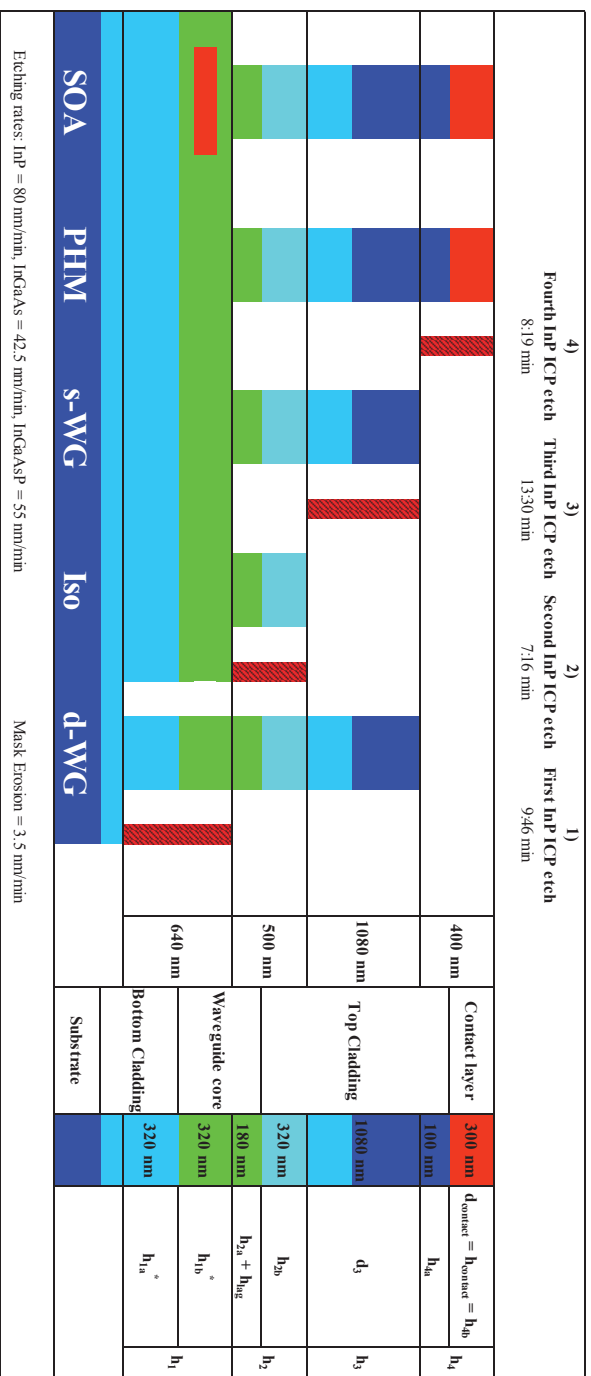


Fig. A1. Cross-sections of the five waveguide structures integrated on chip. From left to right: SOA (PD), PHM, shallow waveguide, isolation section, deep waveguide. The columns indicate the height differences between the different structures. The corresponding etching steps and etching times are listed in the upper part of the figure. On the right side, the values of the height differences are presented together with the thickness of the different layers of the layerstack. The color code is the same of Table 2.1. In this figure, the 10 nm of InP etch-stop layer embedded in the waveguide core is considered to be 10 nm of InGaAsP.

CHAPTER 3

Design choices

Abstract – In this chapter, the main design choices for the devices presented in Chapter 4 and Chapter 5 are explained. Both linear and ring configurations are discussed. The advantages of exploiting an AWG as intra-cavity filter are listed. Constructions based on voltage controlled electro-optic phase modulators are used for fine tuning and for controlling the power of the two modes. On chip photodetectors are designed to monitor the power of λ_1 and λ_2 . A feedback control circuit which exploits the signals extracted from the photodetectors is proposed.

3.1 Linear laser configuration

As discussed in section 1.4.3, in a dual-wavelength laser with a single common SOA, on one hand, the laser cavities of λ_1 and λ_2 need to be partially separated, on the other hand, they have to share the arm of the device where the amplifier is placed. As a consequence, a key component is required to connect the two laser cavities and combine λ_1 and λ_2 . There are several options available for this purpose on InP integration technology, e.g. an unbalanced Mach-Zehnder interferometer (MZI) or an AWG. Fig. 3.1(a) shows the basic scheme for a linear laser cavity in which an AWG is used as intra-cavity filter to allow lasing on two wavelengths within a common arm of the device. The use of an AWG has three main advantages [1]. Firstly, it connects Channel 1 and Channel 2 to the common channel of the device allowing the delivery of light at the available wavelengths simultaneously into the same output waveguide. Secondly, the AWG also determines the coarse tuning of the two wavelengths. This provides a high stability in terms of frequency difference between λ_1 and λ_2 with respect to the temperature: when the temperature of the AWG changes, the difference in frequency between its transmission channels remains nearly the same [2]. Thirdly, thanks to its highly selective transmission function, the AWG attenuates a significant part of the amplified spontaneous emission (ASE) in the laser cavity, reducing the ASE contribution to the enhancement of the linewidth of the lasing wavelengths. Indeed, lasers with intra-cavity AWG have shown optical linewidth down to 130 kHz [3].

Since the optical losses of the cavities of λ_1 and λ_2 need to be controlled to balance the power of the two wavelengths, the simple configuration depicted in Fig. 3.1(a) is not suitable for dual-wavelength operation. In case the two wavelengths experience differences in roundtrip losses of even a fraction of a dB, gain competition would make it so that most of output power would end up in one of the two modes.

In order to obtain equalized power between λ_1 and λ_2 , the intra-cavity loss for the two wavelengths needs to be controlled actively. One possible option is presented in Fig. 3.1(b) where a short SOA is positioned in each individual channel of the device. This solution allows for separate control of each of the wavelengths and for balancing the power between λ_1 and λ_2 . Unfortunately

there are at least three drawbacks on implementing this configuration. First of all, the short SOAs have a current dependent gain spectrum which would influence the cavity mode selection. A second disadvantage is that each short SOA would add ASE noise and other technical noise to the corresponding wavelength (and these noise sources would be different for each channel). This leads to keeping these SOAs as short as possible, reaching the third drawback, since at the moment the shortest SOA that can be fabricated in the generic photonic InP-based integration technology is 50 μm long.

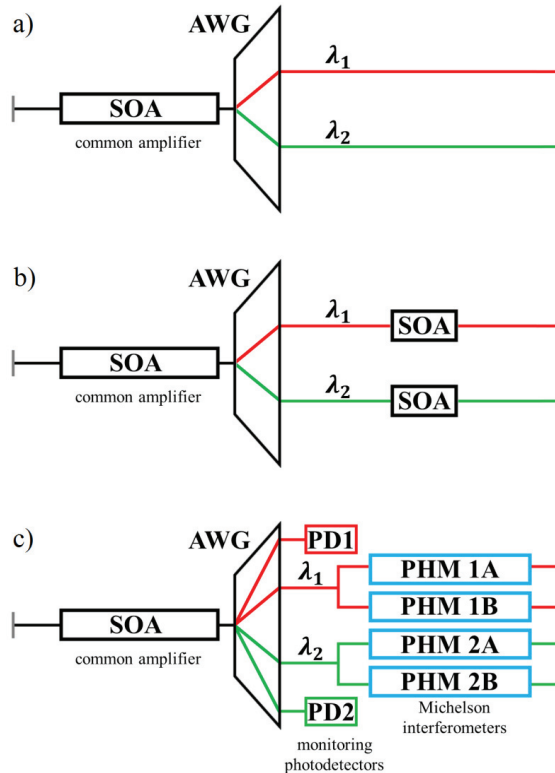


Fig. 3.1. (a) Basic scheme of a linear laser in which an AWG is used as intra-cavity filter. (b) Configuration in which one SOA has been added to each single channel in order to independently control the power of λ_1 and λ_2 . In (c) each individual channel is provided with a Michelson interferometer (MI). Monitoring PDs are connected to a higher order of the AWG.

A more interesting option is to use voltage controlled electro-optic phase modulators (PHMs). Since the current passing through this type of PHM is typically in the nA to μA range, low power (in the order of μW) is needed to control it. As a consequence, the heat dissipation in the PHM is minimal and thermal effects on the laser cavity are negligible. As depicted in Fig. 3.1(c), PHMs can be used to create a balanced Michelson Interferometer (MI) in each individual channel. Such a configuration allows for fine tuning the frequency of λ_1 and λ_2 within the AWG transmission channel and also to control the intra-cavity loss in each channel. If we consider channel 1, a voltage

offset applied to both PHMs of the channel (PHM 1A and PHM 1B) controls the optical length of the laser cavity of λ_1 and the laser cavity modes can be tuned within a fraction of the cavity mode spacing. By applying a differential signal between PHM 1A and PHM 1B, a difference between the phases of the signals travelling through the two arms of the MI can be introduced without tuning the cavity length. In this way, the optical losses in the cavity, and consequently the amplitude of λ_1 , can be controlled. Thus, through control of the voltages applied to all the PHMs of the device, the amplitude of the two wavelengths can be balanced and the difference in frequency between λ_1 and λ_2 can be finely tuned. As discussed in more detail in section 3.1.2, the tuning range depends on the SMSR required and consequently on the channel width of the AWG and on the length of the laser cavity. Thus, the tuning will always be less than the free spectral range of the cavity for each of the channels. The control on the amplitude and the control on the tuning are in principle independent if the arms of each MI are perfectly balanced.

In order to derive the control signals for balancing the power levels, PDs can be integrated with the system for monitoring the power at λ_1 and λ_2 . A convenient way of getting access to light in the two channels for monitoring purposes is to use the power in the higher order outputs from the AWG, exploiting the periodic behavior of this component. The difference signal from the two photodiodes PD1 and PD2 can be used to generate the feedback signal for the loss control system in order to balance the power between the two lasing modes. We have studied such a feedback scheme theoretically using a differential equation model for the laser in which the cavity average photon densities in the two modes and the average carrier density in the amplifier are described as well as the feedback signal on a loss modulator in the wavelength channel with the lowest loss. In the model, the feedback is applied with a specified fixed delay time. This analysis has shown that an electronic feedback circuit used to balance the power of λ_1 and λ_2 , must be partially proportional and partially integrating. A pure integrating feedback signal always leads to an unstable situation with periodically varying power ratio. Furthermore it was found that there is no minimum bandwidth required for adjusting the losses in the cavity. Of course there is a trade-off between the bandwidth of the circuit and the speed at which the system becomes stable. The feedback system model is explained in detail in section 3.4.

3.2 Ring laser configuration

In this section, the ring configuration of a single-SOA-based dual-wavelength laser is presented. The added benefit of a ring laser is an increased SMSR. If the laser operates in unidirectional way, the spatial-hole-burning is avoided since there is no standing wave inside the laser cavity. As presented in Fig. 3.2, starting from Fig. 3.1(c), a ring configuration can be designed using an MMI tree to transform the MIs in MZIs and to reconnect Channel 1 and Channel 2 into a single waveguide. A 2x2-MMI is used to couple the light out from the ring cavity.

As discussed in detail in section 4.2, the design of one output waveguide (primary output) is optimized to reduce back-reflections inside the cavity. The other output of the 2x2 MMI (secondary output) is used to send feedback to the cavity and force the laser to work in the clockwise direction. The reason for this design choice is to increase the signal power received by the PDs.

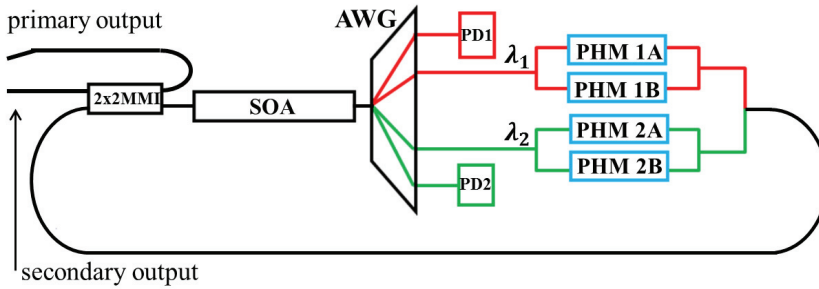


Fig. 3.2. Schematic of the ring single-SOA AWG-based dual-wavelength laser.

3.3 Laser model: tuning and power balance control

As mentioned in section 3.1, active control of the power at λ_1 and λ_2 is required since the two modes are generated and amplified by the same SOA. For this reason, the laser cavities of λ_1 and λ_2 must be partially separated and the components used to control the losses (and consequently the power) in the channel must be placed in these separated parts of the circuit. As depicted in Fig. 3.1 and Fig. 3.2, the PHMs used to control the losses in each individual channel are in Michelson configuration in the linear design and in Mach-Zehnder configuration in the ring design.

In order to show the principle of operation of the loss and tuning control function for one wavelength, a simple steady state model of one channel of the laser is used. The schematic of the simulated part of device is depicted in Fig. 3.3: it is a single channel of the linear laser configuration and it includes the end mirrors for the laser cavity, the common arm of the device with the SOA, the AWG, and one of the individual channels.

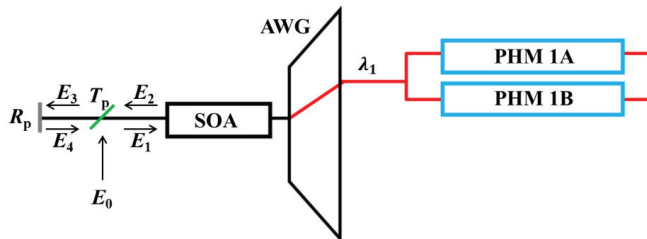


Fig. 3.3. Schematic of a single channel in a linear laser device as modelled to demonstrate the use of a MI or MZI to control the losses in an individual channel.

The electric field A at a specific location in the laser and for a specific wavelength can be described as $A(\omega, t) = \text{Re}(E \cdot e^{i\omega t})$. In this model, we calculate steady state electric field complex amplitude E_1 in the cavity at the output coupler for a range of wavelengths. All components are described as linear optical components with $E_{\text{out}} = T \cdot E_{\text{in}}$ where E_{in} and E_{out} are the complex field amplitudes going in and out, T is a complex number that describes the effect of the component, i.e. the SOA, the AWG and the two PHMs in the Michelson interferometer. The gain in the SOA and the phase shift in the phase modulators are parameters in the model. The ASE in the system is

modelled by positioning a beam splitter in the model cavity with a low power reflectivity of $(1-T_p)$, which couples in light from an external monochromatic source of wavelength λ .

The transmission of the AWG and the SOA are thus described in a simplified way. At this stage this is sufficient for explaining the intended use of the PHMs in the Michelson configuration to control the power and tuning in one channel.

In the following, the equations that describe the transmission of the complex electrical field amplitude for the passive waveguide, the SOA, the AWG, and the PHMs are presented. The transmission of the electric field through a passive waveguide is described by the factor:

$$T_{wg} = e^{i \cdot \left(\frac{2 \cdot \pi \cdot n_g}{\lambda} + i \cdot att_dB \cdot 0.05 \cdot \ln(10) \right) \cdot L} \quad (3.1)$$

where L is the total length of passive waveguide in the cavity, λ is the wavelength, n_g is the effective group index, att_dB is the power attenuation in dB per meter. For the SOA the following factor is used:

$$T_{SOA} = e^{i \cdot \left(\frac{2 \cdot \pi \cdot n_g}{\lambda} \cdot L_{SOA} - i \cdot gL \right)} \quad (3.2)$$

where gL is the total exponential gain coefficient in units of m^{-1} and L_{SOA} is the length of the SOA. The transmission of a single AWG channel is described by:

$$T_{AWG} = e^{[-\ln(2) \cdot 2 \cdot \left(\frac{\lambda - \lambda_c}{I_{FWHM}} \right)^2]} \cdot e^{i \cdot \left(\frac{2 \cdot \pi \cdot n_g}{\lambda} \cdot L_{AWG} + i \cdot loss_{AWG} \cdot 0.05 \cdot \ln(10) \right)} \quad (3.3)$$

where λ_c is the central wavelength of the AWG, I_{FWHM} is the width of the channel at FWHM in the wavelength domain, L_{AWG} is the effective pathlength of the AWG and $loss_{AWG}$ is the total excess loss of the AWG in dB. Finally for a PHM we use:

$$T_{phm} = e^{i \cdot \left(\frac{2 \cdot \pi \cdot n_g}{\lambda} \cdot L + \Delta\phi \right)} \quad (3.4)$$

where $\Delta\phi$ is the phase shift caused by the voltage applied to the PHM and L_{phm} is the length of the PHM.

If the PHMs have identical length, the total length of the linear cavity becomes $L_{SOA} + L_{AWG} + L_{wg} + L_{phm}$. The relation between the electric field amplitude E_1 going into the SOA and the field E_2 coming back from the SOA can then be written as:

$$E_2 = E_1 \cdot F \quad F = T_{SOA}^2 \cdot T_{wg}^2 \cdot T_{AWG}^2 \cdot \frac{1}{2} (T_{phm1}^2 + T_{phm2}^2) \quad (3.5)$$

Here it is assumed that the reflectors on the right hand side of the cavity are highly reflecting. Note that the lengths of the two PHMs do not need to be the same. The model allows for taking into account a difference in length between them to describe an imbalance due to fabrication tolerances or by chosen design.

The other relations between the complex electric field amplitudes are then:

$$\begin{aligned}
E_1 &= E_0 \sqrt{1 - T_p} + E_4 \sqrt{T_p} \\
E_3 &= E_2 \sqrt{T_p} \\
E_4 &= E_3 \sqrt{R_p}
\end{aligned} \tag{3.6}$$

where R_p is the reflectivity of the facet on the left (common arm side). From the equations (3.5) and (3.6) one can solve for E_1 as a function of E_0 :

$$E_1 = \frac{\sqrt{1-T_p}}{1-T_p\sqrt{R_p}} E_0 \tag{3.7}$$

The spectrum of the simulated circuit (E_1 as a function of λ) can then be calculated by setting E_0 to 1 and calculating (3.7) for a range of wavelengths. Initially a low value for the gain in the SOA is chosen. Then, the spectrum of the laser at threshold can be calculated by increasing slowly the gain value until there is a wavelength where the value of E_1 approaches 1, or more precisely T_p . That wavelength is the one at which the laser will start to operate.

To demonstrate the tuning and the control of the loss in this laser circuit, laser spectra are calculated starting from a gain value below threshold when there is no additional phase delays set on the PHMs. Table 3.1 lists the values of the input parameters used for the model. The changes in the mode structure are shown in Fig. 3.4 and Fig. 3.5 where the resulting output spectra below threshold are depicted.

Symbol	Description	Value
L_{SOA}	SOA length	2 mm
L_{AWG}	AWG length	3 mm
L_{phm}	PHM length	2.5 mm
L_{wg}	Passive waveguides length	2 mm
T_p	Transmission fraction of the internal reflector	0.999
R_p	Reflectivity facet left hand side	0.3
n_g	Group refractive index	3.7
gL	SOA total exponential gain coefficient	0.46
λ_c	AWG central wavelength	1550 nm
$loss_{AWG}$	AWG losses	5 dB
I_{FWHM}	AWG channel FWHM	0.4 nm
E_0	ASE electric field spectrum	1

Table 3.1. Values of the input parameters used for the model of section 3.3.

Fig. 3.4a and Fig. 3.5a show the output power spectra of the circuit as a function of the phase shifts of the PHMs. The spectral intensity is color coded on a logarithmic scale. Fig. 3.4 depicts the case in which the phase shift set on PHM 1A is opposite that on PHM 1B. PHM 1A and PHM 1B are thus in anti-phase:

$$\Delta\phi_{1A} = -\Delta\phi_{1B} \quad (3.8).$$

The graph in Fig. 3.4 demonstrates that in this case the losses in Channel 1 can be adjusted and consequently the power at λ_1 can be controlled. At the 0 phase setting, the laser mode at 1550nm at the center of the AWG transmission channel is the most intense mode. When the phase values are increased, the suppression of the central mode can be seen. It is expected that only relatively small changes in loss are needed in order to balance the power of the two required laser modes in the real laser device. Another aspect to be noticed is that the laser mode is not tuned by controlling the phases in this way.

A length difference between the two arms tunes the minimum loss wavelength for the Michelson interferometer. It is therefore desirable to have the length of the arms in the interferometers as equal as possible. A few micrometers path length difference will not cause problems.

At a phase setting of $\pi/2$ the phase delay in one arm of the MI is π and in the other arm it is $-\pi$ because of the double pass of the MI. Thus the transmission loss is minimal at that point. The optical path length of the MI has however changed by $\lambda/2$ (double pass) and another set of cavity modes appear. We do not expect to have any issue in a real laser system due to this effect. In conclusion, the simulation suggests that the Michelson configuration of two PHMs can be used to control the power in one channel of a dual-wavelength laser system.

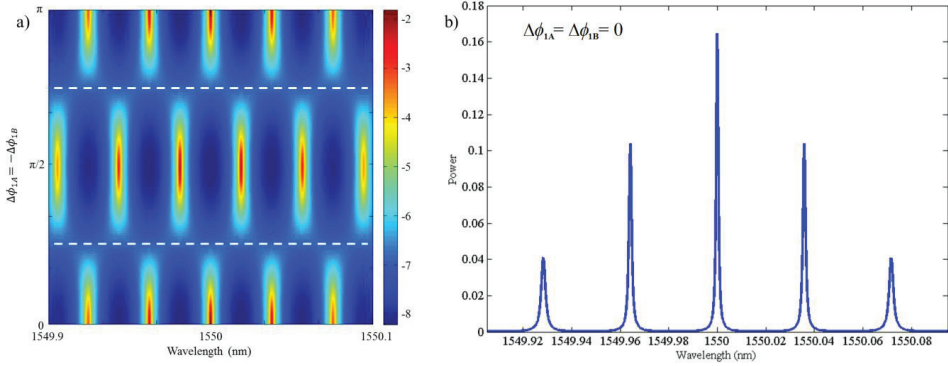


Fig. 3.4. Simulated output spectra of the circuit depicted in Fig. 3.3. a) The spectral power (in arbitrary units) is color coded using a logarithmic scale. On the y-axis, the phase shift of PHM 1A is varied from 0 to π in anti-phase compared to PHM 1B. The graph shows that in this way the intra-cavity loss of the lasing wavelength can be controlled without tuning the laser mode. b) Output spectrum (in arbitrary units on a linear scale) of the circuit when the phase shift of PHM 1A is equal to 0.

Fig. 3.5 shows the output power spectra in a color coded logarithmic scale as a function of the phase shift caused by the PHMs in the case when PHM 1A and PHM 1B are in phase:

$$\Delta\phi_{1A} = \Delta\phi_{1B} \quad (3.9).$$

In this case a tuning effect of the laser modes is produced. The changes in the power of the lasing mode are due to the filtering function of the AWG which does not change. In the laser, the

mode selection is a result of the combination of the fixed transmission spectrum of the AWG and the tuned longitudinal mode structure of the cavity. This causes the tuning function to be limited by mode hopping: there is a trade-off between the tuning and the SMSR.

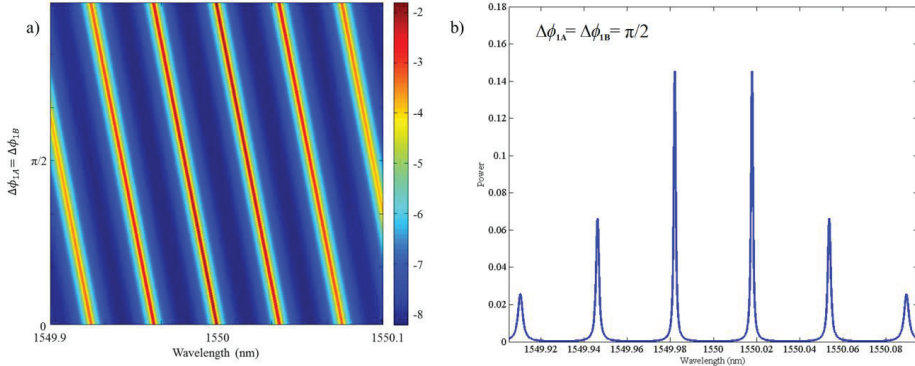


Fig. 3.5. Simulated output spectra of the circuit depicted in Fig. 3.3. a) On the y-axis, the phase shifts of PHM 1A and PHM are varied from 0 to π . The spectral intensity is presented on a log scale (in arbitrary units). The graph shows that in this way the lasing mode can be tuned. b) Output spectrum (in arbitrary units on a linear scale) of the circuit when $\Delta\phi_{1A} = \Delta\phi_{1B} = \pi/2$.

As mentioned above, idealizations have been used in this model:

- The gain of the SOA is kept constant: this is a reasonable approximation below threshold. In reality, a change in loss results in a change of the carrier concentration in the SOA and, thus, affects the tuning of the modes. However, the tuning would be nearly identical on both modes.
- The 2x1 MMI used for realizing the Michelson Interferometer has been considered perfectly balanced. A deviation from 50% splitting does not affect the tuning and loss control much since we mainly used the MI close to its transmission maximum. The extinction ratio is not very relevant.

Furthermore, in the example reported in Fig. 3.4 and Fig. 3.5, no length difference between the PHMs has been taken into account.

These idealizations have been applied in order to keep the model as simple as possible since at this stage the only goal of the model is to verify that a Michelson (or a Mach-Zehnder) construction of two PHMs can be used to control the losses and to tune the modes in one individual channel.

3.4 Monitoring photodetectors and feedback control

As discussed in section 3.3, in order to derive the control signals for balancing the power levels, photodetectors (PDs) can be integrated with the system for monitoring the power at λ_1 and λ_2 . A convenient way of getting access to light in the two channels for monitoring is to use the power in the higher order outputs from the AWG, thus exploiting the periodic behavior of this component. The difference signal from the two photodetectors PD1 and PD2 can be used to generate the feedback signal for the loss control system in order to balance the power between the

two lasing modes. The signal generated by such a feedback control system can be applied to the PHMs of one of the channels of the laser. We have studied such a feedback scheme using a time dependent differential equation model for the laser. In this model the average cavity photon densities of the two modes and the average carrier density in the amplifier are described as well as the time dependent loss that has to be generated by a loss modulator in the channel with the lowest losses. In the model, the feedback is applied with a specific fixed delay time for the control signal.

A block schematic of a proposed control system is depicted in Fig. 3.6. The schematics inside the dashed lines are a symbolic representation of the function and do not define a detailed electronics design.

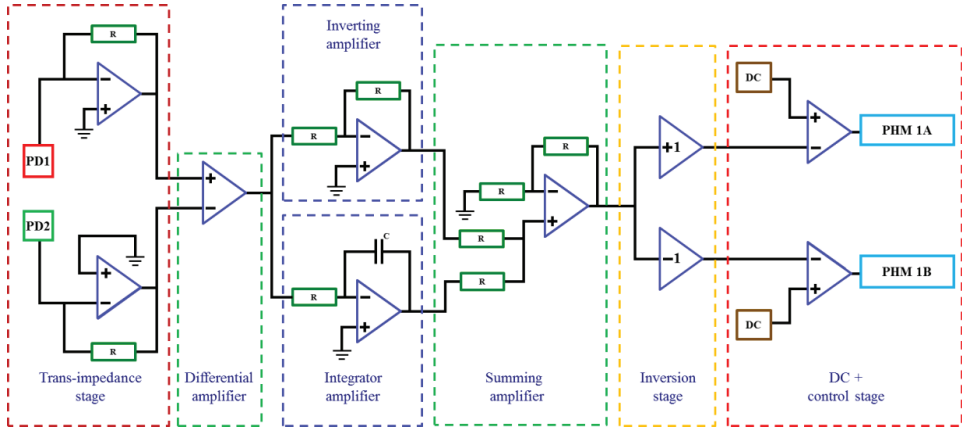


Fig. 3.6. Block schematic of a proposed control system. The currents from the PDs are the input signals from which the system derives the voltage signals that control the losses of Channel 1 through its PHMs. The schematics inside the dashed lines are a symbolic representation of the function and do not define a detailed electronics design.

A trans-impedance stage converts the current signals from PD1 and PD2 into voltage signals. A differential amplifier compares the two voltages and provides as an output a signal proportional to the power difference of the two longitudinal modes. A summing amplifier combines the signals from a Proportional-Integral (PI) stage composed of an inverting amplifier and an integrator amplifier. The inversion and the control stage combine the output of the summing amplifier with the DC signal that allows for tuning of the laser.

The model of the control system assumes that:

- the current signal from PD1 (PD2) is proportional to the power at λ_1 (λ_2). This means that we consider negligible the power present in Channel 1 (Channel 2) at wavelengths different from λ_1 (λ_2): the higher the SMSR and the lower the cross-talk in the AWG, the more correct this idealization is.
- the two waveguides that connect the higher order of the AWG to PD1 and PD2 have the same losses and the two photodetectors have the same quantum efficiency. This idealization does not affect the quality of the model because a parameter can be added to the model in order to compensate for the possible different efficiencies of the PDs and the different losses of the waveguides.

The model uses a set of differential equations describing two lasing modes in the amplifier, one at λ_1 and one at λ_2 . Six differential equations (3.10) are used to describe the system. The first two equations give the time derivative for the photon density P_1 and phase φ_1 of lasing mode 1. The third and fourth equations describe the time derivative for the photon density P_2 and phase φ_2 for lasing mode 2. The change in the phase of the envelope of mode 2 is a little bit different to that in mode 1. Since the phase changes are induced by a change in refractive index, the phase change in λ_1 and λ_2 are slightly different, depending on the ratio between λ_1 and λ_2 . The fifth equation describes the total carrier density N in the amplifier. The last equation in the set is the one for the time derivative of the delayed and normalized power difference between the two modes:

$$\begin{aligned}
 \frac{dP_1(t)}{dt} &= \frac{L_{SOA}}{L_{cav}} \cdot \Gamma \cdot v_g \cdot \sigma \cdot \frac{N(t)-N_0}{1+\epsilon_s(P_1(t)+P_2(t))} P_1(t) + (N(t))^2 \cdot B \cdot \Gamma \cdot \beta \cdot \frac{L_{SOA}}{L_{cav}} - P_1(t) \cdot Loss_1 \\
 \frac{d\varphi_1(t)}{dt} &= \frac{L_{SOA}}{L_{cav}} \cdot \Gamma \cdot \frac{\alpha}{2} \cdot v_g \cdot \sigma \cdot \frac{N-N_0}{1+\epsilon_s(P_1(t)+P_2(t))} \\
 \frac{dP_2(t)}{dt} &= \frac{L_{SOA}}{L_{cav}} \cdot \Gamma \cdot v_g \cdot \sigma \cdot \frac{N(t)-N_0}{1+\epsilon_s(P_1(t)+P_2(t))} P_2(t) + (N(t))^2 \cdot B \cdot \Gamma \cdot \beta \cdot \frac{L_{SOA}}{L_{cav}} - P_2(t) \cdot Loss_2 \\
 \frac{d\varphi_2(t)}{dt} &= \frac{L_{SOA}}{L_{cav}} \cdot \Gamma \cdot \frac{\alpha}{2} \cdot v_g \cdot \sigma \cdot \frac{N(t)-N_0}{1+\epsilon_s(P_1(t)+P_2(t))} \cdot \frac{\lambda_1}{\lambda_2} \\
 \frac{dN(t)}{dt} &= -v_g \cdot \sigma \cdot \frac{N(t)-N_0}{1+\epsilon_s(P_1(t)+P_2(t))} \cdot (P_1(t) + P_2(t)) - \frac{N}{\tau_n} - B \cdot (N(t))^2 - C_a \cdot (N(t))^3 + \frac{I_{SOA}(t)}{q_e \cdot S_{SOA} \cdot L_{SOA}} \\
 \frac{dP_{int}(t)}{dt} &= \frac{P_1(t-\Delta t) - P_2(t-\Delta t)}{P_1(t-\Delta t) + P_2(t-\Delta t)}
 \end{aligned} \tag{3.10}$$

Table 3.2 reports the meaning and the values of the constants used in the system of differential equations (3.10). The values for the SOA parameters are fairly typical values derived from e.g. [4]. The value of the gain non-linearity parameter has been increased by a factor of five from literature values to check if this would create any issues in the stability. The input parameters used in the model are listed in Table 3.3.

In the equations for the derivatives of P_1 and P_2 , the first term represents the optical gain. A linear gain model with gain compression is used. Note that this gain non-linearity in the theoretical predictions [5, 6] is expected to lead to instability for dual-mode lasing. The second term represents the spontaneous emission. The functions $Loss_1$ and $Loss_2$ in the third and last term are used to describe the losses in the two lasing modes. The losses in Channel 1 are partly dependent on the control signals:

$$\begin{aligned}
 Loss_1 &= CL_1 + \frac{\ln\left(\frac{P_{1t-\Delta t} - P_{2t-\Delta t}}{P_{1t-\Delta t} + P_{2t-\Delta t}}\right)^{prop+P_{diffn} \cdot int+1}}{T_{round}} \\
 Loss_2 &= CL_2
 \end{aligned} \tag{3.11}$$

where CL_1 and CL_2 represent the passive propagation losses for the corresponding modes and the loss caused by the output coupler of the laser cavity. CL_m is defined as

$$CL_m = \frac{-\ln(R_{oc}) + loss_{transm}}{T_{round}} \tag{3.12}$$

where R_{oc} is the reflectivity of the output coupler at the common arm side of the cavity (the model assumes that the other mirrors have 100% reflectivity). T_{round} is the cavity roundtrip time. The function $loss_{trans_m}$ describes the total passive propagation losses in the cavity and corresponds to

$$loss_{trans_m} = -\ln(tr_m) \quad (3.13)$$

where tr_m is the transmitted power fraction of the mode m ($m = 1$ or 2).

The second term in the right hand side of the equation of $Loss_1$ (3.11) describes how the feedback control adjusts the losses in the cavity to balance the power in the two lasing modes. In practice such control signal dependent loss can be implemented using e.g. the Michelson Interferometers as described in section 3.3.

Symbol	Description	Value
c	Speed of light	$3 \cdot 10^8 m/s$
h	Planck constant	$6.626 \cdot 10^{-34} J \cdot s$
σ	Linear gain coefficient	$4.229 \cdot 10^{-20} m^2$
n_g	Group refractive index	3.7
v_g	Group velocity	c/n_g
Γ	Confinement factor	0.08
N_0	Carrier transparency density	$1 \cdot 10^{24} m^{-3}$
ϵ	Nonlinear gain coefficient	$1.0 W^{-1}$
ωL	Radius beam waist	$0.5 \cdot 10^{-6} m$
S_{mode}	Area of the laser mode	$(\omega L)^2 \cdot \pi$
τ_n	Carrier lifetime	$0.598 \cdot 10^{-9} s$
β	Spontaneous emission coupling factor	$1 \cdot 10^{-5}$
B	Bimolecular recombination coefficient	$2.6202 \cdot 10^{-16} m^3/s$
C_a	Auger recombination coefficient	$5.269 \cdot 10^{-41} m^6/s$
α	Linewidth enhancement factor	3
$h\nu$	Photon energy	$h \frac{c}{\lambda}$
S_{SOA}	Area of the laser mode inside the SOA	$\Gamma \cdot S_{mode}$
q_e	Elementary charge	$1.6 \cdot 10^{-19} C$
ϵ_s	Gain compression factor	$3.02 \cdot 10^{23} phot \cdot m^{-3}$

Table 3.2. Values of constants and parameters used in the model of the feedback control system.

The model represents a PI controller with a time delay. Such a time delay will occur in the electronics of the optical loss controller. The proportional factor *prop* multiplies the normalized difference in power between the two modes (normalized by the total output power of the two modes) whereas the integral factor *int* multiplies the integrated time derivative of the normalized power

difference between the two modes. The time derivative of P_{int} is described by the sixth equation of the system (3.10).

Symbol	Description	Value
λ_c	Lasing wavelength	1550 nm
Δf	Frequency difference between the two modes	70 GHz
λ_1	Lambda of Channel 1	λ_c
λ_2	Lambda of Channel 2	$\frac{c}{\frac{c}{\lambda_1} + \Delta f}$
R_{oc}	Reflectivity of the common mirror	0.3
L_{cav}	Optical length of the cavity	10 mm
L_{SOA}	Optical length of the SOA	2 mm
T_{round}	Roundtrip time of the cavity	$\frac{L_{cav}}{2 \cdot v_g} = 92.5 \text{ ps}$
tr_1	Transmitted fraction of mode 1	0.7
tr_2	Transmitted fraction of mode 2	0.67
i	N. of integration points	10^4
T_{int}	Integration time	500 ns
Δt	Time delay	5 ns
$prop$	Proportional feedback factor	0.02
int	Differential feedback factor	$0.4 \cdot 10^6$
I	Injection current in SOA	250 mA
N_{start}	Initial carrier density	$1.28 \cdot 10^{24} \text{ m}^{-3}$

Table 3.3. Input values for the simulated laser model.

The equations are implemented in a computer program. A simple integration routine is used to solve the rate equations. Given as inputs the initial conditions for the six variables, the total integration time T_{int} , the number of points used in the integration. :

$$Y(t + \Delta t) = Y(t) + \Delta t \frac{dY}{dt} \quad (3.14).$$

The output intensity (power per square meter) is calculated using the formula:

$$Power_m = P_m \cdot c \cdot \frac{1-R_{oc}}{1+R_{oc}} \cdot h\nu \quad (3.15).$$

Finally, the model gives the instantaneous frequency of the modes, i.e. the time derivative of the phase of φ_1 and φ_2 .

The model has been used to demonstrate that a combination of a proportional and differential electronic feedback control circuit can be used to balance the power in the two modes present in the

laser cavity. In Table 3.3 the input values used in the simulation example are listed. The time delay value for the electronics is set to 5 ns. The initial carrier density has been set to $N_{start} = 1.28 \cdot 10^{24} m^{-3}$, which is close to the equilibrium value of the operating laser, in order to make the simulation faster.

Fig. 3.7a shows the power of the two modes as a function of time. After the initial start-up which takes approximately 15 ns, a stable situation is established where most of the power is in the low loss mode of Channel 1 while the mode of Channel 2 with higher passive loss is suppressed down to over 30dB lower. The feedback control starts to compensate for this difference and balances the power in the two channels in approximately 150 ns. The normalized power difference between P_1 and P_2 is presented in Fig. 3.7b. Using the input values listed in Table 3.3, the difference of power between the two modes is reduced to a value below 2 dB after 120 ns.

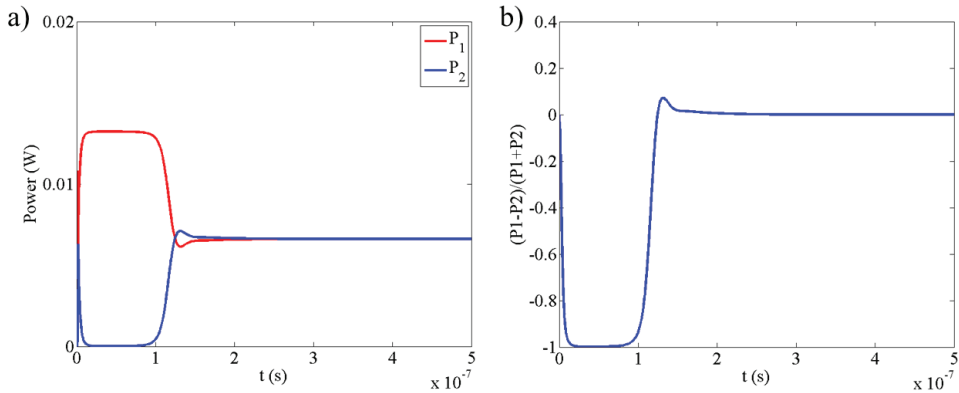


Fig. 3.7. (a) Power of the two modes of Channel 1 and Channel 2. (b) Normalized power difference between P_1 and P_2 .

In Fig. 3.8 the strength of the control loss signal is presented. This control signal is the term with the natural logarithm in equation 3.11. Initially the proportional part is almost constant at -0.02 while the integral part decreases rapidly from 0 to -0.043. Then, the value of the proportional factor increases and, after an overshoot, it tends to 0. These values have the same units as the CL_m variables. Characteristic of this dual-mode laser system is that the smaller the difference in power between the two modes, the smaller the loss differences required to change the balance between them. Because of this, a purely proportional control would always lead to an oscillating behavior between the two modes. The linear feedback factor can only slow down this oscillation but cannot suppress it.

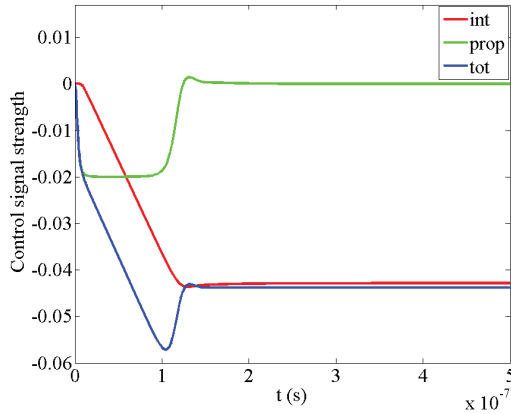


Fig. 3.8. Strength of the control loss signal in time (dimensionless). This is the term with the natural logarithm in equation 3.11. The green curve shows the proportional control signal, the red line the integrated control signal and the blue line shows the total control signal.

An important aspect is the influence of the operation of the control system on the frequency difference between the two laser modes. This is depicted in Fig. 3.9 together with the total control signal. Due to the control in loss, the group index in the SOA changes but both wavelengths experience nearly the same phase change. This is due to the fact that they are separated by only 120 GHz (~1 nm). The deviation that is just visible near $t = 120\text{ns}$ is approximately 4 kHz. This value is considerably below the expected linewidth of 100-200 kHz of the individual modes in a real system that is not actively wavelength stabilized.

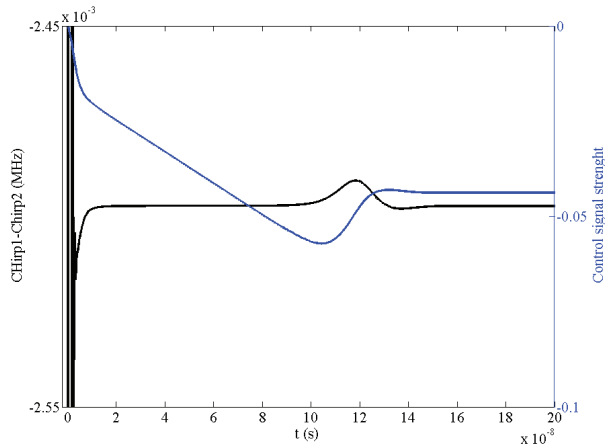


Fig. 3.9. Difference between the chirp, $(d\varphi_1/dt - d\varphi_2/dt)$ of the two modes (black line) and total control signal strength.

As discussed in section 3.3, the signals applied to the PHMs in the MZIs can be used to tune the two modes. As a consequence, the feedback control can also be used for the wavelength stabilization of the two modes to narrow down the linewidth.

From these initial modelling efforts, it can be concluded that it should be possible to design and operate a dual-mode laser as a stable system. The balance of the power in the two modes can be controlled accurately. Furthermore, exploiting the signals of on-chip PDs, a combination of proportional and integral electronic feedback circuit can be used to make the power balance control automatic. It is predicted that tuning of the frequency difference in the two modes is possible within limits fixed by the requirements for the SMSR since the mode selection is a result of the combination of the fixed transmission spectrum of the AWG and the tuned longitudinal mode structure of the cavity.

References

- [1] A. Corradi, G. Carpintero, B.W. Tilma, P.J. Thijs, M.K. Smit, and E.A.J.M. Bente, “Integrated dual-wavelength AWG-lasers for millimeter wave generation”, Proc. of the 16th ECIO, 2012.
- [2] X. Leijtens, B. Kuhlow, and M. Smit, “Wavelength Filters in Fiber Optics, ch. Arrayed Waveguide Gratings”, pp. 125–187. Springer Verlag, 2006. ISBN-13 978-3-540-31769-2.
- [3] G. Carpintero, E. Rouvalis, K. Lawniczuk, M. Fice, C.C. Renaud, X.J.M. Leijtens, E.A.J.M. Bente, M. Chitoui, F. van Dijk, and A.J. Seeds, “95 GHz millimeter wave signal generation using an arrayed waveguide grating dual wavelength semiconductor laser”, Optic Letters, vol. 37, no. 17, September 2012.
- [4] M. J. R. Heck, E. A. J. M. Bente, Y. Barbarin, A. Fryda, H.-D. Jung, Y.-S. Oei, R. Notzel, D. Lenstra, and M. K. Smit, “Characterization of a Monolithic Concatenated SOA/SA Waveguide Device for Picosecond Pulse Amplification and Shaping,” IEEE Journal of Quantum Electronics, vol. 44, no. 4, pp. 360–369, Apr. 2008.
- [5] L. Chusseau, F. Philippe, P. Viktorovitch and X. Letartre, “Mode competition in a dual-mode quantum-dot semiconductor microlaser”, Physical Review A, vol. 88, no. 1, 015803, July 2013.
- [6] L. Chusseau, F. Philippe, and F. Disanto, “Montecarlo modeling of the dual-mode regime in quantum-well and quantum-dot semiconductor lasers”, Optics Express, vol. 22, no. 5, 2014.

CHAPTER 4

Ring laser

Abstract – A series of dual mode ring lasers has been designed based on the calculations presented in Chapter 3 and has been fabricated by the author. In this chapter, we focus on the experimental results obtained from one of these dual mode ring lasers. In order to analyze the performance of the laser it was necessary to develop the theoretical description of the laser further.

4.1 Wafers and active-passive layout

The definition of the position of the active and passive regions on the wafer on which the devices are fabricated is the first design step. The layout of the mask that defines the active and the passive regions on a 2-inch wafer is depicted in Fig. 4.1. This mask has been used in the etch-back operation presented in section 2.2.1.

Four square regions can be identified in the central part of the layout. These are the so-called “usable chip areas” within which the actual devices have to be positioned. This choice has been made in order to allow for cleaving of the wafer in four parts (red dashed lines in Fig. 4.1). This is done right after the third epitaxial growth. Each quarter of the wafer can then be used separately to fabricate devices on it. Two issues must be taken into account when defining the usable chip areas. The first issue is that the quality of the epitaxial layers on the outermost part of a wafer is not suitable for device fabrication: in that area, the correct layer stack definition cannot be guaranteed because of the edge-effect during epitaxial growth. For this reason, each usable chip area lies 3.5 mm far from the edge of the wafer. The second issue is that in the device fabrication process, the layer of spun photoresist is not sufficiently uniform in areas within 3 mm from the edge of a sample. As a consequence, in order to allow for fabricating one quarter per time, 6 mm must be kept as minimum distance between two adjacent usable chip areas. As a result, considering that the wafer has a diameter of 2 inches, each usable chip area is 12.4 mm by 12.4 mm large.

The active/passive pattern is the same for all four quarters, but two of them have been rotated by 90 degrees with respect to the other two. These two orientations have been chosen for the following reasons. In order to exploit the available room on the quarters in the most efficient way, the PHMs must be parallel to the SOAs in our laser circuit. However, in the technology used, the butt-joint transitions between the active and the passive regions have the best quality when the SOAs are parallel to the large flat on the InP wafer whereas the phase modulators are more efficient if they are oriented perpendicularly to the large flat. With a rotation of 90 degrees of the pattern of two quarters, it is possible to have devices optimized for the butt-joints on the SOAs (minimum reflections) and devices optimized for the efficiency of the PHMs.

Inside each usable chip area, the active regions have been distributed in such a way that at least 8 devices (each with a different design) and 2 test structure chips can be designed. Due to lead times

on the fabrication of the wafers and the project deadlines for delivery of devices, the active-passive layout had to be designed much earlier than the actual device. The laser circuits, then, have been designed during the lead time of the specially grown wafers. The SOA blocks are 1, 2 and 3 mm long. Furthermore, 60 μm long active regions have been designed to be used PDs. Due to the optimization of the selective area growth process all the active regions must be designed 30 μm wide and the minimum distance between two active regions is 200 μm . Relatively large passive areas are available for positioning AWGs with 70 or 120 GHz channel spacing and 2 to 3 mm long phase modulators.

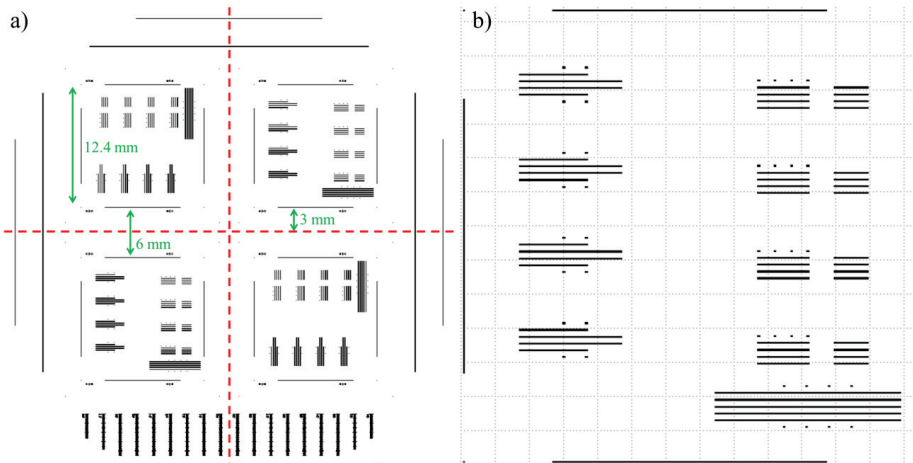


Fig. 4.1. a) Active passive layout of the 2-inch wafers used for device fabrication. The wafer can be cleaved through the dashed red lines if a fabrication in quarters is preferred. Each usable chip area is 12.4 mm by 12.4 mm large. The distance between two usable chip areas is 6 mm (3 mm distance from the cleaving area). The distance of each usable chip area from the edge of the wafer is 3.5 mm (not indicated in the figure). b) The layout of the active areas of one quarter in more detail. The dotted lines indicate a 1 mm grid.

The rulers at the bottom of the active-passive layout are used to align the mask plate to the large flat of the wafer before the very first photolithography step (see point (b) in section 2.2.1).

The long active regions designed at the sides and at the top of the active-passive layout are used for the coarse alignment of the following mask plates used in the device processing. The fine alignment is obtained thanks to specific markers.

The wafers have been bought from Philips Innovation Services at Philips MiPlaza at the High Tech Campus in Eindhoven. At the time we needed to acquire the wafers, Philips was the only available supplier on the market, to the best of our knowledge. Indeed, CIP Technologies had recently stopped the growth of this type of wafers and the wafers grown at that time at the Eindhoven University of Technology had too many defects. This issue turned out to be related to a particular choice of precursor gasses in the growth reactor. Since it was already known that Philips Innovation Services was planning to close down its III-V wafer growth facility, we decided to buy a quite large number of wafers in order to avoid the risk to face lack of material availability in the future. The choice to buy 12 wafers fabricated during three different growth runs has been done also with the purpose to spread the risk of the presence of unsuitable wafers among several samples. In

total three sets of four wafers were realised and delivered. The sets were with one, two or four quantum wells in the active region. In this thesis, in Chapter 4 and 6, we report only on devices with four quantum wells in the active regions.

The choice to work with QW-based wafers derives from the fact that QW-based gain medium have a gain bandwidth which more narrow than QD-based gain medium. AS a matter of fact, this helps to avoid simultaneous lasing effect through different order of the AWG, since the mode selection originates from the overlap between the gain curve and the filter function created by the AWG filter phase modulator construction, as explained in the following sections of this chapter.

4.2 Ring laser design

Several devices and test structures have been designed to be processed on a single quarter of the wafer: four ring lasers, three linear lasers, a series of passive test structures (e.g., AWG, deep and shallow waveguides) and sectioned SOA structures designed for gain measurements. Furthermore, 30% of each usable chip area has been used for lasers designed by the iPHOS project partner Universidad Carlos III De Madrid [1].

Mask Engineer from Phoenix BV and Klayout have been used as software tools for the circuit design and the mask design. The Cobra-TUe library embedded in Mask Engineer has been exploited for the design of the components (e.g., AWG).

In Fig. 4.2 the schematic of a ring configuration is depicted (a) together with the mask design of one of the ring lasers (b). For the sake of clarity, the layers corresponding to the masks of the polyimide and the silica have been removed from the picture. The principle of operation and the main design choices of the ring laser configuration are described in section 3.2. Different versions of ring lasers have been implemented. Variations among the different devices are on: the length of the SOA (2 or 3 mm); the presence of a Mach-Zehnder Modulator (MZM) and/or an SOA in the output waveguide; the position of the 2x2 MMI used as output coupler from the ring cavity. In this chapter, we focus on the analysis of the devices depicted in Fig. 4.2b. In this configuration, the output coupler (2x2 MMI) is placed between the SOA and the AWG. Since the laser is designed to work in the clockwise direction, the choice to place the output coupler after the SOA allows for maximizing the output power at what is indicated as the primary output. The MZM at the primary output can be used e.g. for data modulation. Other devices have been provided (also) with an output SOA that could be used as booster amplifier to increase the output power of the signal. The disadvantage of having a MZM and/or an SOA is the risk that reflections (or ASE, in the case of the SOA) coupled back into the cavity laser affect the functioning of the device making the control more complicated. Several extensions are present in the mask design of the ring laser that we discuss in this chapter (Fig. 4.2b) compared to the block schematic (Fig. 4.2a): these extensions are explained below in this section.

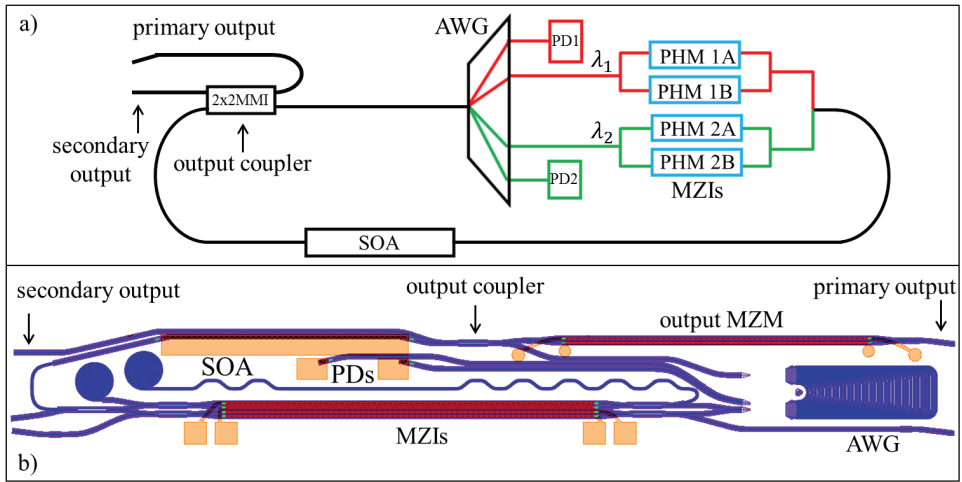


Fig. 4.2. a) Block schematic of a ring laser configuration. b) Mask design of the ring laser analyzed in this chapter. The color code used in (b) is the standard one for the mask designs in the COBRA platform. Polyimide and silica layer are not shown in the picture. The position of the output coupler is different in (a) and in (b) in order to show the examples of two different ring configuration. Furthermore, several extensions are present in the mask design compared to the block schematic (explained in the text of this section). The ring cavity is 15 mm long, the length of the SOA is 2 mm, and the PHMs of the MZIs are 3 mm long whereas the length of the PHMs used in the output MZM is 2.5 mm.

The ring cavity is 15 mm long, thus a mode spacing of 5.5 GHz is predicted. Both shallow and deep waveguides are present. All the curved waveguides except for those in the AWG have been designed to be adiabatic. In this way, offsets between straight and curved waveguides can be avoided, reducing the risk of internal reflections.

The AWG is the pivotal component of the device. The choice to select the orthogonal version of the AWG is twofold. This version of AWG is smaller than the Alcatel and the Smit ones (the input design parameters being equal). Moreover, the orthogonal version is the one that has been used more extensively during the last years; as a consequence, considerable effort has been spent both on modelling and on characterizing this component configuration, making it the most reliable version of AWG.

The central wavelength of the AWG is 1550 nm. The channel spacing has been designed to be 120 GHz and it determines the coarse tuning between the lasing modes of the two channels. The FSR has been chosen equal to 1200 GHz (9.6 nm). A large FSR is convenient in order to avoid lasing at different orders of the AWG. Only the wavelengths of the order that is closer to the top of the gain curve of the SOA should experience enough gain to achieve lasing.

The others input parameters required by the Cobra-TUe AWG library are:

- the polarization: TE, in our case;
- the width of the input/output waveguides: $w_{io} = 2 \mu\text{m}$, standard shallow waveguide width in Cobra technology;
- the width of the array waveguides: $w_a = 1.5 \mu\text{m}$, standard deep waveguide width in Cobra technology;

- the center-to-center distance between the input/output waveguides: $d_r = 5 \mu\text{m}$;
- the width of the openings between the array waveguides at the edge of the FPR: $gap_a = 0.8 \mu\text{m}$ (as presented in section 2.3.5);
- the Array Acceptance Factor (AAF) which determines the opening angle of the array of waveguides: $AAF = 2.7$ [2, 3].

Furthermore, no chirp and no Rowland distribution have been selected for the AWG [4]. The other characteristics of the AWG, e.g., size and number of waveguides in the array, are determined by the software based on the given input parameter values.

The AWG design selected is a compromise between the available space and the requirements on its optical performance. In particular the AAF, the d_r , and the Free Spectral Range (FSR) of the AWG are chosen as large as the available space allows.

The larger the d_r (the spacing between two channel input/output waveguides) and keeping the channel spacing requirement constant, the smaller the FWHM of the AWG channel becomes. This occurs since the displacement of the light beam as a function of wavelength at the output plane needs to increase to cover the larger d_r . A small FWHM is desirable in order to reduce the crosstalk between two adjacent channels. Moreover, with a larger d_r , the suppression at a distance of one laser cavity mode spacing from the center of the AWG channel becomes higher and this in turn results in a larger SMSR. For the ring laser presented here, d_r has been chosen equal to $5 \mu\text{m}$. As shown in Fig. 4.3, an analytical model of the AWG predicts a channel width FWHM of 30 GHz [5].

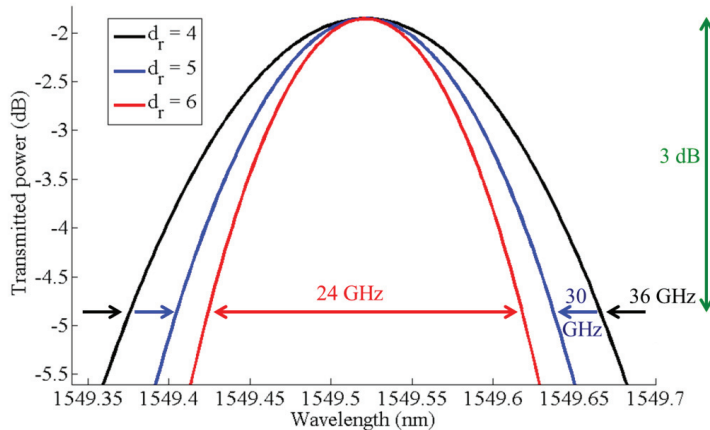


Fig. 4.3. Simulation of the transmitted power through one AWG channel for different values of d_r (center-to-center distance between the input/output waveguides) while all the other input parameters are kept fix at the values indicated above in the text. The blue line presents a FWHM bandwidth of 30 GHz and it corresponds to the case with $d_r = 5$ which is the value used for the actual design of the AWG in the ring lasers.

The AAF determines the opening angle of the array of waveguides. The larger the AAF, keeping other parameters fixed, the lower the ground floor of the crosstalk and the lower the insertion loss. The AWG of the ring laser has an AAF equal to 2.7 which results in a 99% illumination of light onto the waveguide array and a theoretical minimum crosstalk value of -33 dB

from the top of the channel as shown in Fig. 4.4. Such a cross-talk value is however well below a typical experimental cross-talk value minimum of -20 dB.

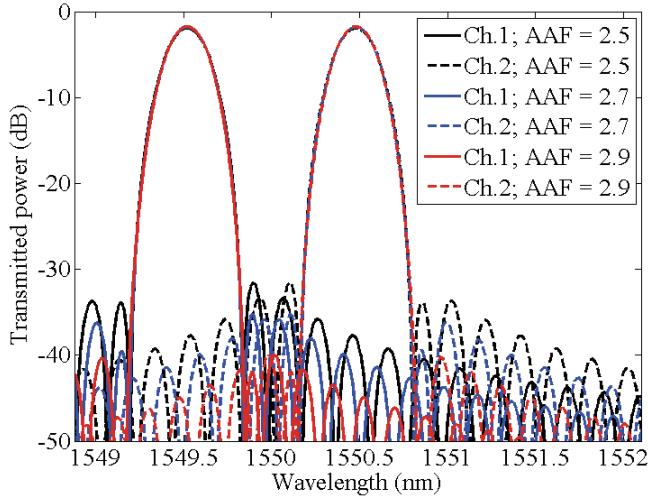


Fig. 4.4. Transmission spectrum of the two channels of the AWG for different values of AAF. The blue lines correspond to AAF = 2.7 which is the value used for the actual design of the AWG in the ring lasers.

With these values of d_r and AAF, an attenuation of 0.3 dB at 5.5 GHz distance from the center of the channel (equal to the mode spacing) is predicted. Laser simulations show that such a channel width provides sufficient suppression of the longitudinal side modes of the cavity: only small loss differences (~ 0.1 dB) are needed for a side mode suppression of 20dB [6].

The selected AWG design based on the input parameter values discussed above is 1500 μm long and 450 μm wide. E.g. an increase of the AAF from 2.7 to 3 while keeping the other parameters fixed would result in a 1700 μm long AWG.

The SOA of the ring laser is 2 mm long. The waveguide enters the active region with a 14° angle with the normal of the active-passive transition in order to minimize the reflections at the active-passive interfaces. The weak point of the butt-joint technique is the difficulty to control the quality of the interface between the active and the passive region. Problems with the quality of the active-passive interface lead to undesired optical reflections in the waveguides at the interface. However, the problem can be solved by using appropriate angles between the waveguide and the active-passive interface [3].

In order to create the MZIs, 2x2 MMIs have been used instead of 1x2 and 2x1 MMIs. The reason is that for the MMI designs used, the 2x2 MMIs give rise to approximately 20 dB lower back-reflection for the two ports on one side of the MMI compared to 2x1 MMIs [7, 8]. Furthermore, as it can be seen in Fig. 3.12, the use of 2x2 MMIs results in a larger number of output waveguides that make the characterization of the device easier. This is e.g. used to get the results in section 4.4.3 where two of these spare outputs are used to characterize the MZIs. As the primary output (and differently than the secondary output), the spare output waveguides reach the facet of

the chip with a taper from $2\ \mu\text{m}$ to $3.5\ \mu\text{m}$ combined with a 7-degree angle of the waveguide with the normal of the facet in order to reduce back-reflections in to the cavity.

Two of these spare outputs from the 2×2 MMIs cannot be used as output waveguides since they are inside the ring cavity. For this reason, two long deep spirals have been designed in order to get rid of the light coupled to these output of the 2×2 MMIs.

The length of the PHMs (3 mm) has been chosen as a compromise between the space available on the chip, the efficiency of the PHM and the accuracy required on the control voltage applied. For the selected orientation, around $1550\ \text{nm}$ a 2π shift should be achieved with a reverse bias of 6 V (single pass). This means that inside the cavity, considering a mode spacing of 5.5 GHz, a noise level of $10\ \mu\text{V}$ in the control voltage applied will lead to a fluctuation in the order of 16 kHz of the lasing modes.

A 2×2 MMI is used to couple the light out of the ring cavity. The primary output is connected to a MZM that can be used for data modulation of the output signal. For this MZM, 2×1 MMIs have been used instead of 2×2 MMIs because of lack of space: a 2×1 MMI is $45\ \mu\text{m}$ long whereas a 2×2 MMI is $330\ \mu\text{m}$ long. The primary output reaches the facet of the chip through a mode filter and a taper from $2\ \mu\text{m}$ to $3.5\ \mu\text{m}$ combined with a 7-degree angle of the waveguide with the normal of the facet in order to reduce back-reflections to the laser cavity. The other output of the output coupler is connected through a straight waveguide to the facet (secondary output) in order to provide a considerable feedback inside the cavity and force the laser to work in clockwise direction.

Two passive waveguides are used to connect the higher order of the AWG to the monitoring PDs. The PDs are meant to be used to check the power of the lasing modes in Channel 1 and Channel 2. Fig. 4.5a shows in detail the design of the PDs.

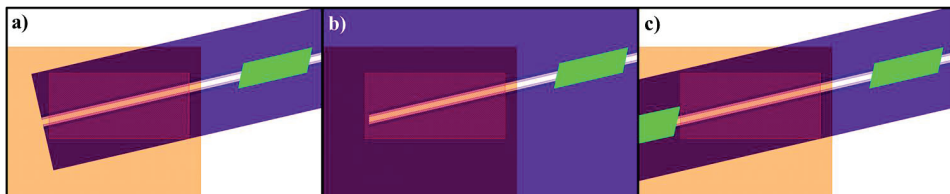


Fig. 4.5. Color code: ■ indicates a trench area: a waveguide is surrounded by two trenches; ■ indicates an area where the waveguide is in the isolation section configuration; ■ is the color the metal pad; the red-recticulated rectangle indicates the active region on the wafer. For sake of clarity, the layers corresponding to the masks of the polyimide and the silica have been removed from the picture. The metal pad is in contact with the waveguide only inside the active region. a) Layout of a PD for the device discussed in this chapter (design with trenches). The isolation section is present only at one end of the waveguide: the PD is not electrically isolated from the rest of the chip. b) Design of a PD for a circuit without trenches: the second isolation section is not needed. c) Correct layout of a PD for a circuit designed with trenches: isolation sections are placed at both ends of the PD.

As in the SOA, the shallow waveguides goes through an isolation section and then enters the active region with a 14° angle with the normal of the active-passive transition. The isolation sections are present at both ends of the SOAs and the PHMs in order to electrically isolate these components from each other. In the designed and realized circuits the PDs could not be used independently for monitoring since isolation sections were only put in the design at one end of the waveguide in the PD structure. This problem originates from a previous design that was produced for a fabrication in

which the waveguides were not in trenches. When there are no trenches, the waveguide of the PDs would be etched at the end as shown in Fig. 4.5b: then, there is no need of isolation section. When the waveguide are in trenches, a second isolation section is required in the design to electrically isolate each PD from the rest of the chip. Fig. 4.5c shows a correct design of the PD for a fabrication process with trenches. The color code used in Fig. 4.5 is explained in the caption.

4.3 Components characterization

In this section the performance of the SOA, the AWG and the MZIs inside the cavity is discussed. This basic characterization is needed to be able to interpret the behavior of the laser.

4.3.1 SOA characterization

The main parameter for the SOA in the laser is the small-signal gain spectrum. Several methods can be used to determine the optical gain of an SOA. The most common ones are the Hakki-Paoli technique [9], the Henry technique [10, 11] and the analysis of the amplified spontaneous emission (ASE) as a function of the length of the amplifier [12]. All these methods have advantages and drawbacks. In the first two techniques, only current densities below the threshold of the device can be applied. Furthermore, the Hakki–Paoli method requires high spectral resolution to resolve the longitudinal modes and the Henry technique calculates the Fermi-level energy separation indirectly and does not immediately provide gain in absolute units. Some of the methods based on the analysis of the ASE use SOAs with different lengths, but these techniques require constant collection efficiency in order to be reliable.

For the measurements of the optical gain, we use a method based on a multisection device [13]. With this technique, current densities larger than the threshold can be applied. Moreover, the method provides values of gain in absolute units. The relation between the net modal gain $G(\lambda)$ and the power $P(\lambda)$ of the ASE at wavelength λ from an SOA of length L can be described as:

$$P(\lambda) = \frac{P_{sp}(\lambda)}{G(\lambda)} (e^{G(\lambda)L} - 1) \quad (4.1)$$

where $P_{sp}(\lambda)$ is the power of the spontaneous emission (per unit length) Using the ASE power spectra for two different SOA lengths L and $2L$, we can obtain an analytical expression for the net modal gain:

$$G(\lambda) = \frac{1}{L} \ln \left(\frac{P_{2L}(\lambda)}{P_L(\lambda)} - 1 \right) \quad (4.2)$$

where $P_{2L}(\lambda)$ and $P_L(\lambda)$ are the ASE power values of a section with a length of $2L$ and L respectively. This methods, then, derives the modal gain spectra $G(\lambda)$ in absolute units from the recorded ASE power.

The SOA test structure used for the gain measurements is shown in Fig. 4.6. Five different multisection devices are present, with different SOA section lengths. For each multisection device,

we measured the ASE power and spectrum on the right hand side of the chip, while forward biasing the first section on the right, then the first and the second sections at the same time, and so on. The validity of the results depends upon the measurement of a single pass of the spontaneous emission light. For this reason all the sections that are not forward biased are reversely biased in order to absorb the ASE generated that propagates to the left and to avoid reflection from the facet.

A 25 μm long isolation section is placed between the SOAs in order to provide electrical isolation between the gain sections.

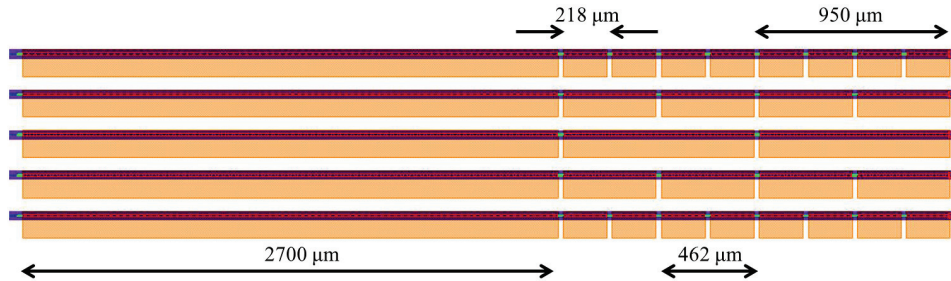


Fig. 4.6: Design of the multisection SOA test structure used for the determination of the optical gain. Sections from 218 μm to 950 μm are present on the chip. For each multisection device, we measured the ASE while forward biasing the first section (from the right end side of the chip), the first and the second sections at the same time, and so on. The 2.7 mm long section is reversed bias in order to maximize the absorption and avoid back reflections from the facet of the chip.

The SOA gain spectra depicted in Fig. 4.7 have been determined by measuring the ASE of the 950 μm SOA sections for different injection currents. The temperature of the device was kept to 15 $^{\circ}\text{C}$ using a water cooling system and a Peltier element. The single-pass ASE has been collected with a lensed fiber and the spectra have been recorded with a 0.5 nm resolution spectrometer over a 60 nm span in 1000 data points.

In order to verify that the feedback from the absorber is negligible, also the light from the absorber side output has been collected. The worst case recorded is the one with both 950 μm long sections biased at 7 kA/cm^2 . In this scenario, the output power level at the absorber side is 30 dB lower than the one at the multisection SOA side. Considering the gain of the SOA sections (see Fig. 4.7) and the reflectivity of the facet (reflectivity = 0.3), these power levels indicate that far less than 10^{-6} of the power is back reflected into the forward biased SOA sections.

In Fig. 4.7 the modal gain spectra for different injection current densities is presented. For the calculation of the current densities a waveguide ridge width of 2 μm was used. The wobbles in the spectra are attributed to reflections on the isolation sections in the waveguide which modulate the recorded spectra. The levels of current injection used for the gain measurements are higher than the threshold current density levels of the actual ring laser.

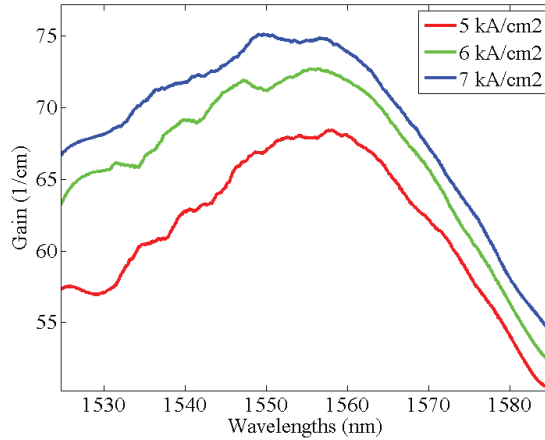


Fig. 4.7: Modal gain spectra for different injection current densities. Gain values higher than 70 cm^{-1} are obtained for injection carrier density equal to 6 kA/cm^2 . These values of gain are in line with what is expected in our technology.

Gain values higher than 70 per cm are obtained for an injection carrier density of 6 kA/cm^2 and over. These values of gain are in line with what is expected in our technology. No significant change in the shape of the gain spectrum has been observed over a range of $10 \text{ }^\circ\text{C}$ at constant current density of 6 kA/cm^2 . A shift in the wavelength of the highest gain of $1 \text{ nm per } ^\circ\text{C}$ was observed.

The gain spectra show that an FSR of the AWG of 9.6 nm is sufficient to obtain lasing in a single order of the AWG (see Fig. 4.8b): 10 nm away from the peak of the gain spectrum, the gain in a 2 mm long SOA is approximately 1.5 to 2.5 dB lower. This is more than sufficient to prevent lasing in the neighboring orders.

The total passive loss in the cavity of the ring laser is estimated to be around 23 dB : 5 dB AWG insertion loss, 3 dB MMI output coupler plus 1 dB insertion loss, 1 dB insertion loss for each splitter/combiner, 4 dB from the PHMs in the MZIs and 5 dB due to the total passive waveguide length.

4.3.2 AWG characterization

The AWG is a passive component and a large part is built up from deeply etched waveguides in the array. The loss value of a shallow waveguide is 8 dB/cm and the deeply etched waveguide is 9 dB/cm . These values have been measured in test waveguides on the same chip. This high loss value is attributed to the fact that the realized waveguides are narrower than what has been designed: $1.8 \text{ }\mu\text{m}$ instead of $2 \text{ }\mu\text{m}$ for the shallow waveguides and $1.3 \text{ }\mu\text{m}$ instead of $1.5 \text{ }\mu\text{m}$ for the deep waveguides. Another possibility is that the p-doping levels of the different layers of the wafer is higher than designed. These doping levels have a strong impact on the optical loss, but these aspects have not been investigated.

A test-AWG identical to the one of the actual device is present among the test structures. Fig. 4.8a shows a measurement of the transmission spectrum through a 4-channel AWG in the

wavelength range of the order nearest the gain peak of the SOA. Fig. 4.8b combines the gain curve at 7 kA/cm^2 with the transmission spectrum of the different orders of the AWG.

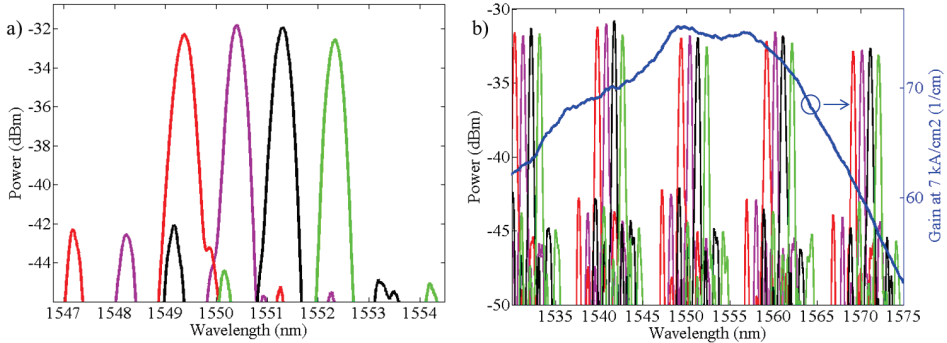


Fig. 4.8. a) Power transmitted through one order of a test 4-channel AWG. Each color corresponds to a different channel. b) Gain curve at 7 kA/cm^2 together with the power transmitted through different orders of the same AWG. An FSR of the AWG of 9.6 nm is sufficient to obtain lasing in a single order of the AWG

The measured channel spacing of the AWG is 121 GHz which nicely matches the designed value (120 GHz). The FWHM of the channels is 45 GHz and this is larger than designed value (35 GHz). However, the suppression at 5.6 GHz from the center of the channel (equal to the expected mode spacing) is 0.25 dB which should be sufficient to have a SMSR better than 25 dB . Also the FSR of the AWG corresponds to the designed value (1200 GHz).

The central wavelength of the channels connected to the higher order outputs matches the central wavelength of the corresponding channels at order 0. This is promising for the possibility to use the signal collected by the PDs connected to the higher order of the AWG to estimate the power in the two lasing wavelength. Unfortunately, as explained in section 3.4.3, in the ring laser, the monitoring PDs could be used since they are not electrically isolated.

4.3.3 MZIs and PHMs characterization

In order to be able to control the device, a precise characterization of the MZIs is needed. This could be done in the actual ring laser itself. As discussed in section 4.2, several spare input/output waveguides have been placed in the design in order to facilitate the characterization of the ring laser. In particular, the i/o waveguide indicated by the dashed lines in Fig. 4.9 can be used to characterize separately MZI1 using an external laser source.

The laser device was mounted using the system described in section 2.4 and kept at a constant temperature of $15 \text{ }^\circ\text{C}$. The transmission of MZI1 as a function of the voltage applied to PHM1A is presented in Fig. 4.10a. This direct characterization shows a value of $V\pi$ equal to 6 V (at 1550 nm) and an extinction ratio of 15 dB . Identical extinction ratio and $V\pi = 6.2 \text{ V}$ was found while scanning the voltage on PHM1B. This direct characterization of part of the device is convenient.

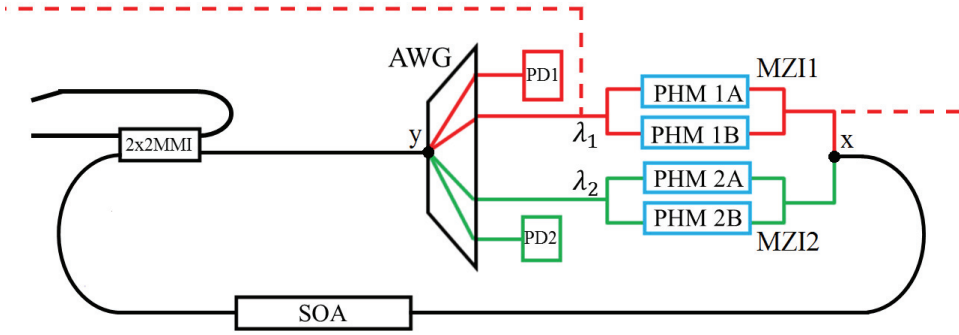


Fig. 4.9: Schematic of the ring dual-wavelength laser. The dashed lines indicate the i/o waveguide that can be used to characterize separately MZI1 using an external laser source.

However, MZI2 must be characterized indirectly since it is placed in the inner part of the ring and, consequently, there are no i/o waveguides that can access MZI2 directly. Thus, we have elaborated an indirect characterization technique. First, MZI1 is set to destructive interference configuration forcing the device to lase through Channel 2. Then, the values of the threshold current (I_{th}) of the laser are determined as a function of the voltage applied to the PHMs of Channel 2. The value of the threshold current changes due to the changes of the losses in the cavity. As a result, the transmission function of MZI2 can be extracted. Fig. 4.10b shows the value of I_{th} while scanning the voltage of PHM2A. When both channels are set to maximum extinction, lasing action takes place through Channel 2. This suggests that the extinction ratio is lower in MZI2 than in MZI1 however. The graph in Fig. 4.10b shows a value of $V\pi$ equal to 6.4 V, consistent with the ones measured directly on MZI1. The measurements on MZI1 and MZI2 thus provide the voltage settings for fully opening and closing the MZI's.

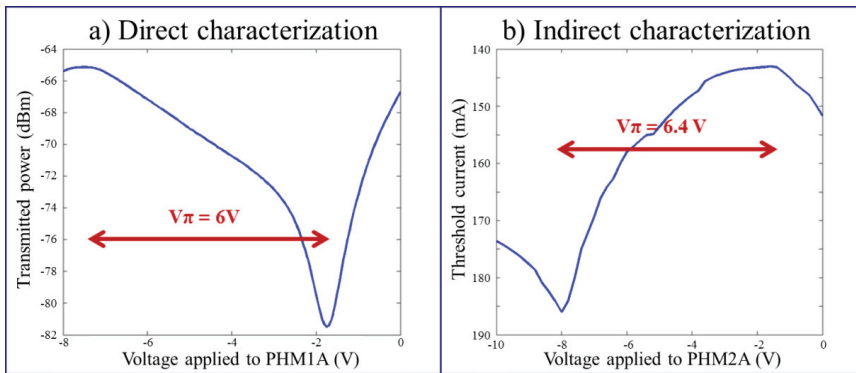


Fig. 4.10. a) Direct characterization of PHM1A. b) Indirect characterization of PHM2A, based on current threshold changes.

4.4 Basic characterization of the ring laser

As mentioned in section 3.2, the added benefit of a ring laser is an increased SMSR. If the laser operates in unidirectional way, spatial-hole-burning is avoided since there is no standing wave inside the laser cavity. This results in a better stability for single mode operation of the laser.

Fig. 4.11 compares the output power collected from the primary output and the secondary output. After reaching the threshold current ($I_{th} = 153$ mA), $P_{clockwise}$ (the power collected from the primary output) is two orders of magnitude higher than $P_{anti-clockwise}$ (the power collected from the secondary output) demonstrating the unidirectional operation of the ring laser.

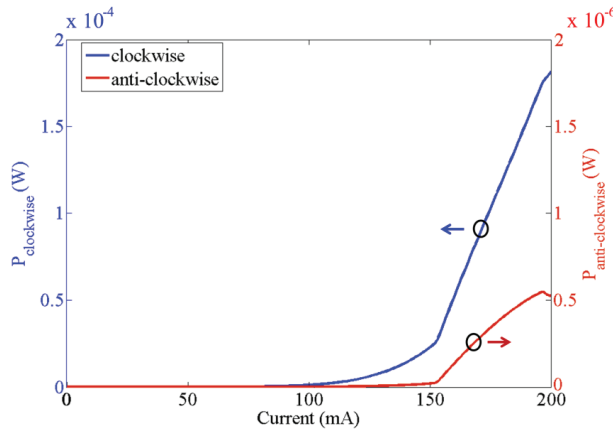


Fig. 4.11. LI curves recorded from primary and the secondary output of the ring laser. After reaching the threshold current ($I_{th} = 153$ mA), $P_{clockwise}$ (the power collected from the primary output) is two orders of magnitude higher than $P_{anti-clockwise}$ (the power collected from the secondary output) demonstrating the unidirectional operation of the ring laser.

The LI curves presented in Fig. 4.11 have been recorded while all the PHMs of the devices were grounded ($V = 0$ V). As a consequence the competition between the two modes in the SOA results in one longitudinal mode lasing, suppressing the mode of the other channel. Fig. 3.22 shows an optical spectrum from the primary output recorded using an APEX Technologies AP2041 spectrometer with 20 MHz resolution. The SOA was biased at 170 mA and the voltage on the PHMs was at 0 V. As expected since there is no balancing of the loss in the two channels, most of the power is at λ_2 whereas λ_1 is suppressed. The mode spacing matches the designed value of 5.5 GHz (15 mm long ring cavity). Furthermore a SMSR larger than 41 dB is demonstrated.

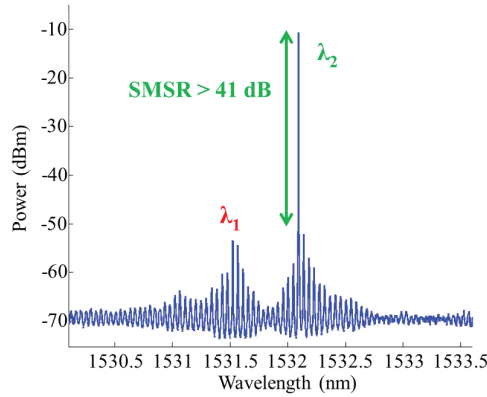


Fig. 4.12. Single mode operation of the ring laser. Optical spectrum from the primary output obtained while biasing the SOA at 170 mA and keeping the voltage on the PHMs at 0 V. The spectrum has been recorded using an APEX Technologies AP2041 spectrometer with 20 MHz resolution. As expected, most of the power is at λ_2 whereas λ_1 is suppressed. The mode spacing matches the designed value of 5.5 GHz (15 mm long ring cavity). Furthermore a SMSR larger than 41 dB is demonstrated.

It is important to notice that although the peak of the gain curves shown in Fig. 4.7 is around 1550 nm, the device tends to lase at shorter wavelength. This might be due to the fact that the losses in the MMIs and in the waveguides are wavelength dependent. The MMIs (as the waveguides) are thinner than expected and this could make the losses at shorter wavelength lower than the losses at 1550 nm. In addition, also the losses of the order of the AWG around 1530 nm appear to be lower than those at 1550 nm (Fig. 4.8b).

As shown in Fig 4.9, a 2x2 MMI is used to couple the light out of the ring cavity. The primary output is connected to a MZM for data modulation of the output signal. For this MZM, 2x1 MMIs have been used instead of 2x2 MMIs because of lack of space on the chip: a 2x1 MMI is 45 μm long whereas a 2x2 MMI is 330 μm long. The primary output, then, reaches the facet of the chip through a mode filter and a taper from 2 μm to 3.5 μm combined with a 7-degree angle of the waveguide with the normal of the facet in order to reduce back-reflections to the laser cavity. Fig. 4.13 shows the power from the primary output as a function of the voltage applied to one of the PHMs of the output MZM (PHM0B) while biasing the SOA at 180 mA. The value of $V\pi$ is around 6.3 V and the constructive interference is obtained when -0.3 V is applied to PHM0B. If not specified, all the measurements presented in this section have been performed while keeping the voltage applied to PHM0B to this value in order to maximize the output power from the primary output.

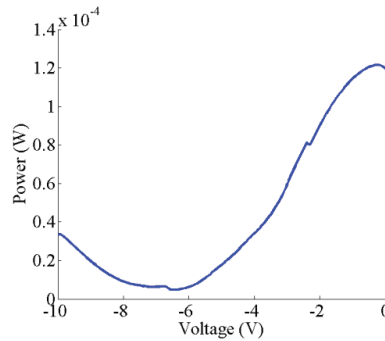


Fig. 4.13. Power from the primary output as a function of the voltage applied to one of the PHMs of the output MZM (PHM0B) while biasing the SOA at 180 mA. The value of $V\pi$ is around 6.3 V and the constructive interference is obtained when -0.3 V are applied to PHM0B. When the voltage reaches the values of the two jumps in the figure ($V = -2.3$ V and $V = -6.6$ V), the device changes the order of the AWG through which it is lasing. At $V = -2.3$ V the device stops lasing at 1532.1 nm and operates in single mode at 1522.9 nm. At $V = -6.6$ V, the device starts operating once again at 1532.1 nm.

It is important to notice that two unexpected jumps are present in the curve of Fig. 4.13. Analyzing the output spectra from the primary output while scanning the voltage of PHM0B under the same conditions used for Fig. 4.13, we noticed that the changes in the applied voltage had a severe impact on the spectrum of the device. In particular, when the voltage reaches the values of the two jumps in Fig. 4.13 ($V = -2.3$ V and $V = -6.6$ V), the device changes the order of the AWG through which it is lasing. At $V = -2.3$ V the device stops lasing at 1532.1 nm and operates in single mode at 1522.9 nm. At $V = -6.6$ V, the device starts operating once again at 1532.1 nm. The impact that the voltage applied to PHM0B has on the output spectrum of the device reveals that there is a reflection inside the primary output arm and the light reflected back in the laser cavity impacts the functioning of the device. This reflection can be caused by the second 2×1 MMI or by the facet [1]. A mode filter and a taper from $2 \mu\text{m}$ to $3.5 \mu\text{m}$ combined with a 7-degree angle of the waveguide with the normal of the facet have been applied in the design. For these conditions a minimum is predicted in the fundamental mode reflection, depicted in Fig. 4.14 which reports the simulations obtained using the Mirf/Femsc software [14]. However, the reflectivity is very sensitive to the width of the waveguide. Since in the ring laser the waveguides are $0.2 \mu\text{m}$ narrower than expected (see section 2.3.5), the mode filter cannot perform as expected and the reflections from the facet are larger than what is desired. Unfortunately, as a result, the output MZM cannot be used because the changes in the reflections dramatically affect the behavior of the device. Also because of the back reflection the laser can behave rather erratically and any systematic and automatic control system to obtain and hold dual-wavelength operation on this device becomes unpractical.

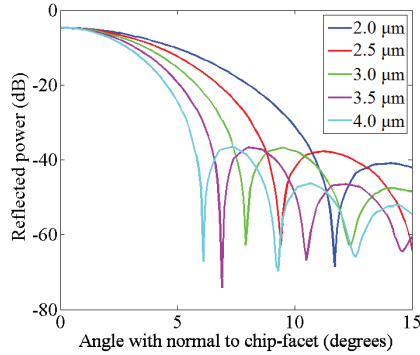


Fig. 4.14. Fundamental mode reflection for different waveguide widths as a function of the angle with normal to chip-facet.

From the technological point of view, this strong dependency of the reflectivity on the width of the output indicates that tilting the output waveguides 7° with respect to the chip facets is not always sufficient to suppress back reflections, making AR coatings a requirement [1].

4.4.1 Dual-wavelength operation and analysis below threshold

As explained in Chapter 3, accurate control of the losses is required in order to obtain a dual-wavelength behavior: the losses in the cavity for λ_1 and λ_2 must be equalized. Although a systematic automatic control is not possible because of the back reflections from the facet, by manually adjusting the voltage settings applied to the PHMs of the MZI, we have been able to achieve dual-wavelength operation, as depicted in Fig. 4.15.

The frequency difference between the two main longitudinal modes is much smaller than expected: 81.3 GHz (Fig. 4.15a), 92.8 GHz (Fig. 4.15b) and 88.7 GHz (Fig. 4.15c). The channel spacing of the AWG is 120 GHz. Moreover, a difference of 3 – 4 dB between the two lasing modes is still present in each of the presented cases.

Although further investigations are required in order to fully understand the functioning of the laser, the graphs in Fig. 4.15 demonstrate that, balancing the losses in the two channel of the device, dual-wavelength operation through one common SOA can be achieved.

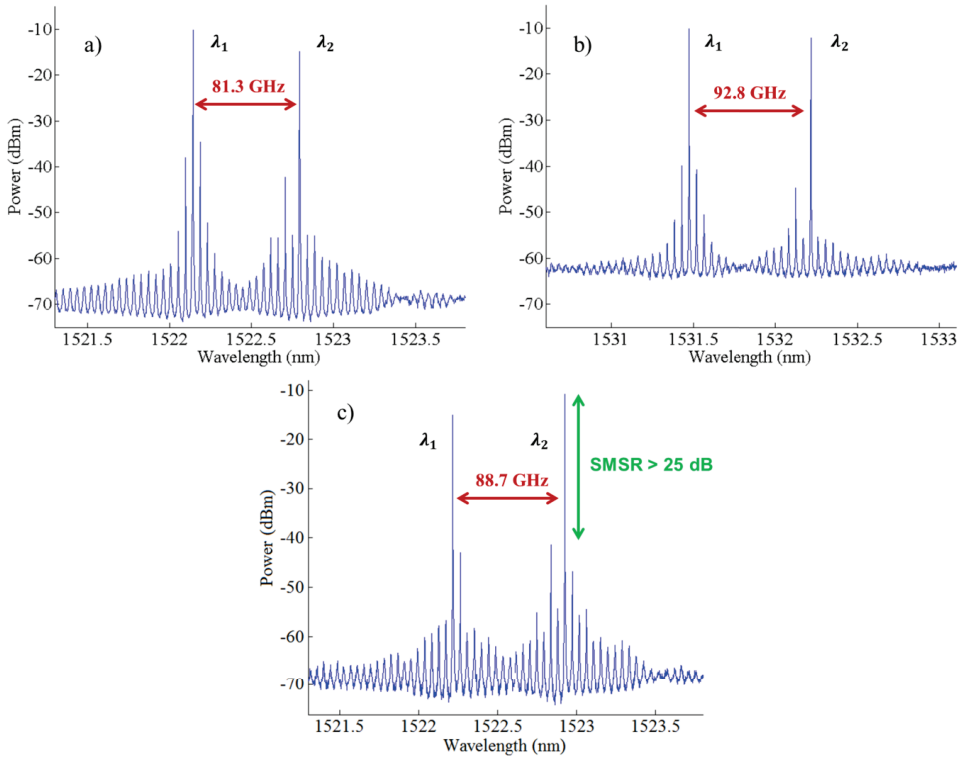


Fig. 4.15. Dual mode operation of the ring laser. a) The current injected in the SOA (I_{SOA}) is 160 mA; the voltages applied to the PHMs are $V_{1A} = -0.8$ V, $V_{2A} = -3.5$ V, $V_{1B} = -2.25$ V, $V_{2B} = -4$ V. The frequency distance between the two lasing mode is 81.3 GHz. b) $I_{SOA} = 150$ mA, $V_{1A} = 0$ V, $V_{2A} = -3$ V, $V_{1B} = -5.4$ V, $V_{2B} = -1$ V; frequency difference = 92.8 GHz. c) $I_{SOA} = 148$ mA, $V_{1A} = -3$ V, $V_{2A} = -4.75$ V, $V_{1B} = -5$ V, $V_{2B} = -5.65$ V; frequency difference = 88.7 GHz; SMSR > 25 dB. A difference of 3 - 4 dB is present between λ_1 and λ_2 in each of the presented cases. The frequency difference between the two longitudinal modes is much smaller than expected: the channel spacing of the AWG is 120 GHz.

The more convenient way to study the functioning of the laser is an analysis of its spectrum below threshold. The output spectrum of the device below threshold shows the mode structure of the cavity much more clearly and the effects of small reflections in and outside the cavity are reduced. Fig. 3.26 shows the output spectra from the primary input while the SOA is biased at 120 mA. The value of current has been chosen close to threshold because lower values did not lead to sufficient output power. The spectrum reported in Fig. 4.16a has been recorded while the MZIs of Channel 1 and Channel 2 were set to the maximum transmission ($V_{PHM1A} = 0$ V, $V_{PHM1B} = -1.8$ V, $V_{PHM2A} = -1.75$ V, $V_{PHM2B} = 0$ V). The frequency difference between the peaks of Channel 1 and Channel 2 is 80.7 GHz, significantly lower than the channel spacing of the AWG. Sweeping the voltage applied to PHM2A and PHM2B simultaneously in order to obtain tuning of the mode fringes results in the appearance of a third lobe between Channel 1 and Channel 2 as depicted in Fig. 3.25b. The voltage settings corresponding to this spectrum are ($V_{PHM1A} = 0$ V, $V_{PHM1B} = -1.8$ V, $V_{PHM2A} = -4.75$ V, $V_{PHM2B} = -3$ V) and the frequency difference between Channel 1 and Channel 2 is

124.8 GHz. As discussed more in detail through the model presented in section 4.5, the presence of the central lobe is caused by the crosstalk between the two channels of the AWG and by the phase in the transmission function of each channel of the AWG. A first clear indication that the central lobe is related to the crosstalk between Channel 1 and Channel 2 can be seen in the subthreshold spectra. Starting from the case of Fig. 4.16 the Channel 1 MZI setting is changed to a high loss configuration. In the resulting spectrum (Fig. 3.25c) both the lobe of Channel 1 and the central lobe are suppressed. Similarly when the MZI in Channel 2 is set to a high loss configuration, both the lobe of Channel 2 and the central lobe are suppressed.

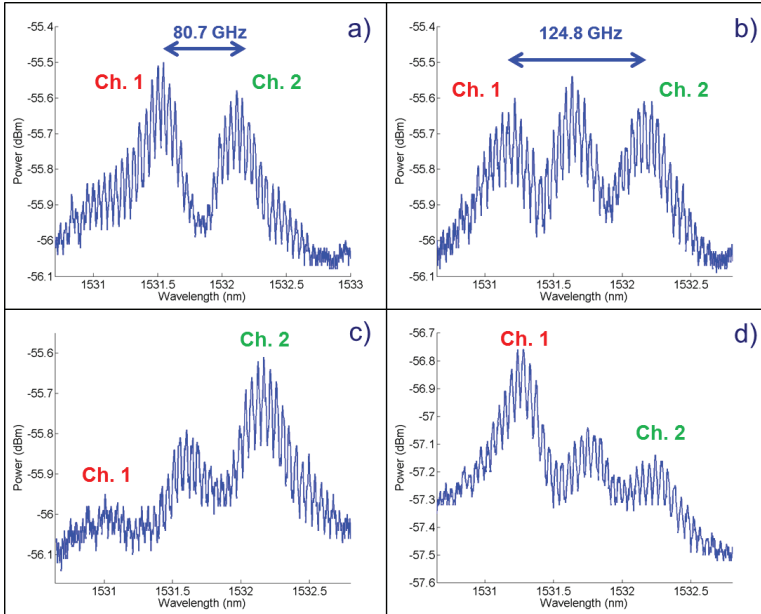


Fig. 4.16. Output spectra of ring laser (primary output) below the lasing threshold. The SOA current is 120 mA. a) The MZIs in Channel 1 and Channel 2 are set to maximum constructive interference configuration. The frequency difference between the two channels is 80.7 GHz, significantly smaller than the channel spacing of the AWG. b) Sweeping simultaneously the voltage applied to both PHMs of Channel 2 leads to the appearance of a third central lobe in the spectrum due to AWG crosstalk between Channel 1 and Channel 2. The frequency difference between the lobes of the two channels is in this case 124.8 GHz. As a proof of the fact that the central lobe is caused by AWG crosstalk, c) Setting the MZI in Channel 1 to destructive interference configuration, both the lobe of Channel 1 and the central lobe are suppressed. Similarly, d) Setting Channel 2 to destructive interference configuration, both the lobe of Channel 2 and the central lobe are suppressed.

4.5 Ring laser analysis

An analytical steady state laser model has been implemented and used to study and explain the observed behavior of the ring laser. The model includes effects of the cross-talk between the two channels in the AWG. In this model each component of the laser has been described by a linear model using the T-matrix formalism [15]. This formalism is mathematically identical to the S-matrix one. The advantage of the T-matrix formalism, however, is that the total T-matrix of two components in series is simply the product of the T-matrices of the individual components. It is then easy to calculate the T-matrix of a single roundtrip and to apply the boundary condition of a ring cavity on it. This is depicted in Fig. 4.17(a). The components in the ring are the filter (comprised of the two AWG channels and MZIs with phase modulators), the SOA, the passive waveguide in the laser and the 2x2 MMI output coupler. The component T-matrices can be combined into a single T_{Ring} -matrix. Then, as depicted schematically in Fig. 4.17(b), the ring cavity condition can be applied and the electric fields can be solved as a function of wavelength, given information on gain, losses, ASE strength, etc.

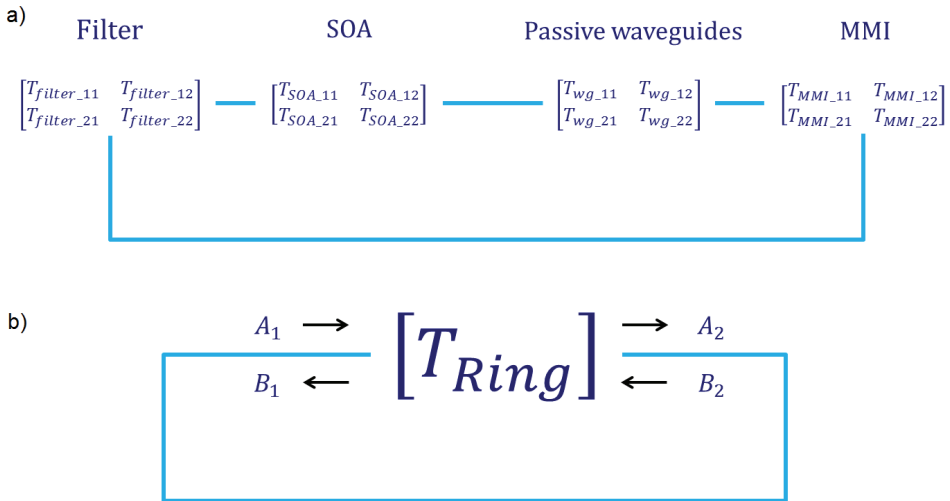


Fig. 4.17: a) A schematic depiction of the T matrices describing the components transmission and reflection for a single pass through the ring cavity of the laser. b) The combined T-matrices form a single T_{Ring} -matrix on which the ring cavity boundary conditions are applied.

The T-matrix of a single pass through the system relates the field amplitudes on side 1 to the field amplitudes on side 2:

$$\begin{bmatrix} A_1 \\ B_1 \end{bmatrix} = \begin{bmatrix} T_{Ring_11} & T_{Ring_12} \\ T_{Ring_21} & T_{Ring_22} \end{bmatrix} \begin{bmatrix} A_2 \\ B_2 \end{bmatrix} \quad (4.3)$$

where A_1 , A_2 , B_1 , B_2 represent the electrical field amplitudes as depicted in Fig. 4.17(b). In the description of the components in the model, no coupling between the clockwise and the anti-

clockwise direction of the ring is taken into account: T_{Ring_21} and T_{Ring_12} are therefore equal to zero. As a consequence, the equation (4.3) becomes a set of two simple equations:

$$\begin{aligned} A_1 &= T_{Ring_{11}} A_2 \\ B_1 &= T_{Ring_{22}} B_2 \end{aligned} \quad (4.4).$$

Essentially, we do not need to consider full T-matrices under such a condition. However for generality we will stick to that description so that further extensions to the model with reflections inside the cavity can be easily made.

The equations (4.4) do not have any ASE included. One solution is to include the ASE as done in section 3.3. Here a slightly different way is used. The average amplified spontaneous emission electric field strength E_{ASE} is added to the laser mode electric field every roundtrip. Adding the ASE and closing the ring gives two further equations to form a system that can be solved:

$$\begin{aligned} A_1 &= T_{Ring_11} A_2 \\ B_1 &= T_{Ring_22} B_2 \\ A_1 &= A_2 + E_{ASE} \\ B_2 &= B_1 + E_{ASE} \end{aligned} \quad (4.5).$$

The solutions of the electric field amplitudes then become:

$$\begin{aligned} A_1 &= \frac{E_{ASE} T_{Ring_11}}{T_{Ring_11} - 1} \\ A_2 &= \frac{E_{ASE}}{T_{Ring_11} - 1} \\ B_1 &= -\frac{E_{ASE} T_{Ring_22}}{T_{Ring_22} - 1} \\ B_2 &= -\frac{E_{ASE}}{T_{Ring_22} - 1} \end{aligned} \quad (4.6).$$

For the T-matrix of the ring and for the T-matrix of each component, given T_{11} , then

$$T_{22} = \frac{1}{T_{11}} \quad (4.7).$$

In the following, the modelling of each component is described in detail starting with the AWG and the MZI filters.

In Fig. 4.18a, the experimental AWG channel transmission is reported. As it can be noticed in Fig. 4.18b, such a shape for the absolute value of the linear transmission of channel n ($n = 1, 2$) of the AWG can be reasonably accurately modelled with:

$$T_{AWG,n}(\lambda) = \left[\frac{\sin\left(\frac{\lambda - \lambda_n}{\xi\sqrt{2}}\right)}{\left(\frac{\lambda - \lambda_n}{\xi\sqrt{2}}\right)} \right] \quad (4.8)$$

where $\xi = 1.2 \cdot 10^{-10}$ m and λ_n is the center wavelength of the channel at $\lambda_1 = 1550.5$ nm or $\lambda_2 = 1551$.

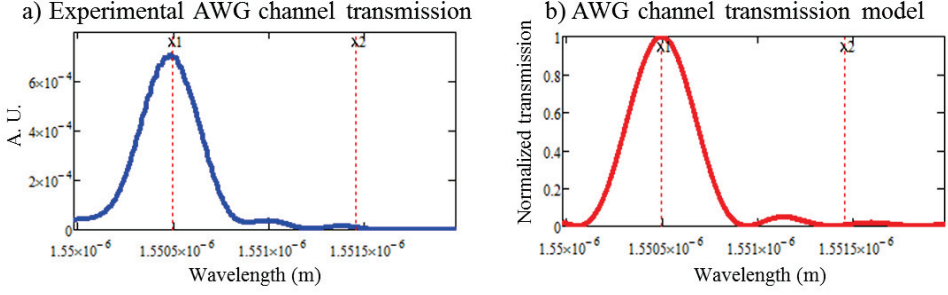


Fig. 4.18: a) Experimental AWG channel transmission; b) AWG channel transmission model.

Equation (4.8) presents a simplified model of the transmission of one channel of the AWG, but it is convenient and effective in the case presented here. As a consequence, we use it to describe the absolute value of the transmission from each individual channel to the common channel of the AWG. Note that in equation (4.8) there is no effect on the phase of the electric field.

For the PHMs in the MZI, a simple linear relation between the change in the phase of the transmitted electric field (Φ_{phm}) and the voltage applied to the PHM (V) is used:

$$\Phi_{phm}(V, \lambda) = \frac{dn_g}{dV} V \cdot L_{phm} \cdot 2\pi \quad (4.9)$$

where L_{phm} is the length of the PHM, λ the wavelength of the light and $\frac{dn_g}{dV}$ is the derivative of the group index to the applied voltage. The voltage dependent loss which occurs in the real PHMs is ignored.

Consequently, the electric field at the output of the PHM as a function of the input field E_{in} is described as:

$$E_{phm}(V, \lambda) = E_{in} \cdot e^{i\Phi_{phm}(V, \lambda)} \quad (4.10)$$

The part of the circuit composed of the Mach-Zehnder construction and the AWG (from point x to point y in anti-clockwise direction in Fig. 4.9) is the wavelength filtering part of the device. The transmission of the electric field through this filter (depicted in Fig. 4.19) is modelled with:

$$E_{filter} = E_{in} \cdot \sqrt{0.5} \cdot \sqrt{\frac{1}{4}} \cdot \left\{ T_{AWG,1}(\lambda) \cdot \left(e^{i\Phi_{phm}(V_{1A}, \lambda)} + e^{i\Phi_{phm}(V_{1B}, \lambda)} \right) + T_{AWG,2}(\lambda) \left(e^{i\Phi_{phm}(V_{2A}, \lambda)} + e^{i\Phi_{phm}(V_{2B}, \lambda)} \right) \cdot e^{i \cdot \frac{\Delta L_{ch}}{\lambda_i} \cdot 2\pi} \right\} \quad (4.11)$$

where E_{in} is the electrical field at the input of the filter, V_{1A} , V_{1B} , V_{2A} , and V_{2B} are the voltages applied to PHM1A, PHM1B, PHM2A, and PHM2B respectively.

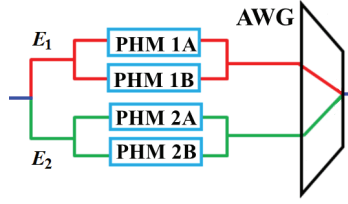


Fig. 4.19: Schematic of the filter composed of the Mach-Zehnder construction and the AWG (from point x to point y in Fig. 3.19). E_1 and E_2 are the electrical fields in Channel 1 and Channel 2 respectively.

Remembering the equation (4.7), the T-matrix for the whole filter is:

$$\bar{T}_{filter} = \begin{bmatrix} T_{filter_11} & 0 \\ 0 & \frac{1}{T_{filter_11}} \end{bmatrix} \quad (4.12).$$

From (4.11) it follows that the element of the T-matrix T_{filter_11} equals:

$$T_{filter_11} = \frac{E_{filter}}{E_{in}} \quad (4.13).$$

The last two components to be modelled are the SOA and the passive waveguides. The model of the SOA requires 4 inputs:

- length of the SOA (L_{SOA});
- wavelength (λ);
- effective group index (n_g);
- total exponential gain coefficient ($g_{SOA} > 0$)

that are used in the following T-matrix:

$$\bar{T}_{SOA} = \begin{bmatrix} e^{i \frac{2\pi n_g L_{SOA}}{\lambda}} \cdot e^{\frac{g_{SOA}}{2}} & 0 \\ 0 & e^{-i \frac{2\pi n_g L_{SOA}}{\lambda}} \cdot e^{-\frac{g_{SOA}}{2}} \end{bmatrix} \quad (4.14).$$

The T-matrix used to model the passive waveguides is similar to the one of the SOA:

$$\bar{T}_{wg} = \begin{bmatrix} e^{i \frac{2\pi n_g L_{wg}}{\lambda}} \cdot e^{-\left(\frac{att_dB}{2} \cdot 0.1 \cdot \ln(10) \cdot L_{wg}\right)} & 0 \\ 0 & e^{-i \frac{2\pi n_g L_{wg}}{\lambda}} \cdot e^{\left(\frac{att_dB}{2} \cdot 0.1 \cdot \ln(10) \cdot L_{wg}\right)} \end{bmatrix} \quad (4.15)$$

where att_dB represents the optical losses per meter in dB.

A 2x2 MMI coupler is used as an output coupler. In this model, MMIs are considered as perfect 3dB splitters (couplers) and the T-matrix of an MMI is taken to be:

$$\bar{T}_{MMI} = \begin{bmatrix} T_{MMI_11} & T_{MMI_12} \\ T_{MMI_21} & T_{MMI_22} \end{bmatrix} = \begin{bmatrix} \sqrt{0.5} & 0 \\ 0 & \frac{1}{\sqrt{0.5}} \end{bmatrix} \quad (4.16).$$

All the optical elements of the ring cavity are described by the T-matrix:

$$\bar{T}_{Ring} = \bar{T}_{filter} \cdot \bar{T}_{SOA} \cdot \bar{T}_{wg} \cdot \bar{T}_{MMI} \quad (4.17).$$

An output spectrum of the laser can now be calculated by setting all the parameters in the model and calculating T_{Ring} for a range of wavelengths. Using the equations (4.6), one can calculate A_2 that is the field strength just after the MMI output coupler. This strength is equal to the field that is coupled out. The setting of the gain of the SOA is important: it should be increased carefully and should not lead to a roundtrip gain of more than one. At the lasing threshold $|T_{filter_11}|^2 = 1$.

The values of the input parameters used in the laser model are listed in Table 4.1

Symbol	Description	Value
λ_c	Lasing wavelength	1550 nm
Δf	Frequency difference between the two modes	120 GHz
λ_1	Lambda of Channel 1	λ_c
λ_2	Lambda of Channel 2	$\frac{c}{\frac{c}{\lambda_1} + \Delta f}$
n_g	Group refractive index	3.7
L_{phm}	Optical length of the PHM	3 mm
L_{SOA}	Optical length of the SOA	2 mm
att_dB	Power attenuation in waveguides	$1 \cdot 10^3 \text{ dB/m}$
L_{wg}	Optical length of the passive waveguides	12 mm
ΔL_{ch}	Path length difference between Ch1 and CH2	0
$g_{SOA} \cdot L_{SOA}$	SOA total power gain coefficient	3.1
ξ	Width AWG channel	0.12 mm

Table 4.1. List of the values of the input parameters used in the laser model.

Before presenting simulation results of the laser system it is useful to give some attention to the transmission spectrum of the filter depicted in Fig. 4.19. Two extreme cases are presented here that give a qualitative idea of the impact that the cross-talk in the AWG has on the behavior of the filter. In Fig. 4.20 the transmission spectrum of the filter in two states is compared. The red line is the spectrum when all the PHMs of the filter are grounded ($V_{1A} = V_{2A} = V_{1B} = V_{2B} = 0 \text{ V}$). The blue line presents the spectrum of the filter in which a phase delay of π is at 1550 nm is applied to both PHMs of Channel 2 ($V_{1A} = V_{2A} = 0 \text{ V}$, $V_{1B} = V_{2B} = V_\pi$).

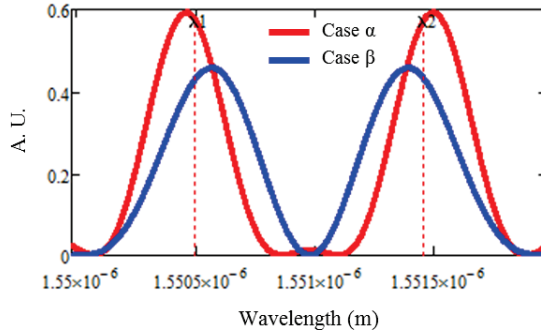


Fig. 4.20: Two extreme cases of the transmission function of the filter depicted in Fig. 4.19. α) The red line presents the result for $V_{1A} = V_{2A} = V_{1B} = V_{2B} = 0$ V. The frequency difference between the peaks is 4.1% larger than the channel spacing of the AWG. β) The blue line presents the result for $V_{1A} = V_{2A} = 0$ V, $V_{1B} = V_{2B} = V_{\pi}$. The frequency difference between the peaks is 4.4% smaller than the channel spacing of the AWG.

According to the design and to the model presented in section 3.3, the settings applied to the PHMs of the filter should have an impact only on the tuning of the longitudinal modes and on the control of the losses in the individual channels to control the power at λ_1 and λ_2 . However, Fig. 4.20 shows that the voltages applied to the PHMs for tuning only, dramatically change the frequency difference between the peak transmission wavelengths of Channel 1 and Channel 2. This effect is due to the presence of crosstalk between the channels of the AWG which makes that light at one wavelength can pass through both arms MZIs in the filter. Thus, fully constructive and fully destructive interference between the light paths through the two MZIs and AWG channels can occur. As a consequence of the crosstalk, the two lasing modes of Channel 1 and Channel 2 are not independent because a certain amount of power at λ_1 is present also in Channel 2 and vice versa. Changing the settings applied to the MZIs of Channel 1 (Channel 2) has an impact also on the transmission at λ_2 (λ_1).

This also explains why the dual-wavelength operation depicted in Fig. 4.15 reveals a frequency difference between the main laser modes that is significantly smaller than the channel spacing of the AWG. The settings applied to the MZIs of the filter that were meant to be used for tuning and balancing the two longitudinal modes do not provide independent control. There are not enough degrees of freedom to control the device.

In the formula (4.8) of the model of the filter, the phase of the transmission function of the AWG is considered to be constant at all the wavelengths. However, the phase of the transmission function of an AWG can be linear, parabolic and even more complex [16, 17].

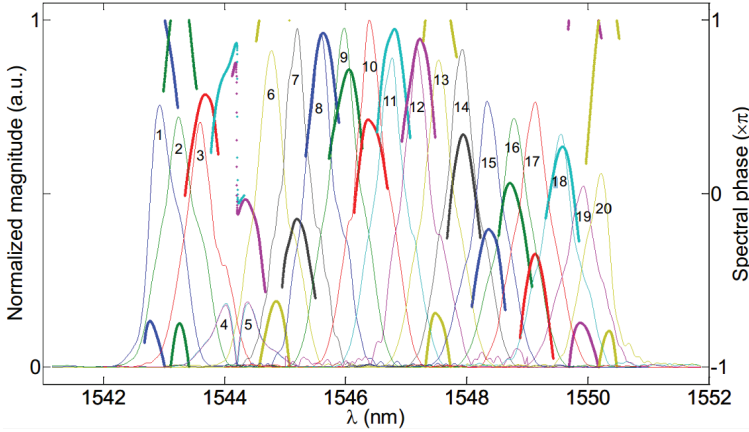


Fig. 4.21. Individual channel response for the 20 device channels of an AWG-based pulse shaper. Channel numbers are indicated on the plot [16].

In Fig. 4.21 the responses of the individual channels of an AWG-based pulse shaper are reported [16]. The spectral phase response curves of the channels can be approximated by a quadratic relation at the center of the channels but a trend close to linear can be noticed at the sides of the channels. The phase offset values vary randomly over the channels. This is due to the fact that the optical path length of each channel cannot be controlled down to the sub-wavelength level during fabrication [16, 17]. In fact, the variations of the responses from channel to channel generate from inaccuracies of the AWG.

To observe the effect of a linear wavelength dependence of the phase in the model, the transmission function of Channel 1 and Channel 2 (see 4.8) were extended to:

$$T_{AWG,1}(\lambda_i) = \left[\frac{\sin\left(\frac{\lambda_i - \lambda_1}{\xi\sqrt{2}}\right)}{\left(\frac{\lambda_i - \lambda_1}{\xi\sqrt{2}}\right)} \right] \cdot e^{i\left(\frac{\lambda_i - \lambda_1}{\xi\sqrt{2}}\right)L_1} \quad (4.18)$$

$$T_{AWG,2}(\lambda_i) = \left[\frac{\sin\left(\frac{\lambda_i - \lambda_1}{\xi\sqrt{2}}\right)}{\left(\frac{\lambda_i - \lambda_1}{\xi\sqrt{2}}\right)} \right] \cdot e^{i\left(\frac{\lambda_i - \lambda_1}{\xi\sqrt{2}}\right)L_2} \quad (4.19)$$

In these equations, L_n is a parameter which determines the slope of the phase dependence. The value of L_n can be positive or negative and is typically in the order of 1. The value of L_1 and L_2 can be very different, however as a first example the transmission function through the AWG is calculated for $L_1, L_2 = 1.4$. This has a very clear effect on the filter transmission as depicted in Fig. 4.22. Fig. 4.22a shows the power (red line) and the phase (blue line) of the transmission function from Channel 1 to the common channel of the AWG according to formula (4.18). Fig. 4.22b shows the transmission function of the total filter. It is clear that the phase of the transmission through the AWG makes the control of the devices extremely complicated.

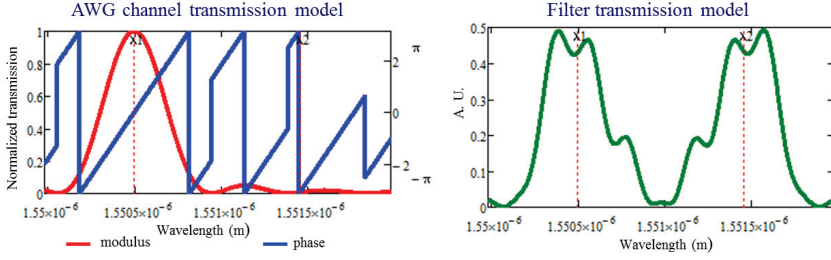


Fig. 4.22: Transmission function through the AWG according to formulas (4.18) and (4.19). a) power (red line) and the phase (blue line) of the transmission function from Channel 1 to the common channel of the AWG. b) Transmission function of the complete filter.

Nevertheless, a qualitative correspondence can be found between the experimental data and the simulated behavior of the device. As shown in Fig. 4.23 the effects caused by the AWG crosstalk and the phase of the AWG transmission function can lead to the presence of unexpected features in the output sub-threshold spectra of the device such as the formation of a lobe of modes between Channel 1 and Channel 2. Several approximations have been used to model the phase transmission in the channels (linear, quadratic, Lorentzian): the effect on the phase for different AWG channels can be similar to such a description. The fact that we have no information about the phase outside the channels makes the system even more complicated to be modelled. It is clear that the phase transmission differences between the different channels (combined with the effect of the crosstalk) have a dramatic impact on the system and on the possibility to control it. In Fig. 4.23, a linear phase dependency is used for Channel 1 and a quadratic one for Channel 2. For the case depicted in Fig. 4.23b the transmission functions are defined as:

$$T_{AWG,1}(\lambda_i) = \left[\frac{\sin\left(\frac{\lambda_i - \lambda_1}{\xi\sqrt{2}}\right)}{\left(\frac{\lambda_i - \lambda_1}{\xi\sqrt{2}}\right)} \right] \cdot e^{i\left(\frac{\lambda_i - \lambda_1}{\xi\sqrt{2}}\right) \cdot L_1} \quad (4.20)$$

$$T_{AWG,2}(\lambda_i) = \left[\frac{\sin\left(\frac{\lambda_i - \lambda_2}{\xi\sqrt{2}}\right)}{\left(\frac{\lambda_i - \lambda_2}{\xi\sqrt{2}}\right)} \right] \cdot e^{i\left(\frac{\lambda_i - \lambda_1}{\xi\sqrt{2}}\right)^2 \cdot Q_2} \quad (4.21)$$

where the parameter values $L_1 = 3.5$ and $Q_2 = 1.5$ have been used.

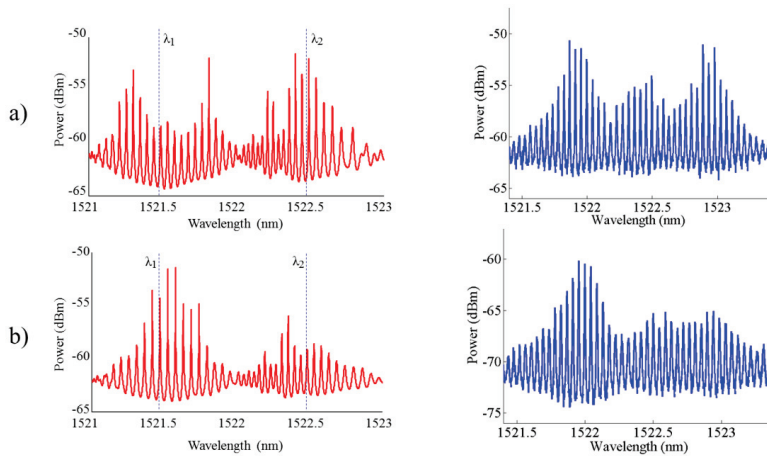


Fig. 4.23. A qualitative correspondence can be found between the experimental data (right) and the simulated behavior of the device (left, calculated for $\lambda_1 = 1521.54$ nm and $\lambda_2 = 1522.5$ nm). The effects caused by the AWG crosstalk and the phase of the AWG transmission function can lead to the presence of unexpected features (b) in the output spectra of the device as well as to the formation of a third lobe between Channel 1 and Channel 2 (a). In this example, linear phase dependency is used for Channel 1 and a quadratic one for Channel 2 according to formulas (4.20) and (4.21).

The effect of crosstalk and the phase variation within the channel makes the prediction of the output spectra of the device unpractical since the behavior of the cross-talk and the phase behavior of the fabricated AWG cannot be predicted sufficiently accurately. Also a systematic control of the losses in the two channels and the tuning of the two lasing modes is not possible in the device.

4.6 Ring laser linewidth and stability

As explained in section 3.3, since λ_1 and λ_2 are generated and amplified by the same SOA, the instantaneous frequency fluctuations in the ring laser due to spontaneous emission and carrier density variations in the SOA are identical for both longitudinal modes. Therefore, we expect such a dual mode device to outperform to similar single longitudinal mode devices. The optical linewidth of a single mode from the laser design presented in this section is therefore the reference relevant to the analysis of the device. Two linewidth measurement methods have been used. The first is the self-heterodyne method which gives a linewidth value on a relatively short time scale. The second method is based on the measurement of the transmission of the laser light through an etalon. This method is suitable for observing variations of the laser frequency over longer times. Both methods and results are presented first and are followed by a discussion of the results.

In Fig. 4.24 the block schematic of the setup used for the self-heterodyne linewidth experiment is depicted [18]. An isolator prevents feedback into the laser under test. A 3dB splitter divides the light in two branches. The delay line is 25239 m long which means that the linewidth variations over more than 124 μ s are not detected (considering a mode index of 1.4682 for SMF-28). In the

other branch a polarization controller (PC) is inserted before a 10 GHz LiBNO₃ acoustic-optical modulator (AOM). This modulator shifts the frequency of the laser light in this arm over 2 GHz. After recombining the two branches, the light is directed towards a 50 GHz u²t photodiode connected to an Agilent E4448A PSA electrical spectrum analyzer (ESA). The ESA then shows a signal around 2 GHz and the width of this signal is interpreted as twice the linewidth of the laser.

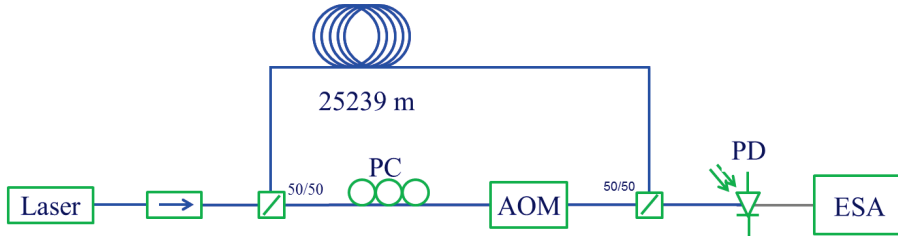


Fig. 4.24: Block schematic of the setup used for the self-heterodyne linewidth measurement.

Fig. 4.25b shows the optical spectrum from the primary output of the ring laser while the device operates in single mode. The current in the SOA is equal to 185 mA, 32 mA above threshold and the voltages applied to the PHMs are $V_{1A} = V_{2A} = V_{1B} = 0$ V, $V_{2B} = 0.8$ V. The FWHM of the signal at the ESA is 8.0 MHz (Fig. 4.25a) which proves an optical linewidth equal to 4.0 ± 0.02 MHz. This value is considerably larger than linewidth values reported on self-heterodyne measurements of DBR lasers and AWG based laser [19, 20].

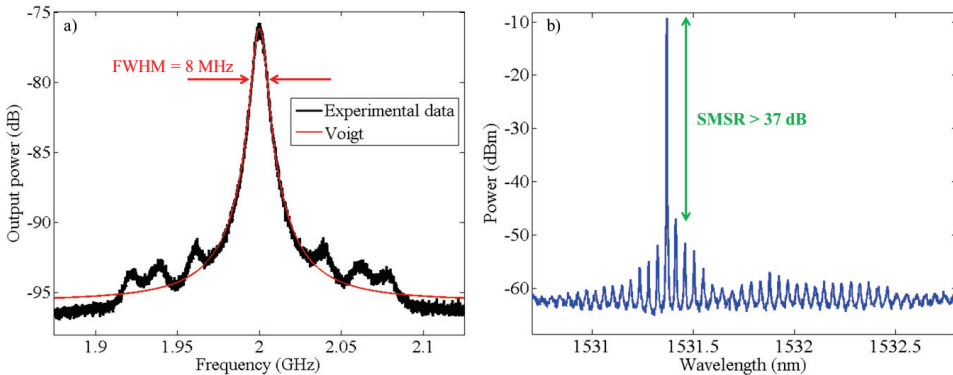


Fig. 4.25. a) Measured linewidth of the ring laser while operating in single mode. The fitted curve with Voigt profile reveals a linewidth of 4 MHz. b) Output optical spectrum of the ring laser.

Since, according to Chusseau [21], a stable dual-wavelength regime is possible only when the coupling factor between the modes is weak enough, the linewidth of the modes should be measured also in dual mode operation and compared to the single mode case. However, in order to be able to measure the linewidth during dual mode operation with the self-heterodyne method, a filter is required. Indeed, it is necessary to select only λ_1 and λ_2 and measure the linewidth of one longitudinal mode per time. This experiment is not presented in this thesis. A second generation

AWG-based dual wavelength laser has been designed in which a second AWG is used as filter to separate the two longitudinal modes into two different output waveguides. This design is presented in section 6.2 and allows for measuring separately the linewidth of each longitudinal mode while operating in dual mode.

From Fig. 4.26 a preliminary indication of the impact of dual mode behavior on the linewidth of the longitudinal modes can be derived. In Fig. 4.26a, the output spectrum of the ring laser is shown during single mode operation. The spectrum has been recorded using an APEX Technologies AP2041 spectrometer with 20 MHz resolution. The figure shows only the lasing longitudinal mode (span = 7.5 GHz) in order to show the shape of the mode itself. Fig. 4.26b presents the spectrum around the same mode (Channel 1) while the laser is operating in dual mode (see insert). The difference between the wavelength of the mode in a) and b) is due to the impact of the different settings applied to the PHMs of the MZIs used to obtain dual mode, as explained in section 4.5. From Fig. 4.26, it is possible to have the preliminary indication that no significant enhancement of the linewidth of the longitudinal modes can be observed while passing from single mode to dual mode operation. Although the resolution and the principle of operation of the spectrometer do not allow for resolving the linewidth of the mode (~ 4 MHz), the absence of a significant enhancement is an indication of that the stability is not deteriorated in dual mode operation.

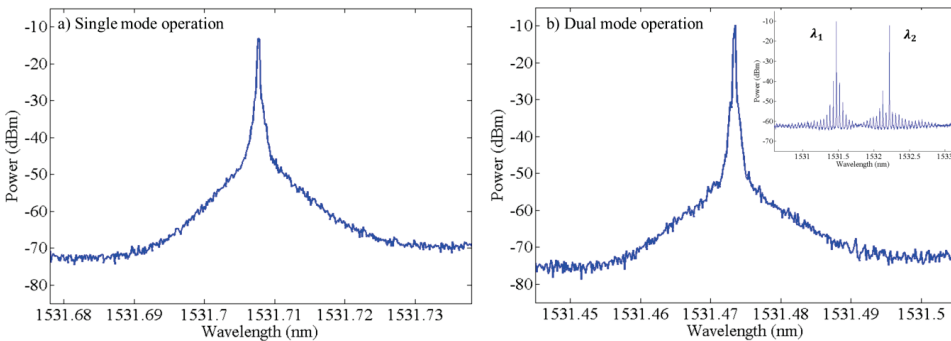


Fig. 4.26. a) Detail of the output optical spectrum of the ring laser in single mode operation: lasing longitudinal mode through Channel 1. b) Detail of the output optical spectrum of the ring laser in dual mode operation: lasing longitudinal mode through Channel 1. In the insert, the spectrum is presented for a larger span in order to show both λ_1 and λ_2 . No significant enlargement of the linewidth of the longitudinal mode can be noticed between a) and b).

The study of the linewidth however is not sufficient to investigate the stability of the lasing modes over a time longer than approximately $100 \mu\text{s}$. During the characterization of the ring laser we noticed on the high-resolution optical spectrum analyzer that there is a drift in frequency of the longitudinal modes over up to hundreds of MHz at these longer time scales.

In order to quantify this drift, we used the setup depicted in Fig. 4.27 to measure the frequency deviations over several time scales. In this method the slope of the filtering function of a Fabry-Perot etalon is exploited. The wavelength of the laser is tuned to the slope of a peak in the transmission spectrum of the etalon. Frequency fluctuations of laser light passing through the etalon are thus converted in amplitude modulations which can be detected. From these amplitude fluctuations and correcting for the amplitude fluctuations of the laser itself, one can derive the

frequency fluctuations. In the setup the light from the laser under test passes through an isolator and an attenuator. A 3dB splitter is used to divide the light into two branches. In the upper branch, the light is directed towards a New Focus 2053-FC photodiode connected to two channels of a LeCroy LT584L 1 GHz oscilloscope (OSC). One channel is AC coupled and the other is DC coupled. The two channels are used to overcome the limited dynamic range (8 bits) of the OSC. In the bottom branch, the light goes through a 25 GHz etalon before being directed towards a PDA50B Thor photodiode connected to one AC coupled channel and one DC coupled channel of the same OSC. The PD of the upper branch detects the amplitude fluctuations of the lasing mode of the laser. In the following this branch is called the AM branch. The PD of the bottom branch detects both the amplitude fluctuations and the frequency fluctuations of the lasing mode. In the following this branch is called AMFM branch.

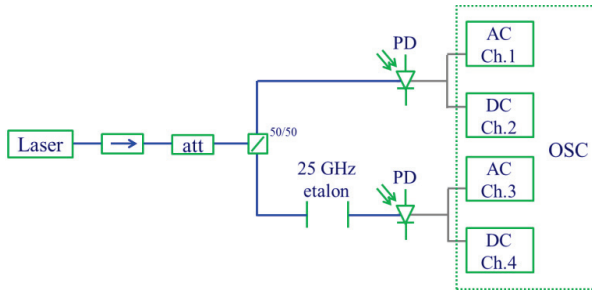


Fig. 4.27: Block schematic of the setup used to investigate the frequency stability of the ring laser.

The experiment requires an initial calibration. A commercial tunable laser is connected to the setup and swept over 25 GHz in order to find the conversion factor from frequency to voltage. The voltage from peak to peak of channel 4 (DC coupled of the AMFM branch) in Fig. 4.27 while sweeping the tunable laser is recorded and we can approximate the conversion from voltage to frequency using a linear conversion factor $k_{V \rightarrow f}$:

$$k_{V \rightarrow f} = \frac{\Delta f}{V_{pp_AMFM_DC}} \quad (4.22)$$

where $V_{pp_AMFM_DC}$ is the peak-to-peak voltage recorded by the DC coupled channel of AMFM branch and Δf is equal to 12.5 GHz corresponding to half of the free spectral range of the etalon. After that, the device under test is tuned to the center of the slope of the filter. Fig 4.28 shows the output spectrum of the ring laser (blue line) with the longitudinal lasing mode centered to the middle of the slope of the filtering function of the filter (green line).

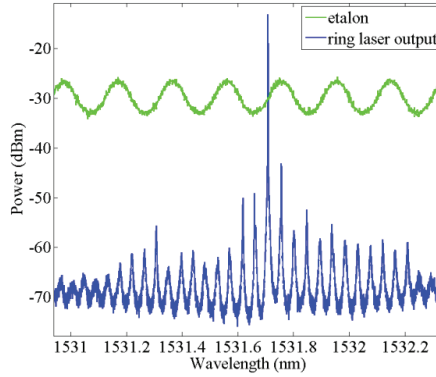


Fig. 4.28: Output spectrum of the ring laser (blue line) with the longitudinal lasing mode centered to the middle of the slope of the filtering function of the filter (green line). The green line corresponds to the spectrum of output light of an erbium doped fiber amplifier (EDFA) filtered with the etalon.

A scaling factor is required in order to take into account the different responsivities of the two photodetectors used for the experiment and the different optical losses in the two arms of the setup. The voltage values (averaged over a 50 s time) recorded in Channel 2 and Channel 4 of the oscilloscope are respectively named as V_{AM_DC} and V_{AMFM_DC} . We can then calculate the scaling factor as:

$$k_s = \frac{V_{AMFM_DC}}{V_{AM_DC}} \quad (4.23).$$

The scaling factor k_s is used to multiply the AC peak-to-peak voltage of the AM branch ($V_{pp_AM_AC}$) and obtain a voltage change (indicated with V_{AM} and corresponding to the maximum amplitude fluctuation) that can be consistently compared with AC peak-to-peak voltage of the AMFM branch ($V_{pp_AMFM_AC} = V_{AMFM}$). In formulas:

$$V_{AM} = V_{pp_AM_AC} \cdot k_s \quad (4.24).$$

Subtracting V_{AM} from V_{AMFM} we can obtain the voltage change (indicated with V_{FM}) caused by the frequency fluctuations of the laser under test:

$$V_{FM} = V_{AMFM} - V_{AM} \quad (4.25).$$

Finally, multiplying V_{FM} with the conversion factor $k_{V \rightarrow f}$ the maximum extension of the frequency fluctuations of the laser under test is found:

$$\Delta f_{FM} = V_{FM} \cdot k_{V \rightarrow f} \quad (4.26).$$

We have studied the fluctuations for different time scales: from 2 seconds up to 50 seconds and the drifting Δf_{FM} has been estimated to be in the order of 230 MHz (248 MHz in the worst case recorded).

We believe that these deviations are caused by technical noise coming from the current and voltage suppliers used to bias the SOA and control the PHMs. The frequency spectrum of the signal transmitted through the etalon which is observed on the AC coupled channel, shows 1/f noise (12 dB/octave reduction) up to 20kHz where the signal becomes equal to the noise level of the detection system. In addition to this some specific low frequency peaks at e.g. 50Hz can be observed. The observed noise is therefore identified as technical noise.

Therefor in principle a feedback control circuit with a control bandwidth of 20kHz or more can be implemented in order exploit the tuning mechanism of the device to stabilize the frequency of the lasing mode with respect to this etalon.

4.7 Conclusions

A dual wavelength ring laser has been designed and fabricated on a 4QW active-passive wafer. Test structures have been used to characterize the SOA and the AWG. A method to characterize directly and indirectly the PHMs of the MZIs of the ring laser has been used in order to calibrate the control system of the device.

The ring laser operates nicely unidirectional thanks to the optical feedback provided by the facet of one output waveguide. An SMSR larger than 41 dB can be achieved when the device operates single mode.

Stable dual-wavelength operation has been proved. The demonstration of experimental dual-mode operation of QW based devices with a single SOA represents an important result. As explained in section 1.4, the fact that two modes share a common SOA can lead to instabilities. There are theoretical predictions that even if the laser cavity allows dual-mode lasing operation, the gain medium nonlinearity can forbid simultaneous emission of the two modes [21]. Chusseau et al. suggest that stable dual-wavelength operation can most likely not be achieved experimentally if the two modes are separated by less than the homogeneous linewidth of the gain medium which is approximately 1.6 THz [21, 22].

A subthreshold analysis and a laser model have been exploited to investigate the behavior of the device. The effect of crosstalk and the phase variation within the channel makes the prediction of the output spectra of the device unpractical since the behavior of the cross-talk and the phase behavior of the fabricated AWG cannot be predicted sufficiently accurately. Furthermore, a systematic control of the losses in the two channels and the tuning of the two lasing modes is not possible in the device.

The single mode linewidth of the laser is 4.0 MHz on a time scale of approximately 100 μ s and drifts over 230MHz on the timescale of seconds. From the optical spectra, no significant enhancement of the linewidth can be noticed when passing from single mode to dual mode operation. This is a preliminary indication that the stability of the dual mode behavior of the ring laser is as good as that of the single mode laser.

The linear configuration of the AWG-based dual-wavelength laser is significantly different from the ring. A study of such a linear dual wavelength configuration is presented and studied in Chapter 5.

References

- [1] G. Carpintero, K. Balakier, Z. Yang, R.C. Guzmán, A. Corradi, A. Jimenez, G. Kervella, M.J. Fice, M. Lamponi, M. Chitoui, F. van Dijk, C.C. Renaud, A. Wonfor, E.A.J.M. Bente, R.V. Penty, I.H. White, and A.J. Seeds, "Microwave photonic integrated circuits for millimeter-wave wireless communications", *Journal of Lightwave Technology*, vol. 32, no. 20, pp. 3495-3501, October 2014.
- [2] M.K. Smit, and Cor van Dam, "PHASAR-Based WDM-Devices: Principles, Design and Applications", *J. of Sel. Topics in Quantum Electron.*, vol. 2, no. 2, June 1996 .
- [3] Y. Barbarin, "1.55 μm integrated modelocked semiconductor lasers," PhD thesis, Technische Universiteit Eindhoven, The Netherlands, 2007.
- [4] N. Ismail, F. Sun, G. Sengo, K. Wörhoff, A. Driessen, R.M. de Ridder, and M. Pollnau, "Improved arrayed-waveguide-grating layout avoiding systematic phase errors" *Optics Express*, Vol. 19, Issue 9, pp. 8781-8794, 2011.
- [5] Emil Kleijn, Meint Smit, and Xaveer Leijtens, "New analytical arrayed waveguide grating model", *J. Lightwave Technol.*, vol. 31, no. 20, pp. 3309-3314, October 2013.
- [6] S. Latkowski, T. De Vries, L. Augustin, M. Smit, E.A.J.M. Bente A Monolithically Integrated Tunable Single Longitudinal Mode Extended Cavity Ring Laser Using Intracavity Mach-Zehnder Interferometers, in *Proceedings of the 18th Annual Symposium of the IEEE Photonics Society Benelux Chapter*, Eindhoven, Netherlands, 2013.
- [7] X.J.M. Leijtens, P. Le Lourec, and M.K. Smit, "S-matrix oriented CAD-tool for simulating complex integrated optical circuits", *J. of Sel. Topics in Quantum Electron.*, vol. 2, no. 2, pp. 257-262, June 1996.
- [8] E. Kleijn, D. Melati, A. Melloni, T. de Vries, M.K. Smit, and X.J.M. Leijtens, "Multimode interference couplers with reduced parasitic reflections", *IEEE Photon. Technol. Lett.*, vol. 26, no. 4, pp. 408-410, February 2014.
- [9] B.W. Hakki and T.L. Paoli, "Gain spectra in GaAs double-heterostructure injection lasers," *Journal of Applied Physics* vol. 46, no. 3, pp. 1299-1306, 1975.
- [10] C. H. Henry, R. A. Logan and F. R. Merritt, "Measurement of gain and absorption spectra in AlGaAs buried heterostructure lasers," *Journal of Applied Physics*, vol. 51, no. 6, pp. 3042-3051, 1980.
- [11] P. Blood, A. I. Kucharska, J. P. Jacobs and K. Griffiths "Measurement and calculation of spontaneous recombination current and optical gain in GaAs-AlGaAs quantum-well structures," *Journal of Applied Physics*, vol. 70, no. 3, pp. 1144-1156, 1991.
- [12] A. Oster, G. Erbert, H. Wenzel, "Gain spectra measurements by a variable stripe length method with current injection," *Electronics Letters*, vol. 33, no. 10, pp. 864-866, 1997.
- [13] J.D. Thomson, H.D. Summers, P.J. Hulyer, P.M. Smowton, P. Blood, "Determination of single-pass optical gain and internal loss using a multisection device," *Applied Physics Letters*, vol. 75, no. 17, pp. 2527-2529, 1999.
- [14] P.-A. Besse, J.-S. Gu., and H. Melchior, "Reflectivity Minimization of Semiconductor Laser Amplifiers with Coated and Angled Facets Considering Two-Dimensional Beam Profiles" *IEEE Journal Of Quantum Electronics*, vol. 21, no. 6. June 1991.
- [15] L.A. Coldren, S.W. Corzine, M.L. Mashanovitch, "Diode lasers and photonic integrated circuits", 2nd edition, Chichester: Wiley, 2012.
- [16] M.S. Tahvilli, "photonic integrated circuits for shaped pulse laser systems", PhD thesis, Technische Universiteit Eindhoven, The Netherlands, 2013.
- [17] M.S. Tahvili, E. Smalbrugge, X.J.M. Leijtens, M. Wale, M.K. Smit, and E.A.J.M. Bente, "Calibration of an InP-Based Monolithically Integrated Optical Pulse Shaper", *IEEE Photonics Journal* December 2013.
- [18] T. Okoshi, K. Kikuchi, A. Nakayama, "Novel method for high resolution measurement of laser output spectrum", *Electronics Letters*, vol. 16, no. 16, pp. 630-631, 1980.
- [19] F. van Dijk, A. Accard, A. Enard, O. Drisse, D. Make, F. Lelarge, "Monolithic dual wavelength DFB lasers for narrow linewidth heterodyne beat-note generation", *Proceedings of the 2011 IEEE MWP*.

- [20] G. Carpintero, E. Rouvalis, K. Lawniczuk, M. Fice, C.C. Renaud, X.J.M. Leijts, E.A.J.M. Bente, M. Chitoui, F. van Dijk, and A.J. Seeds, “95 GHz millimeter wave signal generation using an arrayed waveguide grating dual wavelength semiconductor laser”, *Optic Letters*, vol. 37, no. 17, September 2012.
- [21] L. Chusseau, F. Philippe, P. Viktorovitch and X. Letartre, “Mode competition in a dual-mode quantum-dot semiconductor microlaser”, *Physical Review A*, vol. 88, no. 1, 015803, July 2013.
- [22] L. Chusseau, F. Philippe, and F. Disanto, “Montecarlo modeling of the dual-mode regime in quantum-well and quantum-dot semiconductor lasers”, *Optics Express*, vol. 22, no. 5, 2014.

CHAPTER 5

Linear laser

Abstract – A linear AWG-based dual wavelength laser has been designed and fabricated in a Multi-Project Wafer run. This chapter focuses on the characterization results of this linear laser. Dual wavelength operation is demonstrated. The advantages and disadvantages of this configuration compared to the ring laser presented in Chapter 4 are described and discussed.

5.1 Linear laser design

The laser device described in this chapter has been fabricated using active/passive regrowth integration technology within a Multi-Project Wafer (MPW) run in the framework of Memphis project [1].

An MPW run is a fabrication in which different designs from different projects are combined on the same wafer. This means that all designs of the PICs share the same fabrication process flow. The MPW runs derive from the generic integration approach and lead to a large reduction of the research and development costs. In photonics, most integration technologies are developed and optimized for a specific application. As a result, there are almost as many technologies as applications. Most of them are very similar, but sufficiently different to prevent easy transfer of a design from one fab to another. The idea behind the generic integration approach originates from the necessity to decrease the costs for the fabrication and the development of PICs. Similarly to what is done in microelectronics, a certain number of basic building blocks (BBBs) can be identified and connected together during the design of different PICs. Examples of BBBs are: waveguides, PHMs, SOAs, MMIs. BBBs can be combined in order to create composed building blocks (CBBs) as e.g. an AWG. The goal is to support the monolithic integration of a small set of accurately characterized building blocks that offer the basic functionality which is required to realize PICs for a broad range of different applications. Such a process, in which a broad range of functionalities can be synthesized from a small set of BBBs, is called “generic integration process”.

An advantage of generic integration technologies is that, because they serve many different applications, they justify the investments in developing the technology for a very high performance and reliability at the level of the building blocks. Furthermore, in a standardized technology we can develop design libraries and a related software infrastructure for components or sub-circuits that are used by many designers. This leads to a significant reduction of the design time and an increase in the design accuracy. Moreover, thanks to the use of generic integration technologies, successful designs can be easily transferred from research to mass production.

In the case of the linear laser presented in this chapter, the MPW run has been performed at Oclaro Technology Ltd (UK). The details of the manufacturing process are kept confidential by the company and are not objects of this thesis.

Mask Engineer from Phoenix BV and Klayout have been used as software tools for the circuit design and the mask design. The Oclaro library embedded in Mask Engineer has been exploited for the design of the components (e.g., AWG). In Fig. 5.1 a picture of the mask layout of the dual wavelength linear AWG-based laser is presented. It corresponds to the linear laser schematic depicted in Fig. 3.1(c) in Chapter 3.

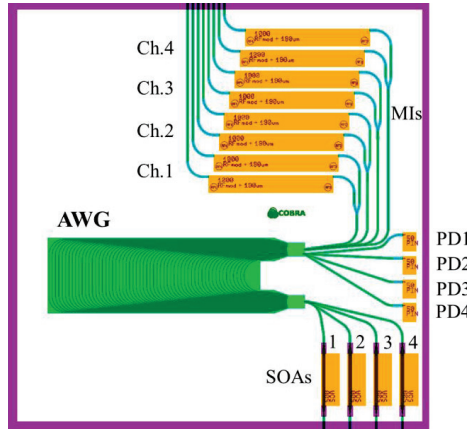


Fig. 5.1. Circuit design of the AWG-based dual wavelength linear laser. It corresponds to the linear laser schematic depicted in Fig. 3.1(c). However, two extensions can be noticed: the presence of four SOAs instead of one and four individual channels instead of two.

All components, apart from the SOAs and PDs, are passive waveguide structures. The mirrors of the laser cavities are formed by the cleaved facets of the chip. In the device layout the AWG takes a large amount of space since it has a relatively small channel spacing of 70 GHz (0.56 nm at 1550 nm). The AWG has a free spectral range of 9 nm. Two extensions can be noticed in comparison with the schematic of Fig. 3.1(c). Firstly, on the bottom side of the device there are four (500 μm long) SOAs instead of only one. These are connected using waveguides to four different positions on the lower FPR of the AWG. In this way, four independent device configurations are available on the same chip. By activating only one of these amplifiers, one of four wavelengths within a free spectral range of the AWG can be selected. Thus the optimal wavelength can be selected with respect to the gain peak of the SOA. Furthermore, this choice provides back-up solutions in case of damage or defects on one (or more) of the waveguides where the SOAs are placed. Secondly, four separate wavelength channels are available from the other FPR of the AWG, each at 70 GHz distance in frequency to one of the SOA connected waveguides. Thanks to this approach, the difference in frequency between the two lasing wavelengths can be chosen to be equal to a multiple of the channel spacing (from 70 GHz to 210 GHz).

One waveguide connects each individual channel to a Michelson interferometer: a 1x2 MMI is used to split the light into the two balanced arms of the MI. Each arm of the MI is provided with a 1 mm long electro-optical PHM. The choice of using 1x2 MMIs (despite the fact that they give higher back-reflection compared to 2x2 MMIs) is due to space constraints: the available area is 4 mm by 4 mm and there is not enough space in the cell to be able to direct the spare output to a facet or to a PD.

On the right hand side of the chip in Fig. 5.1, four 50 μm long monitoring PDs are positioned. The PDs are connected to a higher order of the AWG such that each PD can be used to monitor the level of power in the corresponding individual channel of the device. Isolation sections are present at the input of the PDs and at both ends of the PHMs in order to electrically isolate these components from each other and from the SOAs.

The design layout is subject to limitations given by the standard technology platform. The input/output waveguides can be positioned only at the top and at the bottom facets and the waveguide ends must be positioned on a predefined 25 μm grid. A second point is that SOAs can be oriented only orthogonal to the major flat of the wafer. Thirdly, a PHM can be oriented both parallel and orthogonal to the major flat, but the efficiency is approximately 30% higher when it is parallel.

The lengths of the cavities for λ_1 and λ_2 have not been equalized. Moreover, the length of the cavities is different when biasing a different SOA. The length of the different laser cavities available varies from 9.4 mm to 10.4 mm: the corresponding expected values for the mode spacing are in the range between 3.8 GHz and 4.3 GHz. The wavelength selection results from the combination between the transmission of the AWG and the cavity modes. An analytical model of the AWG predicts a channel width FWHM of 25 GHz and an attenuation of 0.3 dB at 4 GHz distance from the center of the channel. Laser simulations shows that such a channel width provides sufficient suppression of the longitudinal side modes of the cavity: only small loss differences (~ 0.1 dB) are needed for a side mode suppression of 20dB [2].

The position and the length of the PHM has been chosen as a compromise between space on the chip, efficiency of the PHM and accuracy required on the control voltage applied. For the selected orientation, around 1550 nm a 2π shift can be achieved with a reverse bias of 5 V (single pass) for a length of 1 mm. This means that inside the cavity where there is a double pass and for a mode spacing of 4 GHz, a noise level of 10 μV in the control voltage applied will lead to a fluctuation in the order of 16 kHz of the lasing modes.

The position and the length of the SOAs have been chosen in a trade-off between the required gain and the available space. Both aspects play a role on the functioning of the device. The difference in frequency between the modes at λ_1 and λ_2 is around 70 GHz (or 140 GHz or 210 GHz). This gives rise to a spatial pattern caused by the beating of the two modes inside the cavity with a period of approximately 1.2 mm (or 0.6 mm or 0.4 mm), This is comparable to the length of the SOA. Considering that most of the cavity is formed by passive structures, the length and the position of the SOA with respect to the maxima and minima of the spatial pattern determines how the interference between λ_1 and λ_2 may influence the stability of the system and/or lead to tuning effects.

The AWG is the pivotal component of the device. The choice to select the orthogonal version of the AWG is twofold. This version of AWG is smaller than the Alcatel and the Smit ones (the input design parameters being equal). Moreover, the orthogonal version is the one that has been used more extensively during recent years. As a consequence, considerable effort has been spent both on modelling and on characterizing this component configuration [3], making it the most reliable version of AWG. The AWG is a passive component on the Oclaro platform and thus has deeply etched waveguides in the array.

The central wavelength of the AWG is 1550 nm. The channel spacing has been designed to be 70 GHz (0.56 nm) and it determines the coarse tuning between the lasing modes of the adjacent channels. The FSR has been chosen equal to 1120 GHz (8.96 nm). This large FSR is convenient in

order to avoid lasing at different orders of the AWG. Only the wavelengths of the order that is nearest to the top of the gain curve of the SOA should be lasing.

The others input parameters used for the design of this AWG are:

- the polarization: TE since the gain of the QWs in this polarization is highest;
- the width of the input/output waveguides: $w_{io} = 1.5 \mu\text{m}$, the standard deep waveguide width in Oclaro technology;
- the width of the array waveguides: $w_a = 1.5 \mu\text{m}$, the standard deep waveguide width in Oclaro technology;
- the center-to-center distance between the input/output waveguides: $d_r = 2.5 \mu\text{m}$;
- the width of the openings between the array waveguides at the edge of the FPR: $gap_a = 0.4 \mu\text{m}$;
- the Array Acceptance Factor (AAF) which determines the opening angle of the array of waveguides: $AAF = 3$ [4, 5].

Furthermore, the Rowland distribution has been used for placing the input/output waveguides [6]. No chirp has been added to this AWG design. The other characteristics of the AWG, e.g., size and number of waveguides in the array, are determined by the software (Mask Engineer) based on the given input parameter values.

As for the ring laser, the AWG design selected is a compromise between the available space and the requirements on its optical performance. In particular the AAF, the d_r and the FSR of the AWG are chosen as large as the available space allows.

A picture of one of the fabricated devices is presented in Fig. 5.2. It shows the waveguides and gold contacts on the SOAs and PHMs as well as additional test structures on the chip. A High-Reflection (HR) coating has been applied to the facet of the device on the side of the MIs.

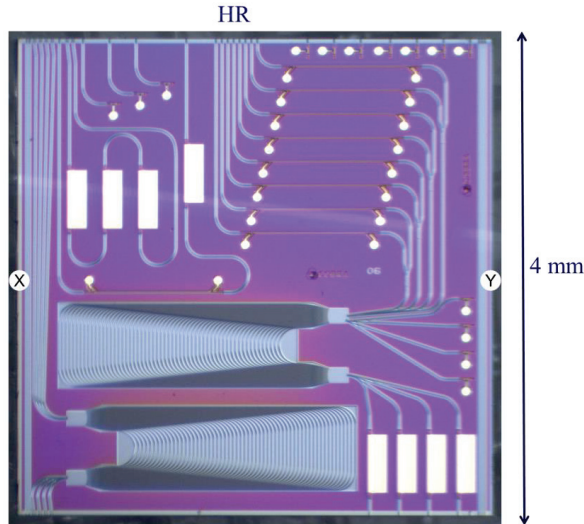


Fig. 5.2. Picture of a fabricated linear laser chip including test structures which are not depicted in Fig. 5.1. The point “X” and “Y” define line used to cleave one of the device in order to obtain a simple AWG-based linear laser in which the MI construction is not present.

5.2 Basic characterization of the linear laser

In this section the basic characterization of the device is reported. Firstly, the characterization of the AWG, the main component of the linear laser, is presented. The AWG transmission spectrum has been characterized directly on the device. A second copy of the chip has been cleaved to be able to characterize the AWG. Secondly, single mode operation of the linear laser is presented. An SMSR larger than 41 dB was demonstrated. Finally, the use of the PDs for monitoring the power in the individual channels of the device is demonstrated. For the characterization a similar set-up and chip mounting was used as described in section 2.4.

5.2.1 AWG characterization

In the case of the ring laser presented in section 4.3.2, characterization of the AWG inside the actual laser cavity was not possible due to the ring configuration of the cavity. Instead the relevant parameters were determined using a test-AWG that was fabricated on the same chip. In the linear cavity structure of the laser presented in this chapter, it is possible to characterize the actual AWG that is used inside the laser as intra-cavity filter. By biasing one of the SOAs (e.g. SOA1) at a current value below the lasing threshold and collecting the ASE light that passes through the AWG and the MI structure from the output waveguides at the top side of the chip in Fig. 5.2, the transmission spectrum of the AWG can be reconstructed. During this experiment, the PHMs are grounded. The graph in Fig. 5.3 presents the optical spectrum. It shows that the actual channel spacing of the AWG is smaller than the designed value: 66 GHz instead of 70 GHz. The channel width FWHM is 29 GHz which is larger than the design value and model prediction of 25GHz.

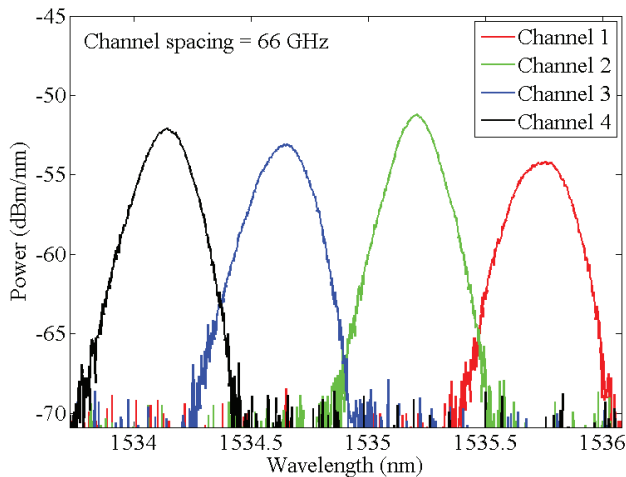


Fig. 5.3. Optical spectra of the ASE from the laser with SOA1 below the lasing threshold and recorded at one of the HR coated facets at the end of one of the MIs. The ASE is filtered by the AWG and the lobes correspond to the AWG channels. The actual channel spacing is smaller than the designed value (66 GHz instead of 70 GHz).

However the channel spectrum is slightly more peaked at the top which results in an attenuation at one cavity mode distance of 4 GHz from the center of the channel of 0.3 dB which matches the simulated value. The low level of power in the spectra of Fig. 5.3 is due to the high-reflective coating on the facet of the device on the side of the MIs. The reason why the spectrum shown in Fig. 5.3 is centered around 1535 nm is that we had already noticed that the device will lase around this wavelength.

One of the fabricated devices has been cleaved through the line indicated by “X” and “Y” in Fig. 5.2 in order to have on one chip only the part of circuit with the SOAs and the AWG. In this way a much simpler AWG-based linear laser has been obtained: the MIs have been excluded from the PIC. Similarly to what is described above, while biasing SOA1 below threshold, the light that now passes only through the AWG has been collected from the output waveguides of the individual channels. At the same time, also the light (ASE) exiting the circuit from the output of the SOA arm has been collected. In this way, the power of the ASE collected on the SOA side can now be compared to the top of the transmission curve of the AWG spectrum. This is shown in Fig. 5.4. Assuming the reflectivity of both facets is the same and ignoring the influence of the short passive waveguide sections on both sides of the AWG it is possible to determine the insertion loss of the AWG to be 7.4 dB (± 0.5 dB).

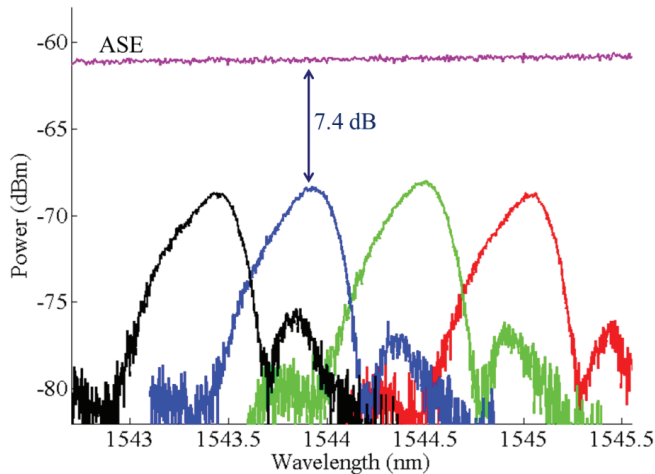


Fig. 5.4. Optical spectra of the ASE recorded from both sides of the shortened linear laser cavity below threshold. The spectrum of each individual channel of the AWG can be seen. The color code is the same of figure 5.3. In addition, here, the violet line indicates the power of the ASE collected directly from the output waveguide connected to SOA3. In this way the losses introduced by the AWG can be estimated around 7.4 dB. Note this is a different AWG and order of the AWG as in Fig 5.3.

The shape of the AWG channels in Fig. 5.4 appears to be slightly different than the one of Fig. 5.3. There can be a number of causes for this. Both devices are from the same fabrication batch but could originate from quite different parts of the wafer. Another possibility is that the spectra in Fig. 5.4 are of a neighboring transmission order of the AWG around 1544 nm instead of the order

around 1535 nm. A third possibility is that the polarization state of the ASE is a bit different. This uncertainty limits the accuracy of the measurement.

Also in this device the channel spacing is 66 GHz. The FSR has been measured to be 8.66 nm. This is smaller than the designed value of 8.96 nm.

5.2.2 Single mode operation

When the PHMs in the MIs are grounded, i.e there is no explicit control of the MI filters, the laser is expected to operate in single AWG channel. The losses in the MI are then essentially random values since the in the fabrication of the devices the path lengths are controlled to a level that is substantially above one wavelength. Also only a small loss difference is needed for the laser to operate on a single channel as discussed in sections 3.1 and 3.3. Fig. 5.5 shows the LI curves recorded while biasing SOA1. The curve presents some peaks and dips which correspond to mode hopping since, as mentioned, no control is applied to the PHMs and consequently the device tend to lase at the wavelength that experiences lower losses. The laser has a threshold current of 39 mA when SOA1 is biased.

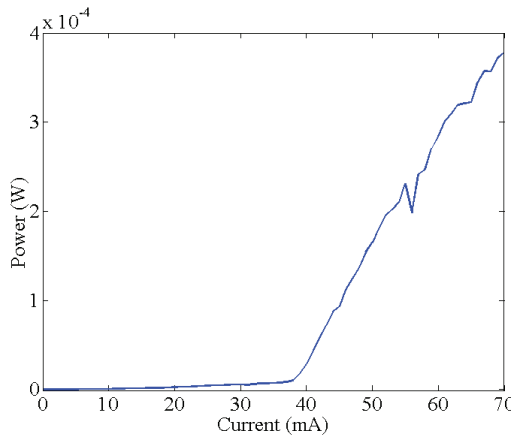


Fig. 5.5. LI curve of the linear laser when SOA1 is biased and the PHMs of the MIs are grounded. The peaks and the dips are due to mode hopping. The threshold current is 39 mA.

As expected, while biasing the common SOA without balancing the losses in the different channels using the MIs, the device lases in a single AWG channel and often in a single mode; the modes in the other channels are suppressed. Indeed, Fig. 5.6 shows an example of single mode operation: channels 2, 3 and 4 are suppressed.

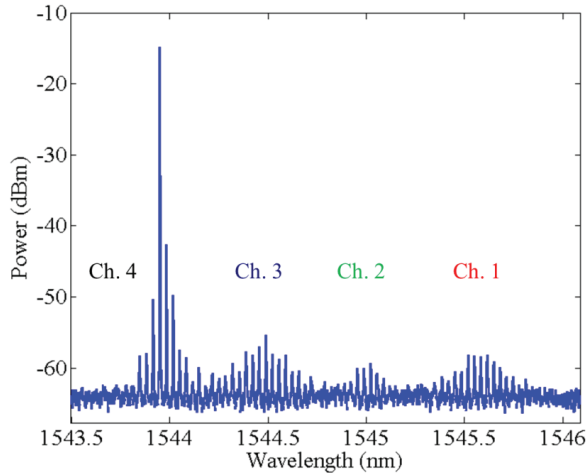


Fig. 5.6. Output spectrum of the linear laser collected from the output waveguide connected to SOA1. SOA 1 is biased at 60 mA. The graph shows that when zero volt is applied to the PHMs of the MIs, the device lases through the individual channel with the lowest losses that is this case is Channel 4.

The spectra of the laser output presented in Fig. 5.6 and Fig. 5.7 have been recorded with a 100 MHz resolution spectrometer, collecting the light from the output waveguide with a lensed fiber directly connected to SOA1. Fig. 5.6 shows that the mode spacing is 4.1 GHz which corresponds to the total length of the laser cavity under test in this measurement of 9.8 mm (assuming a group index value of 3.7). The spectra show no obvious indication of significant intra-cavity reflections. Furthermore, Fig. 5.6 demonstrates a SMSR of 41 dB. Adjusting the settings applied to the PHMs, the value of the SMSR can be increased up to 47.3 dB (Fig. 5.13b). This confirms that the attenuation of 0.3 dB provided by the shape of the channel of the AWG at 4 GHz distance from the center of the channel is enough to obtain single-mode operation in one channel [7].

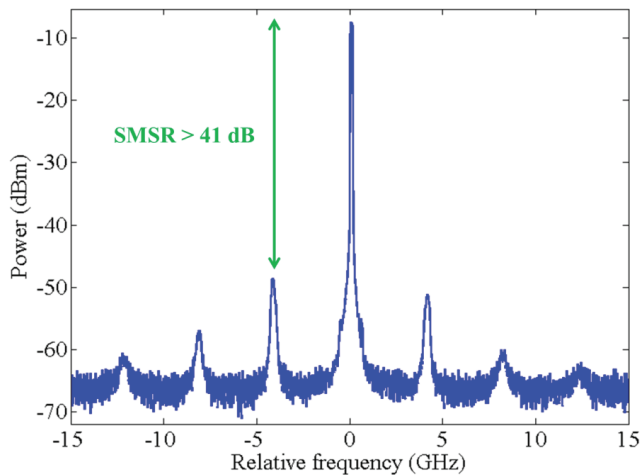


Fig. 5.7. Detail of the output spectrum of the linear laser of Channel 1. The x-axis is shown as relative frequency in GHz in order to make easier to see the mode spacing that is equal to 4.1 GHz. An SMSR higher than 41 dB is demonstrated. SOA1 is bias at 66 mA.

Although the central wavelength of the AWG is 1550 nm and also the SOAs are designed to have the maximum of their gain curve around the same wavelength, the device tends to lase at shorter wavelengths.

5.2.3 Monitoring PDs

In order to derive electrical signals proportional to the optical power present in each individual channel, monitoring PDs have been integrated with the system. A convenient way of getting access to light in the individual channels for monitoring purposes is to use the power in the higher order outputs from the AWG, exploiting the periodic behavior of this component. The signals from PD1, PD2, PD3 and PD4 (Fig. 5.2) can be used to generate the feedback signal for the loss control system (section 3.4) in order to balance the power between two lasing modes in two individual channels while suppressing the other two channels.

As it is explained in section 5.3.1, an automatic feedback control system to balance the power between two individual channels is unpractical for the device presented in this chapter. This is due to the impact of the crosstalk and of the phase behavior of the AWG. In the case of this particular linear laser design the control is also complicated by the fact that four individual channels with MI's are to be controlled in comparison to two channels of the ring configuration presented in Chapter 4. Therefore the goal of this section is limited to showing a proportional dependency between the power in each individual laser channel and the intensity of the signal derived from the corresponding PD.

The device that was cleaved through the line indicated by "X" and "Y" in Fig. 5.2 has been used to characterize the behavior of the monitoring PDs. The reason for this choice is twofold: the complication of the MIs was in this way excluded and it is possible for this device to collect the light from a single output waveguide for each individual channel when operating above the lasing

threshold. Fig. 5.8 shows the output power signal of each individual channel as a function of the current injected in SOA1 (LI curves) together with the photocurrents collected from each PD. The graph refers to a case in which the device operates in single mode through channel 1 with an SMSR larger than 40 dB when the current is higher than 45 mA. The voltages applied to the PHMs are $V_{1A} = -2.7$ V, $V_{1B} = -3.0$ V, $V_{2A} = -1.8$ V, $V_{2B} = 0$ V, $V_{3A} = 0$, $V_{3B} = -4.5$ V, $V_{4A} = -0.4$ V, $V_{4B} = 0$. As expected, the photocurrent in PD3 is (around 10 times) larger than in the other PDs. Because of such a larger SMSR, it is possible to conclude that the photocurrent in PD1, PD2 and PD4 is mainly due to crosstalk between channel 3 and the other AWG channels. Fig. 5.8 demonstrates that the photocurrent of each PD is proportional to the optical power present in the corresponding individual channel.

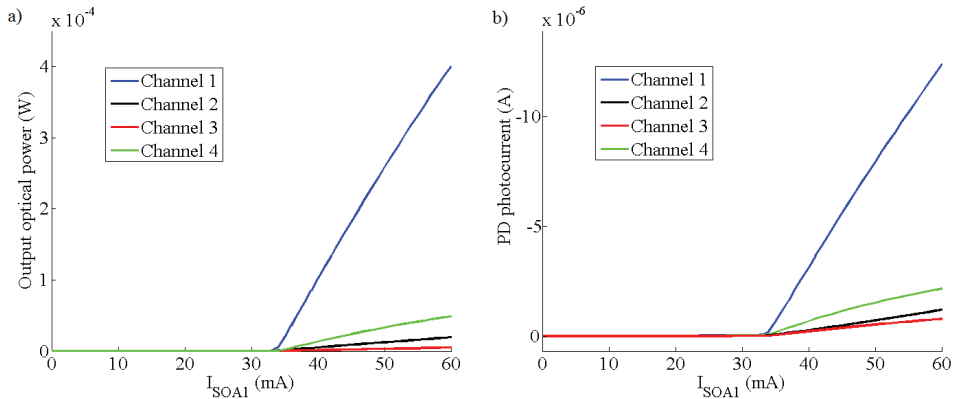


Fig. 5.8. (a) LI curves of the four laser channels in the ‘cleaved laser’ measured at the AWG side of the chip and (b) photocurrents in each corresponding PD. Each color indicates a pair PD-Channel. The device is lasing in single mode through Channel 3 when operated above 45 mA.

By adjusting the temperature of the heat sink of the chip and selecting an SOA for biasing, single mode operation could be obtained for each of the individual channels. This could be used to investigate the response of each PD. Fig. 5.9 shows for each PD the photocurrent as a function of the bias current in the SOA when the device is lasing in a single mode in the channel corresponding to the PD under test. This result demonstrates that the monitoring PDs can be used to estimate the power in the individual channels. The measurements presented in Fig. 5.8 have been taken under the following conditions:

- Channel 1) $T = 12.0$ °C, $V_{1A} = -2.7$ V, $V_{1B} = -3.0$ V, $V_{2A} = -1.8$ V, $V_{2B} = 0$ V, $V_{3A} = 0$, $V_{3B} = -4.5$ V, $V_{4A} = -0.4$ V, $V_{4B} = 0$.
- Channel 2) $T = 12.5$ °C, $V_{1A} = -5.7$ V, $V_{1B} = -3.3$ V, $V_{2A} = 0$, $V_{2B} = -3.6$ V, $V_{3A} = 0$, $V_{3B} = -4.5$ V, $V_{4A} = -2.5$ V, $V_{4B} = -1.1$ V.
- Channel 3) $T = 11.5$ °C, $V_{1A} = 0$, $V_{1B} = -2.9$ V, $V_{2A} = -4.4$ V, $V_{2B} = -1.6$ V, $V_{3A} = -3.3$ V, $V_{3B} = -3.5$ V, $V_{4A} = 0$, $V_{4B} = -5.1$ V.
- Channel 4) $T = 11.8$ °C, $V_{1A} = -3.3$ V, $V_{1B} = -4.5$ V, $V_{2A} = -3.0$ V, $V_{2B} = -4.6$ V, $V_{3A} = -1.5$ V, $V_{3B} = -2.0$ V, $V_{4A} = -2.1$, $V_{4B} = -0.7$ V.

It is important to stress that the photocurrent through the PD can be used as a measure of the optical power of the mode that is lasing through the corresponding channel only if the SMSR within

the channel itself is sufficiently large (approximately larger than 20 dB). In that case one only has to deal with signal perturbations due cross-talk between the channels in the AWG.

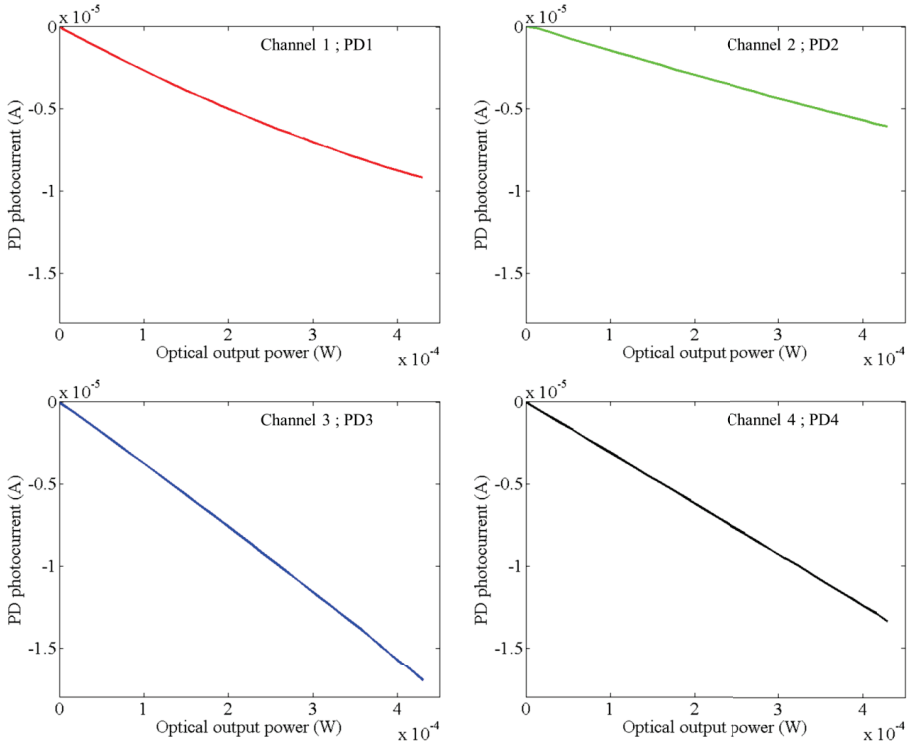


Fig. 5.9. Photocurrent in each PD as a function of the optical power in the corresponding output channel. The values of current, voltages and temperature used for these measurements are listed in the text.

An interesting aspect to be considered is the different response of the PDs for different orders of the AWG. The FSR of the AWG (equal to 8.96 nm) is typically sufficiently large to avoid the laser device to easily jump in its output wavelength from one order to another order of the AWG. If this happens however the power monitoring through the PDs needs to be recalibrated. This is due to the wavelength dependency of the response of the PDs. Different AWG orders have a ~ 9 nm difference in wavelength. Since the PDs are simply reverse biased short SOAs the absorption length in the PD can vary significantly with wavelength. Fig. 5.10 presents a case in which the shortened laser which operates in single mode through channel 4, jumps to a shorter wavelength (different AWG order) when the current reaches the value of 54 mA. Although the photocurrent in PD2 is still proportional to the optical power in Channel 2, the proportionality between the photocurrent and the optical power clearly changes.

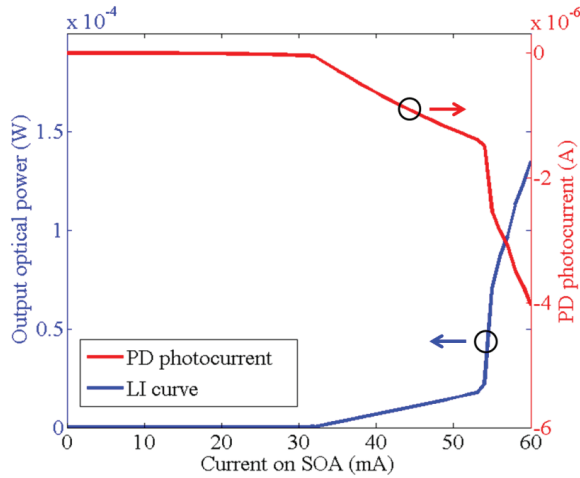


Fig. 5.10. LI curve corresponding to Channel 2 and photocurrent in PD2. When the current reaches the value 54 mA, the laser jumps to another order of the AWG (shorter wavelength) keeping on lasing through Channel 2.

From these results we can conclude that the photodiodes can be used for the power balancing in dual mode operation provided the amount of cross-talk is characterized and the laser is operated in a suitable region away from changes in AWG order. Then the power levels in the two channels can be derived from the signals in two or more photodiodes. Since the balancing does not need to be very accurate this should not be too difficult to achieve.

5.3 Dual mode operation and stability of the laser

In this section, dual mode operation is shown for different combinations of channels and for all the frequency ranges available in the device. Furthermore, the stability of the linear laser is investigated for different time scales, similarly to what is presented in Chapter 4 for the ring configuration.

5.3.1 Dual mode operation

Dual mode operation has been achieved for a number of frequency differences between two channels. In Fig. 5.11, a transition from single mode operation to dual mode operation is depicted. The graph in the insertion shows the spectrum obtained while the common SOA (SOA3 indicated in Fig. 5.1) is biased at 45 mA and all the PHMs of the MI of each channel are grounded. The device is lasing only through one channel. The modes of the channels that are not shown in the picture are suppressed with a suppression ratio > 45 dB. Increasing the voltage on the PHMs of the suppressed channel to 0.20 V (PHM 1A) and 0.88 V (PHM 1B), the losses in two channels have been balanced. As a consequence, lasing occurs also in the channel that was initially suppressed, as shown in Fig. 5.11. In this measurement, the total power collected in fiber is -9.0 dBm (coupling

losses between the output waveguide and the lensed fiber are around 4.5 dB). The difference in power between the two lasing modes is less than 2 dB, which satisfies the requirements. The voltage supplies used performing these measurements have been controlled manually. This represents a remarkable result showing that dual mode operation using one common SOA can be stable. Chusseau et al. suggest that stable dual-wavelength operation can most likely not be achieved experimentally if the two modes are separated by less than the homogeneous linewidth of the gain medium which is approximately 1.6 THz [8, 9].

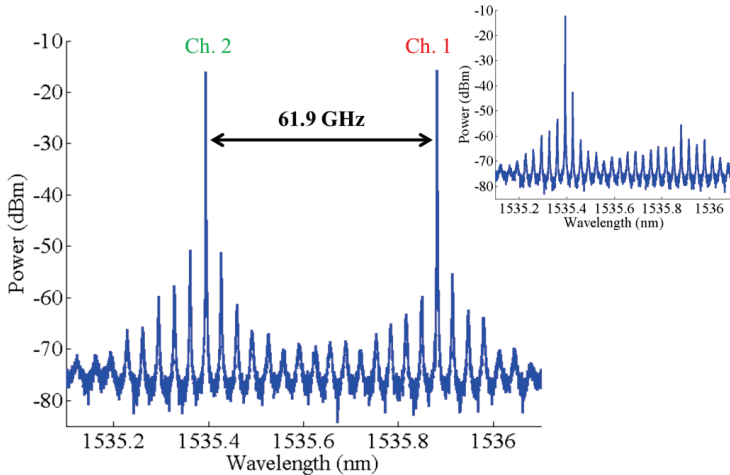


Fig. 5.11. Output spectrum of the linear laser demonstrating stable dual mode operation. The insert on the top right shows the spectrum while all the PHMs are grounded. Dual wavelength operation has been achieved by manually adjusting the losses in the suppressed channel. See text for a description of the operating conditions.

Stable dual wavelength operation has also been achieved between non-adjacent channels with mode distances of 123.7 GHz (Fig. 5.12a) and 199.1 GHz (Fig. 5.12b). The operating conditions in these cases are:

- Fig. 12a) $I_{\text{SOA3}} = 50.0 \text{ mA}$, $V_{1A} = -1.4 \text{ V}$, $V_{1B} = -1.4 \text{ V}$, $V_{2A} = 0$, $V_{2B} = -0.65 \text{ V}$, $V_{3A} = 0$, $V_{3B} = -2.1 \text{ V}$, $V_{4A} = -3.9$, $V_{4B} = -2.7 \text{ V}$
- Fig. 12b) $I_{\text{SOA3}} = 48.5 \text{ mA}$, $V_{1A} = -1.3 \text{ V}$, $V_{1B} = -1.5 \text{ V}$, $V_{2A} = -3.0 \text{ V}$, $V_{2B} = -4.6 \text{ V}$, $V_{3A} = -1.5 \text{ V}$, $V_{3B} = -2.0 \text{ V}$, $V_{4A} = -2.1$, $V_{4B} = -0.7 \text{ V}$.

As it can be noticed from the spectra, the difference in frequency between two lasing wavelengths does not correspond exactly to the actual value of the AWG channel spacing (or to a multiple of it). The differences with the exact multiple of the AWG channel spacing are at most 4.1 GHz which is one cavity mode spacing. This is exactly what one can expect. This means that the effect of the crosstalk between the channels of the AWG is considerably smaller than in the linear configuration. The crosstalk does not differ significantly between the AWG used in the ring laser and the one used in the linear laser. The difference in impact of the crosstalk on the performance of the two devices can be understood. In a linear laser the crosstalk is suppressed two times better than in a ring configuration thanks to the two passes per roundtrip through the AWG compared to the single pass per roundtrip in the ring laser. This represents a considerable advantage

of the linear configuration over the ring configuration. The match of the resulting wavelength differences to the designed difference values between λ_1 and λ_2 is considerably better for the linear laser. Thus the effect of the crosstalk in the AWG is much reduced due to the fact that the light passes it twice during one cavity roundtrip. Calculations on the linear laser mode structure similar to those in section 4.5 on the ring laser, show that there is still some shifting of the transmission maxima with a change of the phases in the MZIs. More importantly the effect of the behavior of the phase in an AWG channel still creates unwanted spectral features and this makes the control of the exact frequency difference between the modes and dual mode operation still unpractical. Furthermore, the presence of four individual channels in this particular design of the linear laser, compared to the two of the ring laser, makes the control more complex.

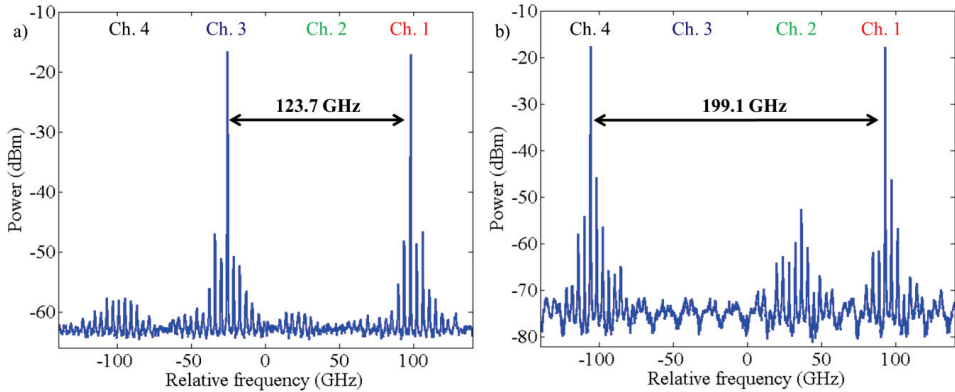


Fig. 5.12. Laser output spectra demonstrating dual mode operation obtained between two non-adjacent channels. The difference frequency between the modes at λ_1 and λ_2 is 123.7 GHz in a) and 199.1 GHz in b). The center wavelength in the spectra is 1535.6 nm. The operating conditions are listed in the text.

An interesting aspect is that a clear hysteresis behavior is observed in the device. The ranges of currents and voltages at which dual wavelength operation are observed are limited and the “capture range” of voltages in which the device goes from single mode to dual mode operation is smaller than the “lock range” of voltages. In this “lock range” the laser keeps staying operating in dual mode. For most of the measurements, capture range and lock range are in the order of 0.02 V and 0.1 V respectively. It appears there is a mechanism in this laser system which actually stabilizes dual mode operation. This phenomenon has not been clearly observed for the ring laser presented in Chapter 4, no such hysteresis was observed there. This indicates that the standing wave pattern generated by the two modes in the cavity plays a role in the stability of the dual mode operation. Note that the ring laser was operating in a uni-directional mode and no standing wave pattern is formed in that device. In dual lasing mode there will be a only travelling beating pattern. This is an dynamics aspect that is interesting for future investigations.

5.3.2 Linewidth and stability of the linear laser

As for the ring laser (Chapter 4), two linewidth measurement methods have been used to investigate the stability of the linear laser. The first technique is the self-heterodyne method which

gives a linewidth value on a relatively short time scale. The second method is based on the measurement of the transmission of the laser light through an etalon. This technique is suitable for observing variations of the laser frequency over longer times. Both methods and results are presented first and are followed by a discussion of the results.

The setup used for the self-heterodyne linewidth experiment is the one used also for the ring laser and depicted in Fig. 4.24 in Chapter 4. Fig. 5.13b shows the output optical spectrum of the linear laser while the device operates in single mode. The SMSR is larger than 47.3 GHz. The current in the SOA is equal to 70 mA, that means 31 mA above threshold current. The voltages applied to the PHMs are $V_{1A} = 0$, $V_{1B} = -3.5$ V, $V_{2A} = 0$ V, $V_{2B} = -4.8$ V, $V_{3A} = -2.5$ V, $V_{3B} = -5.5$ V, $V_{4A} = -1.3$ V, $V_{4B} = -2.7$ V. The FWHM of the signal at the ESA is 1.44 MHz (Fig. 4.25a) which implies an optical linewidth equal to 722 KHz \pm 2 KHz. This value is considerably smaller than the one measured for the ring laser (8 MHz, Chapter 4). Furthermore, it is comparable to linewidths observed from DBR lasers but larger than values reported on self-heterodyne measurements of AWG based laser linewidths [10, 11].

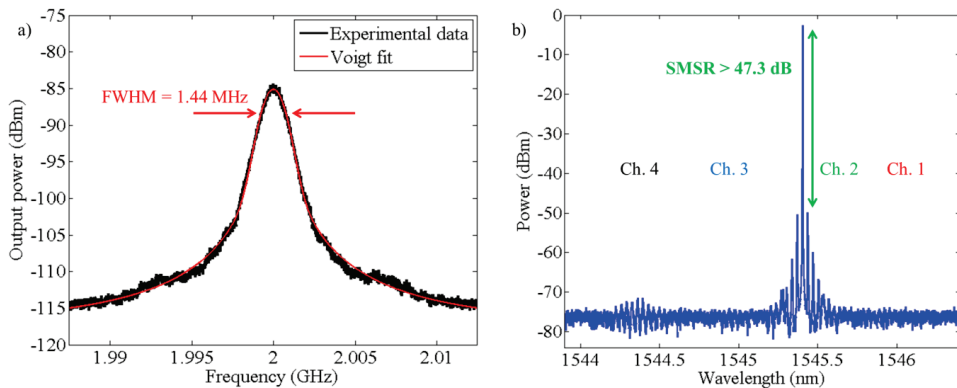


Fig. 5.13. a) The measured signal on the RF analyser in the self-heterodyne set up while the linear laser operates in a single mode. The data are fitted with Voigt profile which reveals a FWHM linewidth of 722 KHz. b) Output optical spectrum of the linear laser for the operating condition of the linewidth measurement (described in the text).

Theoretical predictions presented in [9] state that a stable dual-wavelength regime is possible only when there is only very weak gain competition between the two lasing modes. This means the modes should be separated in frequency by more than the homogeneous linewidth broadening (in the order of 1 THz). We observe dual wavelength lasing where the modes are much closer. It is therefore also interesting to measure the linewidth of the modes in dual mode operation and compare it to the single mode case. A linewidth broadening would indicate a less stable lasing regime. In order to be able to measure the linewidth during dual mode operation with the self-heterodyne method it is necessary to select only λ_1 or λ_2 in order to measure the linewidth of the modes separately. A second generation AWG-based dual wavelength laser has been designed in which a second AWG is used as filter to separate the two longitudinal modes into two different output waveguides. This design is presented in section 6.2.2 and should allow for measuring separately the linewidth of each longitudinal mode while operating in dual mode.

A first indication of the impact of dual mode behavior on the linewidth a less accurate method is used with which the linewidth of the two main longitudinal modes has been obtained. In Fig. 5.14a, the output spectrum of the linear laser is shown during single mode operation (through Channel 4). The spectrum has been recorded using an APEX Technologies AP2041 spectrometer with 20 MHz resolution. The figure shows only the lasing longitudinal mode (span = 5 GHz) in order to show the shape of the mode itself. Fig. 5.14b presents the spectrum around the same mode (Channel 3) while the laser is operating in dual mode (through Channel 3 and 4). The shift in wavelength of the lasing mode is due to the impact of crosstalk and phase of the AWG. Although the resolution and the principle of operation of the spectrometer do not allow for resolving the linewidth of the mode (~ 700 kHz), the absence of an observable enhancement is an indication of that the stability is not deteriorated in dual mode operation. From Fig. 5.14 it follows that if there is a change of the linewidth of the longitudinal modes when going from single mode to dual mode it is less than 2 MHz.

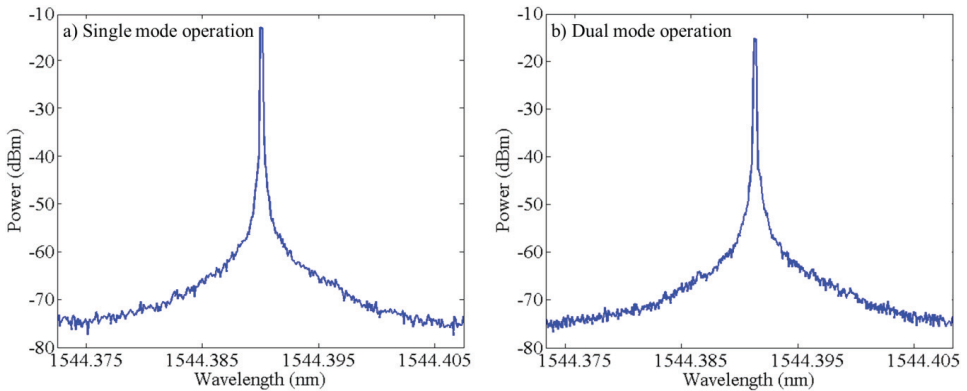


Fig. 5.14. a) Detail of the output optical spectrum of the linear laser in single mode operation: lasing longitudinal mode through Channel 4. b) Detail of the output optical spectrum of the ring laser in dual mode operation: lasing longitudinal mode through Channel 4. No significant enlargement of the linewidth of the longitudinal mode can be noticed between a) and b).

In order to investigate the stability of the linear laser further, we used the setup depicted in Fig. 4.27 in Chapter 4 to measure the frequency deviations over longer time scales. In this method the slope of the filtering function of a Fabry-Perot etalon is exploited. The wavelength of the laser is tuned to the slope of a peak in the transmission spectrum of the etalon. Frequency fluctuations of laser light passing through the etalon are thus converted in amplitude modulations which can be detected. From these amplitude fluctuations and correcting for the amplitude fluctuations of the laser itself, one can derive the frequency fluctuations.

We have studied the fluctuations for different time scales: from 2 seconds up to 50 seconds and the drifting Δf_{FM} has been estimated to be in the order of 150 MHz (162 MHz in the worst case recorded).

We believe that these deviations are caused by technical noise coming from the current and voltage suppliers used to bias the SOA and control the PHMs. The frequency spectrum of the signal transmitted through the etalon which is observed on the AC coupled channel, shows $1/f$ noise

(12 dB/octave reduction) up to 20 kHz where the signal becomes equal to the noise level of the detection system. In addition to this some specific low frequency peaks at e.g. 50 Hz can be observed. The observed noise is therefore identified as technical noise.

Therefor in principle a feedback control circuit with a control bandwidth of 20 kHz or more can be implemented in order exploit the tuning mechanism of the device to stabilize the frequency of the lasing mode with respect to this etalon.

5.4 Conclusions

A dual wavelength linear laser has been designed for a MPW run and has been fabricated in an industrial foundry (Oclaro Technology U.K.). The transmission spectrum and losses of the AWG inside the laser have been characterized.

An SMSR larger than 47 dB can be achieved when the device operates single mode.

Stable dual-wavelength operation has been demonstrated for all three different frequency ranges (70, 140 and 210 GHz) for which it was designed. The demonstration of experimental dual-mode operation of QW based devices with a single SOA represents an important result. As explained in section 1.4, the fact that two modes share a common SOA can lead to instabilities. There are theoretical predictions that even if the laser cavity allows dual-mode lasing operation, the gain medium nonlinearity can forbid simultaneous emission of the two modes [8]. Chusseau et al. suggest that stable dual-wavelength operation can most likely not be achieved experimentally if the two modes are separated by less than the homogeneous linewidth of the gain medium which is approximately 1.6 THz [8, 9].

The PDs present in the device can be used to electrically monitor the power in each individual channel. Future studies can exploit this functionality to control the device using the electrical feedback circuit presented in section 3.4.

A single mode linewidth of the laser of 722 kHz is observed on a time scale of approximately 100 μ s. Frequency drifting is observed up to 162MHz on the timescale of seconds. From the optical spectra, no significant enhancement of the linewidth can be noticed when passing from single mode to dual mode operation. This is a first indication that the stability of the dual mode behavior of the ring laser is as good as that of the single mode laser.

The linear configuration of the AWG-based dual-wavelength laser is significantly different from the ring. The impact of the crosstalk on the device is considerably lower than in the ring laser presented in Chapter 4 thanks to the double pass through the AWG (compared to the single pass in the ring laser). This represents a considerable advantage of the linear configuration that results to match the designed values for the frequency differences between λ_1 and λ_2 considerably better than the ring laser. However, the impact of the crosstalk and the phase in the AWG channels make the control of the device unpractical. Furthermore, the presence of four individual channels in the linear laser (compared to the two of the ring laser) makes the control more complex.

Second generation of devices has been designed in order to combine the advantages of the ring and the linear lasers presented in Chapter 4 and Chapter 5. These devices are presented in Chapter 6 together with a proposed design for a dual wavelength laser based on MZIs instead of an AWG.

References

- [1] M. Smit, X. Leijtens, H. Ambrosius, E. Bente, J. van der Tol, B. Smalbrugge, T. de Vries, E.-J. Geluk, J. Bolk, R. van Veldhoven, L. Augustin, P. Thijs, D. D'Agostino, H. Rabbani, K. Lawniczuk, S. Stopinski, S. Tahvili, A. Corradi, E. Kleijn, D. Dzibrou, M. Felicetti, E. Bitincka, V. Moskalenko, J. Zhao, R. Santos, G. Gilardi, W. Yao, K. Williams, P. Stabile, P. Kuindersma, J. Pello, S. Bhat, Y. Jiao, D. Heiss, G. Roelkens, M. Wale, P. Firth, F. Soares, N. Grote, M. Schell, H. Debregeas, M. Achouche, J.-L. Gentner, A. Bakker, T. Korthorst, D. Gallagher, A. Dabbs, A. Melloni, F. Morichetti, D. Melati, A. Wonfor, R. Penty, R. Broeke, B. Musk, and D. Robbins, "An introduction to InP-based generic integration technology," *Semiconductor Science and Technology*, vol. 29, no. 8, p. 083001, Jun. 2014.
- [2] S. Latkowski, T. De Vries, L. Augustin, M. Smit, E.A.J.M. Bente, "A Monolithically Integrated Tunable Single Longitudinal Mode Extended Cavity Ring Laser Using Intracavity Mach-Zehnder Interferometers," in *Proceedings of the 18th Annual Symposium of the IEEE Photonics Society Benelux Chapter*, Eindhoven, Netherlands, 2013.
- [3] E. Kleijn, "Passive components in indium phosphide generic integration technologies", PhD thesis, Technische Universiteit Eindhoven, The Netherlands, 2014.
- [4] M.K. Smit, and Cor van Dam, "PHASAR-Based WDM-Devices: Principles, Design and Applications", *J. of Sel. Topics in Quantum Electron.*, vol. 2, no. 2, June 1996 .
- [5] Y. Barbarin, "1.55 μm integrated modelocked semiconductor lasers," PhD thesis, Technische Universiteit Eindhoven, The Netherlands, 2007.
- [6] N. Ismail, F. Sun, G. Sengo, K. Wörhoff, A. Driessen, R.M. de Ridder, and M. Pollnau, "Improved arrayed-waveguide-grating layout avoiding systematic phase errors" *Optics Express*, Vol. 19, Issue 9, pp. 8781-8794, 2011.
- [7] A. Corradi, G. Carpintero, B.W. Tilma, M.K. Smit, and E.A.J.M. Bente, "Integrated dual-wavelength semiconductor laser systems for millimeter wave generation", *Proceedings of the 23rd International Semiconductor Laser Conference (ISLC)*, October 2012.G.
- [8] L. Chusseau, F. Philippe, P. Viktorovitch and X. Letartre, "Mode competition in a dual-mode quantum-dot semiconductor microlaser", *Physical Review A*, vol. 88, no. 1, 015803, July 2013.
- [9] L. Chusseau, F. Philippe, and F. Disanto, "Montecarlo modeling of the dual-mode regime in quantum-well and quantum-dot semiconductor lasers", *Optics Express*, vol. 22, no. 5, 2014.
- [10] F. van Dijk, A. Accard, A. Enard, O. Drisse, D. Make, F. Lelarge, "Monolithic dual wavelength DFB lasers for narrow linewidth heterodyne beat-note generation", *Proceedings of the 2011 IEEE MWP*.
- [11] G. Carpintero, E. Rouvalis, K. Lawniczuk, M. Fice, C.C. Renaud, X.J.M. Leijtens, E.A.J.M. Bente, M. Chitoui, F. van Dijk, and A.J. Seeds, "95 GHz millimeter wave signal generation using an arrayed waveguide grating dual wavelength semiconductor laser", *Optic Letters*, vol. 37, no. 17, September 2012.

CHAPTER 6

Conclusions and outlook

Abstract – In this chapter the results obtained from the devices presented in Chapter 4 and 5 are summarized. Two design configurations of new generation AWG-based devices are presented. The goal of the new generation devices is to combine the advantages of the linear and the ring laser presented in the previous chapters. Finally, an alternative design based on asymmetric MZIs instead of an AWG is presented.

6.1 Conclusions

As a partner in the iPHOS project, Eindhoven University of Technology had the task to explore the feasibility of realizing monolithically integrated AWG-based dual-wavelength lasers suitable for millimeter wave generation. The goal was to design and fabricate on an active/passive InP chip, a laser which can deliver simultaneously two lasing modes from the same output waveguide. Furthermore, the device had to exploit the filter function of an AWG. The AWG determines the coarse tuning of the two wavelengths.

The target frequency differences between the two lasing wavelengths (the frequencies of the mm-waves that can be generated by beating the two modes) are 70 GHz and 120 GHz. We have designed and fabricated devices aiming for both frequencies.

The basic idea behind the work presented in this thesis is to investigate photonic integrated dual-wavelength lasers in which the frequency fluctuations of the two wavelengths λ_1 and λ_2 are correlated. This can be obtained using a dual-wavelength laser in which both wavelengths are generated and amplified by one SOA. Being amplified by the same SOA, the two modes share the same variations caused by changes in refractive index due to changes in temperature and variations in carrier concentration. The carrier concentration fluctuations are due to intensity variations in the laser as well as fluctuations in the electrical current supplied. As a consequence, the variations in the laser longitudinal cavity mode structure for each of the two modes are strongly correlated.

A control system is required in order to be able to control independently the losses of the cavities and consequently the power of λ_1 and λ_2 . Of course, this control system introduces a technical noise source which is different for the two wavelengths, thus, keeping any technical noise originating from these parts at a minimum is critical. We have chosen to exploit PHMs as actuator to balance the power between the two lasing modes. Since the current passing through this type of PHM is typically in the nA to μ A range, low power (in the order of μ W) is needed to control it. As a consequence, the heat dissipation in the PHM is minimal and thermal effects on the laser cavity are negligible. PHMs have been used to create balanced MZIs or MIs to control the losses of each individual channel.

The fact that two modes share a common SOA can lead to instabilities. There are theoretical predictions that even if the laser cavity allows dual-mode lasing operation, the gain medium nonlinearity can forbid simultaneous emission of the two modes. According to Chusseau [1] a stable dual-wavelength regime is possible only when there is a very weak gain competition between the two lasing modes. This means that the modes should be separated in frequency by more than the homogeneous linewidth broadening (in the order of 1 THz). The physical origin of the mode coupling is the short intra-band relaxation time that strongly couples the carrier populations [1]. The quantum well based laser model presented by Chusseau shows that dual-wavelength operation can only occur in a small range of applied injection currents and temperatures. Therefore, Chusseau et al. suggest that stable dual-wavelength operation can most likely not be achieved experimentally if the two modes are separated by less than the homogeneous linewidth of the gain medium which is approximately 1.6 THz for InGaAs QWs with InGaAsP barriers [1, 2].

In this thesis a ring and a linear dual-wavelength lasers are investigated. The ring laser presented in Chapter 4 has been fabricated by the author on a 4QW wafer together with other devices and test structures. The fabrication was based on the standardized generic integration technology developed at COBRA. Minor variations were made to the standardized process flow. The linear AWG-based dual wavelength laser presented in Chapter 5 has been designed by the author and fabricated in a MPW run.

The ring laser operates in a unidirectional mode thanks to the optical feedback provided by the facet of one output waveguide. An SMSR larger than 41 dB can be achieved when the device operates single mode.

Stable dual-wavelength operation has been proven. The demonstration of experimental dual-mode operation of QW based devices with a single SOA represents an important result also considering the laser model presented by Chusseau [1].

A subthreshold analysis and a laser model have been exploited to investigate the behavior of the ring laser. The effect of crosstalk and the phase variation within the channel makes the prediction of the output spectra of the device unpractical since the behavior of the cross-talk and the phase behavior of the fabricated AWG cannot be predicted sufficiently accurately.

The single mode linewidth of the ring laser is 4.0 MHz on a time scale of approximately 100 μ s and drifts over 230MHz on the timescale of seconds. From the optical spectra, no significant enhancement of the linewidth can be noticed when passing from single mode to dual mode operation. This is a first indication that the stability of the dual mode behavior of the ring laser is as good as that of the laser when operating in a single mode.

The linewidth of the laser in single longitudinal mode operation can be improved by applying a stabilization scheme using e.g. a reference etalon and a feedback control signal to e.g. the amplifier. Measurements have shown that a significant improvement of the linewidth should be possible with a control bandwidth limited to 20 kHz since the strongest noise sources are in that frequency range.

In the linear laser presented in Chapter 5, an SMSR larger than 47 dB has been achieved when the device operates single mode. Stable dual-wavelength operation has been proven for all the available frequency ranges between adjacent and non-adjacent channels, confirming the possibility to achieve dual-mode behavior in a device that uses a common SOA to generate and amplify λ_1 and λ_2 .

In the linear laser, PDs connected to the higher order have been used to electrically monitor the power in each individual channel. Future studies can exploit this functionality to control the device using the electrical feedback circuit proposed in section 3.4 of this thesis.

The single mode linewidth of the linear laser is 722 kHz on a time scale of approximately 100 μ s and drifts up to 162MHz on the timescale of seconds. From the optical spectra, no significant enhancement of the linewidth can be noticed when passing from single mode to dual mode operation. Similar as with the ring laser, this is an indication that the stability of the dual mode behavior of the linear laser is as good as that of the laser when operating in a single mode.

The linear configuration of the AWG-based dual-wavelength laser is significantly different from the ring. The impact of the crosstalk on the device is considerably lower than in the ring laser presented in Chapter 4 thanks to the double pass through the AWG (compared to the single pass in the ring laser). This is a considerable advantage of the linear configuration. The designed values for the frequency differences between λ_1 and λ_2 were matched in practice. However, the phase in the AWG channels still makes the automatic control of the device unpractical.

Similarly to the ring laser system, it looks possible to reduce the linewidth of the single mode output of the linear laser using a feedback control system with a control bandwidth limited to 20 kHz using a control on the amplifier.

Further investigations are needed to provide a conclusive answer whether there is an advantage of using a common SOA to generate and amplify two modes. In this study we have demonstrated that there are effects that are dominating the wavelength stability of the devices. Large changes in the output frequency (hundreds of MHz) of the lasers have been observed on long time scales (seconds). Although a clear explanation of this effect has not been found, the fact that it is more pronounced at low frequencies suggests that it is due to technical noise. We can identify at least two sources of technical noise. Firstly, since the control mechanism of the devices is based on PHMs, one important component is the stability of the voltage source connected to the PHM. Fluctuations in voltage will result in variations of the cavity length. To achieve 1 MHz stability in a cavity such as the designs presented in this thesis and with a free spectral range of around 5 GHz, a stability of 1 mV is required. Since the PHM is a diode in reverse bias, it has a high impedance and this will therefore be susceptible to interference which can easily lead to such voltage variations. A second source of noise comes from the fact that there is a photocurrent generated in the PHMs that, for the type of devices presented in this thesis, can reach values in the order of a few milliamps. The carriers involved will create small variations on the phase. Also the contact resistance will create variation on the voltage over the PHMs since these are voltage controlled. These two aspects should be investigated further in the future to demonstrate if the use of a common SOA for two modes is indeed a design choice that can lead to the development of dual-wavelength lasers with better performance of the state-of-the-art devices in terms of phase noise. However, it would seem important to use devices where the two wavelengths in the laser follow the same path at least in the amplifiers as well as in other control elements such as PHMs.

6.2 Second generation of AWG-based dual-wavelength lasers

In order to continue to explore and investigate the possibility to develop dual-wavelength lasers for millimeter wave generation based on an AWG and on a common SOA for two wavelengths, a new generation of devices has been designed. In this section, the two configurations A and B of a second generation AWG-based linear laser are presented. These new configurations have been designed on the predefined active/passive layout presented in section 4.1 and have been fabricated using the process flow described in Chapter 2 during the same fabrication run of the ring laser presented in Chapter 4. Both configurations have been designed with the goal to combine the advantages of the ring and the linear lasers presented in Chapters 4 and 5. Furthermore, configuration B is provided with an Asymmetric MZI (AMZI) and a second AWG placed outside of the laser cavity. This configuration has been designed to allow for on-chip optics stabilization and on-chip analysis of the stability of the lasing modes.

6.2.1 Configuration A of the second generation device

Fig. 6.1 shows the mask layout design of configuration A of the second generation AWG-based linear laser. This layout design contains one laser circuit that can be operated in one of two possible configurations. The schematics of the two possible configurations are depicted in Fig. 6.2a and 6.2b. The schematics are shown separately for clarity: only the AWG, the PDs and the MI construction are shared by both schematics that are combined in a single device presented in Fig. 6.1. One of the differences compared to the linear laser design presented in Chapter 5 is that the laser cavity ends are defined using 1x0 Multimode Interference Reflectors (MIRs) [3]. The use of MIRs allows for designing the device in any position of the so-called usable chip areas on the wafer (see section 4.1), independently from the position of the cleaving areas. For this reason also the length of the laser cavity can be designed more accurately and typically can be designed to be shorter. This increases the cavity mode spacing which in turn can improve the tuning range and the side mode suppression ratio of the laser output.

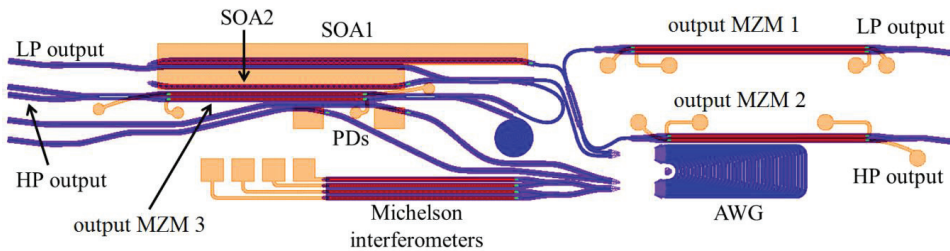


Fig. 6.1. Circuit layout design of the configuration A of the new generation AWG-based linear laser. The layout combines the schematics depicted in Fig. 6.2.

The light is coupled out from the laser cavity using a 2x2MMI similarly to what is done in the ring laser presented in Chapter 4. In this way it is possible to place an output MZ modulator. Such a

modulator is not present in the linear design of the previous generation (section 5.1). The 2x2MMI is placed in the waveguide that connects the AWG to the common SOA. This design choice has been selected in order to have the higher possible output power from one of the output waveguides. Indeed, the output waveguides indicated with HP (high power) in Fig. 6.1 and 6.2 transmit the light right after that this has gone twice through the SOA. This is expected to lead to higher power from the laser compared to the design used in the previous generation. The outputs named as LP (low power) should provide a lower level of output power compared to the HP output due to the passive losses of AWG and MIs. Only two individual channels are present in this device in order to make the control slightly easier.

A different design has been adopted also for monitoring the power of the two wavelengths through the waveguides connected to the higher order of the AWG. As for the first generation laser designs, the waveguides are connected to PDs, but in the second generation designs they cross the photodetectors and reach the facet of the chip. In this way, the signals travelling through the waveguides used for monitoring can be checked both electrically and optically. If needed, the PDs can be forward biased and used as amplifiers to increase the signal power.

With reference to Fig. 6.1, the two SOAs connected to the AWG at different wavelengths are included similarly to the four amplifiers used in the laser described in Chapter 5. The SOAs have different lengths (SOA1 is 3 mm long whereas SOA2 is 2 mm long). In this way, two independent device variations are available on the same chip. This choice provides a back-up solution in case of damaging of one of the waveguides where the SOAs are placed. Furthermore, the choice to use one SOA or the other presents an option to choose the optimal AWG channel with respect to the SOA gain spectrum.

The AWG used for the second generation devices has the same design of the one used for the ring laser presented in Chapter 1.

Three output MZ data modulators are present in the device: output MZM 2 and MZM 3 are on HP output waveguides whereas output MZM 1 is placed on LP output waveguide. The second LP output waveguide is directly connected to the facet of the chip. Output MZM1 and MZM2 are connected to the cavity of SOA1. 2x1 MMIs (45 μm long) are used in MZM 1 and 2 because of space limitations. The use of 330 μm long 2x2 MMIs would not allow for having sufficiently long PHMs. The output MZM 3 modulator that is connected to the cavity of SOA2 has been designed using 2x2 MMIs since more space is available in that part of the chip. This output MZM provides two output waveguides due to the use of 2x2 MMIs. To be noticed is that one of the ports of the input 2x2 MMI of this output MZM has been connected to a long deeply etched spiral in order to terminate the waveguide from this port.

For similar reasons, the MI structure has been designed using 1x2 MMIs. In this case, although there is sufficient room to place 2x2 MMIs, there is not enough to place spirals or to design output waveguides in order to lose the light that would be coupled in the spare ports of the 2x2 MMIs.

Differently from the first generation linear laser, the number of individual channels has been kept at the minimum of two in order to simplify both the monitoring and the control operations.

The length of the PHMs used in the MZ modulators varies from 1560 μm (MZM 3) 1574 μm (MZM 2) and 1868 μm in MZM 1. All the output waveguides reach the facet of the chip through a mode filter and a taper from 2 μm to 3.5 μm combined with a 7-degree angle of the waveguide with the normal of the facet in order to reduce back-reflections to the laser cavity.

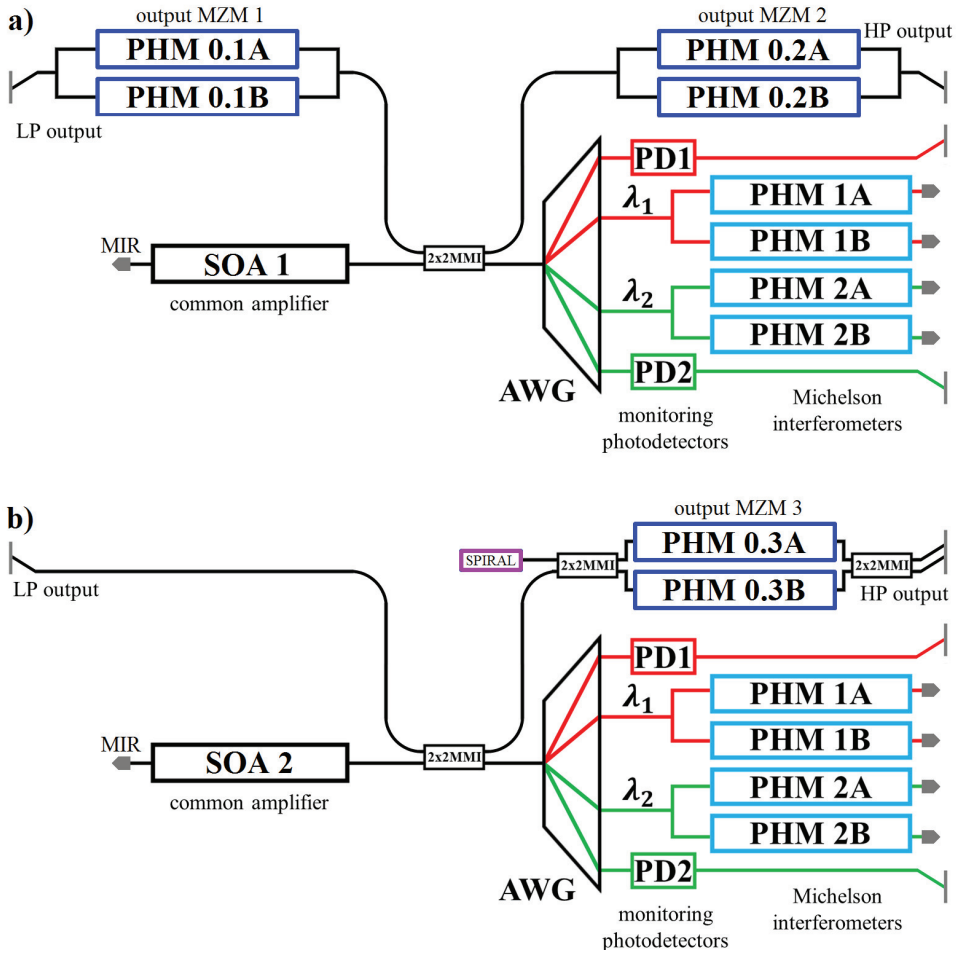


Fig. 6.2. Schematics of the lasers that are combined in a single circuit layout presented in Fig. 6.1. In the layout, the AWG, the PDs and the MI construction are shared by both a) and b) laser.

6.2.2 Configuration B of the second generation device

In Fig. 6.3a the schematic of configuration B of a new generation linear laser is depicted. This configuration has been designed to further investigate the linewidth and the stability of the lasing modes, especially when the device operates in dual-mode. The slope of the filtering function of the AMZI can be used to translate frequency fluctuations into power variations. Alternatively, the slope of the filtering function can be exploited in the following way: one of the modes can be locked at the top of the filtering function of the AMZI and the frequency/power translation provided by the slope is used to monitor the other mode and then tune it in order to keep the frequency difference constant.

The AMZI is connected to a second AWG which is used to separate the two lasing wavelengths into two separate output waveguides. Each output waveguide passes through a PD and then reaches the facet of the chip. This device can be used to analyze separately the linewidth and the stability of the two lasing modes when the device operates in dual-mode. However, in order to be able to split the two modes into the two output waveguides, the second AWG must be close to identical to the first one that is used as intra-cavity filter inside the laser cavity of the device.

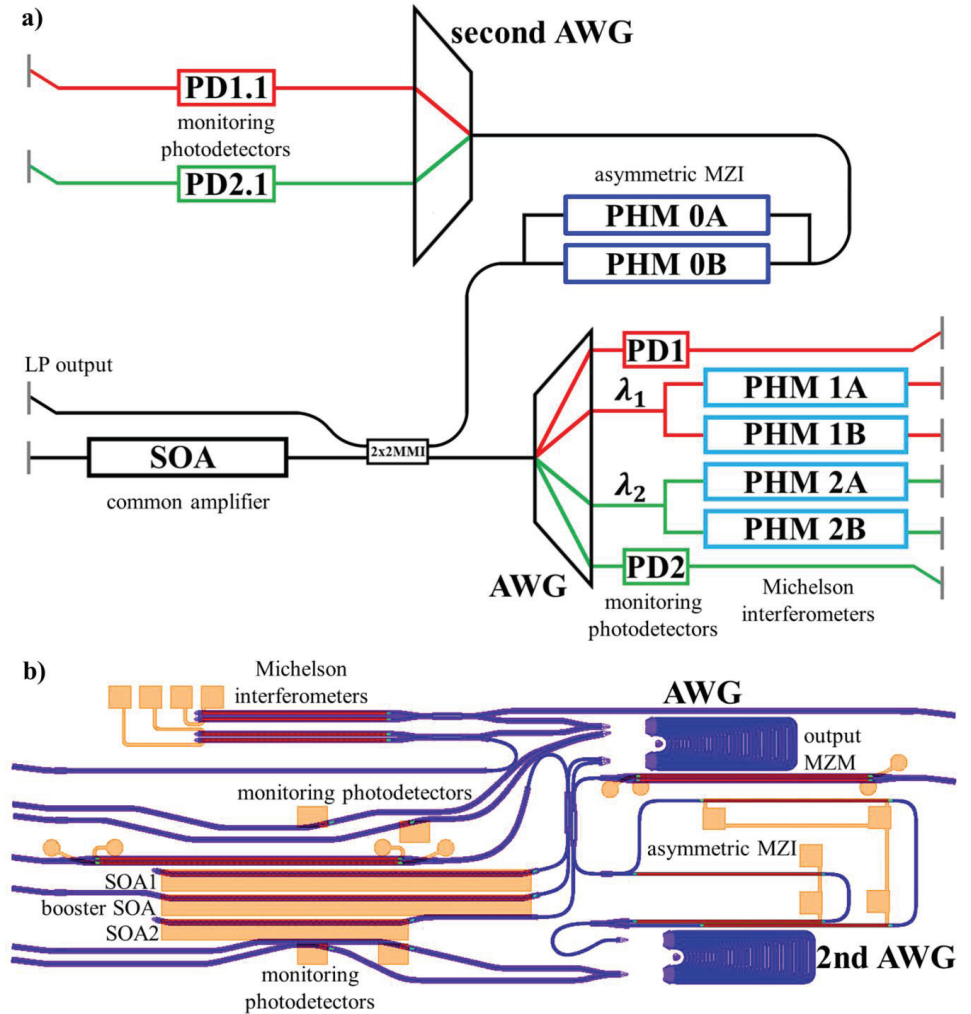


Fig. 6.3. a) The block schematic of configuration B of the second generation linear laser is depicted. This configuration has been designed to further investigate the linewidth and the stability of the lasing modes, especially when the device operates in dual-mode. b) Circuit design: few extensions can be noticed if compared to the block schematic.

The circuit design (mask lay-out) of the second configuration is shown in Fig. 6.3. A few extensions can be noticed compared to the schematic. Firstly, as with the layout in Fig. 6.2, two SOAs are present to give a choice of laser cavities (both SOA1 and SOA2 are 3 mm long). Secondly, the HP output waveguides from each of the two possible linear configurations are provided with MZMs. Thirdly, the LP output is provided with a 3 mm long booster SOA. Furthermore the MI construction is built using 2x2 MMIs. In this case enough room was available to use these longer MMIs and to design output waveguides to transport the light from the spare ports of the MMIs to a chip facet. These outputs can provide information to simplify the characterization of the device.

Also in this configuration, all the output waveguides reach the facet of the chip through a mode filter and a taper from $2\ \mu\text{m}$ to $3.5\ \mu\text{m}$ combined with a 7-degree angle of the waveguide with the normal of the facet.

Both configurations have been combined on a 2-inch wafer mask design set together with other device designs and have been fabricated by the author.

6.3 Dual-wavelength laser based on asymmetric Mach-Zehnder interferometers

The use of an AWG as intra-cavity filter in a dual-wavelength laser where one SOA generates and amplifies both lasing modes presents the advantages listed in section 6.1. As a consequence, it is worth to further investigate in this direction. However, the coarse tuning between the two wavelengths depends strictly on the channel spacing of the AWG. Furthermore, a rather complicated control mechanism is required in order to achieve dual-wavelength operation.

An alternative principle can be derived from an integrated tunable laser scheme originally proposed for gas detection. In recent studies [4, 5], a laser wavelength tuning mechanism based on AMZIs is presented. In this scheme, the optical path length unbalances are controlled with phase shifters allowing for a tuning range in the order of few terahertz. The configuration with three AMZIs in series requires a small number of control elements and it has been designed in order to achieve single mode operation of the laser.

The laser presented by Latkowski [4, 5] has a geometry as schematically depicted in Fig. 6.4. It consists of an SOA providing optical gain, the AMZI-based wavelength selective filter and an MMI for coupling out the optical signal. All elements are connected with straight and curved passive waveguides forming an extended ring cavity.

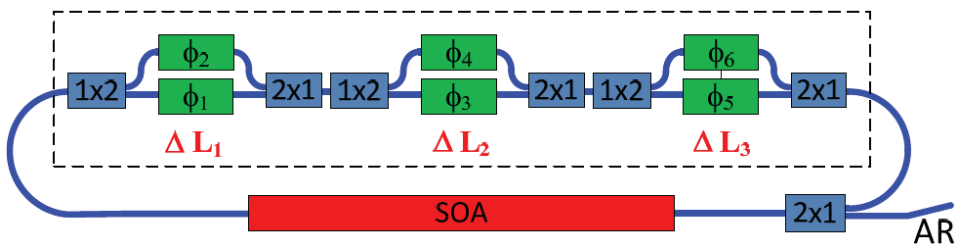


Fig. 6.4. Block schematic of the AMZI-based laser as presented by Latkowski [4, 5].

In this device, the wavelength filter consists of three AMZIs in series. Each AMZI has a different unbalance as indicated in Fig. 6.4 and is equipped with PHMs in both arms. The FSR of each of the three MZIs is therefore different. The transmission peak of each of the AMZIs can be tuned over one full FSR by a change of the optical phase difference between the arms by 2π .

The mode selection derives from the superposition of the three filter functions of the AMZIs with the cavity modes. Fig. 6.5 presents a simulated output spectrum of the AMZI-based laser at threshold (red line) over a limited wavelength range. The blue line represents the total filtering function of the three AMZIs. The filter can be tuned in such a way that two longitudinal modes, separated by the FSR of the AMZI with the largest unbalance, have the same power.

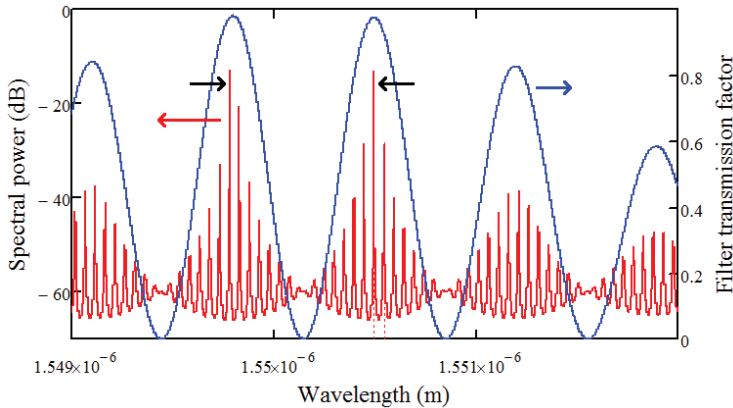


Fig. 6.5. Simulated output spectrum of the AMZI-based laser at threshold (red line). The blue line represents the total filtering function of the three AMZIs. The filter can be tuned in such a way to obtain two longitudinal modes having the same power (indicated by the black arrows).

An AMZI-based dual-wavelength laser design would have the advantage to avoid the presence of the AWG that has in practice a complex transmission function. The phase behavior in the AMZI is much simpler than that of an AWG and it is fully predictable except for a simple offset-value. A big advantage of this laser design is that both laser modes share the same waveguides everywhere so disturbances in the amplifier and the waveguides should have a very limited influence on the frequency difference.

In short, this type of device is promising for dual-wavelength operation, although other disadvantages should be taken into account: by design, the tunability, for instance, is not continuous. For these reasons, we suggest further investigation in this direction.

References

- [1] L. Chusseau, F. Philippe, P. Viktorovitch and X. Letartre, "Mode competition in a dual-mode quantum-dot semiconductor microlaser", *Physical Review A*, vol. 88, no. 1, 015803, July 2013.
- [2] L. Chusseau, F. Philippe, and F. Disanto, "Montecarlo modeling of the dual-mode regime in quantum-well and quantum-dot semiconductor lasers", *Optics Express*, vol. 22, no. 5, 2014.
- [3] Kleijn, Smit, Leijtens, "Multimode interference reflectors: A new class of components for photonic integrated circuits," *J. Lightw. Technol.*, vol. 31, no. 18, pp. 3055–3063, 15 September 2013.

- [4] S. Latkowski, M.K. Smit and E. Bente, “Integrated Tunable Semiconductor Laser Geometry Based on Asymmetric Mach-Zehnder Interferometers for Gas Sensing Applications”, in the Proceedings of the 2012 Annual Symposium of the IEEE Photonics Society Benelux Chapter, Mons, Belgium, 29-30 November 2013.
- [5] E. Bente, S. Latkowski, T. de Vries, M.K. Smit, “Widely tunable monolithically integrated lasers using intracavity Mach-Zehnder interferometers”, 2014 16th International Conference on Transparent Optical Networks (ICTON), pp.1–4, 6-10 July 2014.

Summary

Monolithic integrated dual-wavelength laser for millimeter-wave generation

The work presented in this thesis concerns research on dual-wavelength lasers that are suitable as a light source for an optical-based millimeter wave (mmW) generation system. Optical integration technology based on indium phosphide (InP) semiconductor material appears to be a promising technology for realizing dual wavelength lasers that can satisfy the requirements imposed by the mmW application. The research work resulted in the realization of several InP-based monolithically integrated dual-wavelength lasers in the 1550nm wavelength region and an assessment of the capabilities of these devices.

In an optics-based millimeter wave source, the light generated by the dual wavelength laser source is directed towards a high speed photodiode. The photodiode rectifies the optical signal beating between the two laser modes. This results in a millimeter wave electric signal that has a frequency equal to the difference between the two optical frequencies. This electrical signal can be coupled to a transmitting antenna. The most critical requirements for the laser system derive from the requirements on the stability of the frequency and power of the mmW signal. In order to minimize the phase noise, the frequency difference between the two lasing modes generated by the optical source must be controlled and kept as stable as possible.

The goal of this study is to investigate dual-wavelength lasers which were designed to try to have nearly identical frequency fluctuations of the two generated wavelengths λ_1 and λ_2 . We designed lasers in which both wavelengths have an accurately controlled frequency difference and both wavelengths are generated and amplified by one common semiconductor optical amplifier (SOA). This is expected to reduce the noise in the frequency difference between the two modes and consequently reduce the phase noise of the millimeter wave.

The laser designs used an Arrayed Waveguide Grating (AWG) as an intra-cavity filter to coarsely set and combine the two lasing wavelengths in a common optical amplifier. The designs contain electronically controlled interferometers in two separate channels of the device to fine tune the wavelengths and to actively equalize the power between λ_1 and λ_2 . Integrated photodetectors monitor the power of the two wavelengths. Both ring and linear configurations have been realized using a standardized optical InP fabrication process.

Relatively stable dual-wavelength operation has been demonstrated for several frequency difference ranges (60 GHz, 120 GHz, 200 GHz) in both linear and ring laser configurations.

Characterization of the lasers has demonstrated that other noise sources than expected dominate the frequency noise and active stabilization of the two wavelengths is required. Also the use of an AWG as a wavelength selection led to a much more complex control problem for the power and tuning of the two lasing modes than expected. In particular, theoretical analysis of the laser cavity shows that the crosstalk between the channels of the AWG and the non-uniform phase delay within a single AWG channel makes that the ring laser configuration is unsuitable for AWG-based dual-wavelength lasers despite other advantages. The linewidth and the stability of the lasing modes over different time ranges have also been studied. An electronic feedback circuit to automatically balance the power of the two wavelengths, exploiting the signals extracted from the monitoring photodetectors is proposed and analyzed.

On the basis of the results obtained, new designs for monolithically integrated dual-wavelength lasers are proposed.

In Chapter 1, the state of the art of semiconductor-based dual-wavelength laser is reported together with the motivation for the present work. The choice of using a single Semiconductor Optical Amplifier to generate and amplify both wavelengths is described. Furthermore, the requirements for the development of dual-wavelength lasers at TU/e in the frame work of the FP7 iPHOS project are listed (e.g., the use of an Arrayed Waveguide Grating).

In Chapter 2, the active-passive integration technology process used to fabricate the devices presented in Chapters 4 and 6 of this thesis is explained. The fabrication is based on the standardized generic integration technology developed at COBRA. Minor variations that were made to the standardized process flow are discussed. The last section of Chapter 2 describes the mounting and the wire-bonding of the chips implemented in order to simplify the characterization of the devices in the lab.

In Chapter 3, the main design choices for the devices presented in Chapter 4 and Chapter 5 are presented. Both linear and ring configurations are discussed. The advantages of exploiting an AWG as intra-cavity filter are listed. Constructions based on voltage controlled electro-optic phase modulators are used for fine tuning and for controlling the power of the two modes. On chip photodetectors are designed to monitor the power of λ_1 and λ_2 . A feedback control circuit which exploits the signals extracted from the photodetectors is proposed.

A series of dual mode ring lasers has been designed based on the calculations presented in Chapter 3 and has been fabricated by the author. In Chapter 4, we focus on the experimental results obtained from one of these dual mode ring lasers. In order to analyze the performance of the laser it was necessary to develop the theoretical description of the laser further.

A linear AWG-based dual wavelength laser has been designed and fabricated in a Multi-Project Wafer run. Chapter 5 focuses on the characterization results of this linear laser. Dual wavelength operation is demonstrated. The advantages and disadvantages of this configuration compared to the ring laser presented in Chapter 4 are described and discussed.

In Chapter 6, the results obtained from the devices presented in Chapter 4 and 5 are summarized. Two design configurations of new generation AWG-based devices are presented. The goal of the new generation devices is to combine the advantages of the linear and the ring laser presented in the previous chapters. Finally, an alternative design based on asymmetric MZIs instead of an AWG is presented.

Acknowledgments

The PhD is of course not only a professional experience but also a gym for life. You need motivation, stamina and focus to go through tough periods and, at the same time, you should find the way to celebrate achievements, be proud of the results and appreciate the learning process, day by day. I have been extremely lucky being surrounded by people who always reminded me to enjoy my time while keeping on working hard.

The first thanks go to my supervisor, Erwin Bente, who was always present, during the week and during the weekend, to guide me through these years. Erwin, I genuinely admire your devotion and the effort that you demonstrate every day in your job. Thanks for all the explanations and for the support. I am really glad that we always had sincere and transparent discussions both about work and life.

I want to thank Meint Smit who wonderfully coordinated the OED-PhI group during the years. Your motivation has inspired all of us. You are a great leader and you have been able to pass your enthusiasm for photonics to all the people who have been part of the group.

I continue with the technicians that are the owners of all the secrets of the cleanroom. Your work is really a key strength for the development of the PhI group. Barry, thank you for all the interesting explanations that you gave me about chemicals, photoresists, sputtering and plating. Thank you for the extensive wire-bonding work that you did for me: I know that I gave you, let's say, the opportunity to challenge and broaden your skills. Tjibbe, thank you for the positive attitude that you transmitted to me: you taught me how to keep on smiling when things do not go in the right direction during a "standardized" COBRA fabrication. You and Barry literally saved my PhD when my wafer got stuck to the mask during my second fabrication. And thanks for the fun that we had playing with the vOEDball team: I miss it a lot. Jeroen, thank you for your patience: you have been willing to answer tens of questions per day. We had a lot of fun making jokes in the cleanroom and this has made the time much more enjoyable. Erik-Jan, thank you for taking care of the ICP and the FC2000 as they were babies: you taught me the proper way of working in a cleanroom. And thanks for your availability on Saturday morning to replace the gold in the FC2000 to allow my expensive evaporations. Staying in the cleanroom, I want to thank Huub for addressing my complaints and for striving every day for improving the quality of the cleanroom: you really did an amazing job. And thanks to Luc: I learned a lot working side-by-side with you, Peter and Boudewijn.

I want to thank Jos: you were the first person in the group that I had contact with in 2008. You forwarded my email to Jose and that day my adventure at TU/e began. Thanks for all your smart questions and suggestions about my work and for all the discussions about Italy and football.

Going back in time, of course my thanks go to Jose who has been my first supervisor at TU/e during my Master project. You gave me the time to learn and you passed your passion for photonics to me. It is thanks to you and Pietro that I decided to apply for a PhD position. Pietro, you were the only Italian in the group when I joined it in 2009 and you really inspired me. You have always

found the way to give me valuable suggestions both in person and by email: I hope to be able to visit you soon in California.

I really have to thank Xaveer for his support during the preparation of all my GDS file and for all the discussions about the different AWGs available on the different platforms. Thanks for your positive attitude and your friendly way of working.

I will never forget the support that I received from Saeed and Sylwester: your presence in the OLA was a treasure. You have always been willing to stay until late in the lab to help me to complete my measurements: I really appreciate this.

I also want to thank Bauke who guided me during my first device design: it has been very important for me to have you in the group when I started my PhD.

Thanks to Valentina: we spent a lot of time one opposite to the other (with two computer screens in the middle). You are a really smart and working-hard person: I really enjoyed sharing the office with you and I am sure you have a brilliant future in front of you.

I continue with Aura: although you spent too much time in the cleanroom when I was in the office and vice versa, it has been wonderful to share with you good and tough moments. You were always smiling and this really had a positive impact on me. Remember to thank me for the hand cream when you finish your thesis.

And then Rui: thanks for the fun that we had in the office when Aura and Valentina were completely absorbed in their tasks. And, of course, thanks for your help in the OLA, especially with the linewidth measurement setup.

I will never forget Elton, Giovanni and Domenico: during the toughest period I could just walk to one of you and have some chat just to cheer up and have the feeling that we were all supporting each other. Giovanni, thank you for the coffee (I probably still owe you some money). Elton, I want to thank you for the experience that we shared being part of the IEEE Photonics Student Board. Domenico, thanks a lot for the fun that we had in Nice: I really hope that you will decide to stay in Eindhoven.

Also many thanks to Josselin: we spent quite some time together in the cleanroom. Thank you for listening to my (broken-)french songs.

Special thanks to Kasia: we laughed a lot together and I really appreciate the fact that you pushed me to give my best and complete my thesis as soon as possible.

And, of course, I want to thank all the other people who have been members of the OED/Phi group during these years: Alonso, Dan, Deepak, Dima D., Dima P., Dominik, Emil, Hadi, Jing, Jolanda, Kevin, Longfei, Manuela, Milan, Robert, Srivathsa, Staszek, Vadim, Victor, Weiming, Yuqing and all the other new and old members.

Further thanks to the members of ECO and PSN groups: I was really happy to collaborate with you in the cleanroom and in the optical labs.

Not to forget are the members of the iPHOS project. I learned a lot from all of you: meetings and discussion were always useful and fruitful. Special thanks to Guiller: I will never forget the dinners we had all around Europe during conferences and project meetings. And thanks for the clever comments that you had on my thesis.

Now I turn to my personal life (and to Italian language).

Grazie mamma e papa per aver accettato la mia scelta di lasciare l'Italia, per esservi preoccupati che io stessi bene e per avermi sempre ricordato che la porta di casa è aperta, in ogni

momento. Mi avete reso molto felice quando siete venuti a trovarmi. Anche se ve l'ho detto troppe poche volte, mi mancate tanto.

Naturalmente ringrazio anche mia sorella e mio fratello. Grazie per la stima che avete in me e per i tanti consigli che mi date. Grazie perchè per voi sono sempre il fratellino piccolo.

Un ringraziamento speciale alle mie nipoti: Alice, Arianna e Margherita. Ogni volta che torno in Italia il vostro sorriso mi riempie di gioia. Mi dispiace non vedervi crescere ogni giorno, ma è stupendo scoprire che siete sempre felicissime di rivedere vostro zio.

Grazie, grazie e ancora grazie a mia nonna. Sei un punto di riferimento ed un esempio da seguire per tutti i tuoi nipoti. Grazie per l'affetto che mi dimostri al telefono e ogni volta che vengo a trovarvi. Grazie per le mille domande sull'Olanda e sugli olandesi.

Voglio poi ringraziare mia cugina Lucia. Grazie per esserci sempre stata quando ho avuto bisogno e grazie per avermi cercato anche quando io non l'ho fatto. E grazie a Carlotta per i tanti sorrisi via skype.

Rimanendo in Italia, ringrazio anche tutti i miei amici di Modena e Nonantola: riuscite sempre a farmi sentire a casa, come se nulla fosse cambiato, come se io non fossi mai partito.

Ed ora passiamo ai miei compagni di avventura qua ad Eindhoven. Elisa, Alberto e Daniel: non trovo davvero le parole per ringraziarvi. Grazie per i tantissimi pranzi alla TU/e, le infinite conversazioni su skype, le mille chiacchiere e le splendide cene. Grazie per avermi sempre ascoltato e grazie per tutte le volte che abbiamo riso insieme. Elisa, grazie per il sorriso che riesci a mettere a chiunque ti incontri, grazie per i preziosissimi consigli, grazie per l'accoglienza che dimostri a chiunque entri nella tua vita e grazie per essere un'amica di inestimabile valore, davvero. Grazie per tutte le volte che ci sei stata, in particolare per quella fetta di torta a metà pomeriggio di domenica. Alberto, prima di tutto: ci manchi molto qua in Olanda perciò tu e Marthe siete pregati di tornare al più presto. Grazie per essere sempre stato il primo a farsi sentire, sia qua ad Eindhoven, sia dopo esserti trasferito in Inghilterra. Grazie per la tua genuinità, per la tua saggezza e per la tua capacità di capirmi. Grazie perchè so di poter contare su di te in ogni momento. Daniel, grazie perché riesci sempre a sdrammatizzare ogni situazione con una battuta, ricordandomi che c'è sempre un motivo per sorridere. Grazie per tutte le volte che abbiamo gioito e sofferto insieme per una partita di calcio. Grazie per i tuoi consigli dai quali ho imparato molto, per l'ospitalità a Laives e per avermi fatto una stupenda sorpresa insieme a Marina all'aeroporto di Eindhoven.

Grazie mille a Luca: siamo diventati coinquilini quasi per caso nella mitica HS5 ed è stato un immenso colpo di fortuna. Grazie per tutte le partite a calcetto, per le serie tv e per tutte le volte che mi hai invitato a cena. Ma soprattutto, ti ringrazio per le nostre lunghe conversazioni, per i nostri onesti confronti da cui sono sicuro che entrambi impariamo tanto. Grazie davvero per la nostra amicizia.

Non posso ovviamente dimenticare Floriano: tutto ciò che è iniziato ad HS5 è stato grazie a te. Ti ringrazio per il tuo modo sempre allegro di affrontare la vita: mi hai sempre trasmesso voglia di fare e di esplorare. Ad Eindhoven sarai sempre il benvenuto.

Talking about housemates, I want to sincerely thank Tom. You are much more than my Mo-Bro. Thanks for your effort to learn a few words in Italian and thanks for answering all the questions that I had (and will have) about English. When you come to visit us in Eindhoven, I always have the feeling that you never left and I actually hope that you will be back in NL sooner or later.

Let's continue with the other friends. Juan Carlos, thank you for introducing me to the amazing world of the half-marathons: as you know it is my new passion and soon it will be also time to try cycling. Of course, I will join you and Raymond, my amazing flat mate. Raymond, thanks for all the jokes that you make on daily basis, for the balcony time during the weekend, for the concerts and, much more, for the deep discussions that we had (we will enjoy Palazzo also without Daniel).

Marina, thanks for being always smiling and positive and active and so on: you always bring happiness to Palazzo. I sincerely admire your attitude.

Maja, thanks for the fruitful discussions that we had about meditation, life and books: we should definitely talk more often.

And thanks to all the people who have been members of the Happy Dogs: barking, wagging and drinking with you has been simply marvelous.

Well, then I have to thank also the members of my second team: the Ragtag Rebels. All the trainings and the matches have been an extraordinary opportunity to remind myself that life is not only about working.

Ci sono poi amici che ho incontrato ad Eindhoven, ma che ora sono in altre parti d'Europa. Tra questi, voglio ringraziare di cuore Giulia e Robi. Grazie perché mi sembra di conoscervi da sempre. Grazie per tutte le volte che ci siamo ritrovati in Olanda, Svizzera e Italia. Grazie per le interminabili chiacchierate via skype e per esservi sempre preoccupati che io fossi felice. Ho davvero grandissima stima di voi.

E, infine, la persona più importante di questi anni, Daniela. Sono davvero innumerevoli i motivi per i quali ti devo e ti voglio ringraziare. Grazie per avermi supportato nella scelta di investire anni della mia vita in un PhD. Grazie per avermi spinto ad uscire dalla mia "comfort zone". Grazie per avermi motivato e spronato a dare il meglio di me, a migliorarmi e a mettere a frutto le mie potenzialità. Grazie per avermi capito nei momenti di difficoltà. Grazie per essere stata dura e chiara quando io mi intestardivo. Grazie per avermi coccolato quando mi sentivo senza forze. Grazie per aver vissuto ogni gioia e ogni delusione di questo PhD come una cosa non solo mia, ma nostra. Grazie per avermi chiesto persino i dettagli del mio lavoro e grazie per esserti sforzata di capire gli aspetti più tecnici e complicati della mia ricerca. Grazie per la fiducia e per la stima. C'è poi un intero mondo che va ben oltre queste poche righe e ben oltre questi anni... e ce lo teniamo per noi.

Curriculum Vitae

Antonio Corradi was born on 24-05-1984 in Modena, Italy. He studied Electronic Engineering at Università degli Studi di Modena e Reggio Emilia in Modena, Italy. In 2009 he carried out his Master project in the Opto-Electronic Devices group (OED, now renamed as PhI) at the Eindhoven University of Technology. In 2010 he graduated within the OptoLab group of Università degli Studi di Modena e Reggio Emilia on opto-electronics. The same year he started a PhD project in the Photonic Integration group (PhI) at the Eindhoven University of Technology of which the results are presented in this dissertation. Since January 2015 he is a member of Engineers Without Borders of The Netherlands and since March 2015 he is employed as Imaging Design Engineer at ASML, Veldhoven.

Publications

A. Corradi, G. Carpintero, E. Smalbrugge, M.K. Smit and E.A.J.M. Bente, “*Characterization of an AWG-based dual-wavelength ring laser,*” 17th European Conference on Integrated Optics (ECIO), Nice, France, June 2014.

A. Corradi, G. Carpintero, M.K. Smit and E.A.J.M. Bente, “*Integrated dual-wavelength AWG laser for sub-terahertz wave generation,*” 18th Ann. Symp. IEEE Photonics Society Benelux Chapter, Eindhoven, The Netherlands, November 2013.

A. Corradi, G. Carpintero, E. Smalbrugge, M.K. Smit and E.A.J.M. Bente, “*Characterisation of monolithically integrated dual wavelength AWG-lasers for mm-wave generation,*” 17th Ann. Symp. of the IEEE Photonics Society Benelux Chapter, Mons, Belgium, November 2012.

A. Corradi, G. Carpintero, B.W. Tilma, M.K. Smit and E.A.J.M. Bente, “*Integrated dual-wavelength semiconductor laser systems for millimeter wave generation,*” ISLC 2012, San Diego, California, USA, October 2012.

A. Corradi, G. Carpintero, B.W. Tilma, P.J. Thijs, M.K. Smit and E.A.J.M. Bente, “*Integrated dual-wavelength AWG-lasers for millimeter wave generation,*” 16th European Conference on Integrated Optics (ECIO), Sitges, Spain, April 2012.

A. Corradi, G. Carpintero, B.W. Tilma, P.J. Thijs, M.K. Smit and E.A.J.M. Bente, “*Integrated dual wavelength lasers for millimeter wave generation,*” 16th Ann. Symp. of the IEEE Photonics Benelux Chapter, Ghent, Belgium, December 2011.

M.K. Smit et al., “*An introduction to InP-based generic integration technology,*” Semiconductor Science and Technology, 29(8):083001, 2014.

J. Pozo, A. Corradi, E. Smalbrugge, T. De Vries, M.K. Smit, D. Lenstra, R. Nötzel, “*Quantum Dot Twin Stripe Lasers as Emitter and Receiver in Chaotic Encrypted Communication Systems,*” 14th Ann. Symp. of IEEE Photonics Benelux Chapter, Brussels, Belgium, November 2009.

J. Pozo, A. Corradi, E. Smalbrugge, T. De Vries, M.K. Smit, D. Lenstra, R. Nötzel, “*Quantum-Dot InAs/InGaAsP/InP (100) Twin-Stripe Lasers for Secure Encrypted Communication*,” 2nd Chaotic Modelling and Simulation International Conference, Chaos 2009, Greece, June 2009.

R.C. Guzman, A. Jimenez, K. Lawniczuk, A. Corradi, X.J.M. Leijtens, E.A.J.M. Bente and G. Carpintero, “*Dual-wavelength operation of monolithically integrated arrayed waveguide grating lasers for optical heterodyning*,” Proc. SPIE 8781, Integrated Optics: Physics and Simulations, Prague, Czech Republic, April 2013.

R.C. Guzman, L.J. Orbe, G. Carpintero, A. Corradi, and E.A.J.M Bente, “*Traveling wave model of an AWG-based multiwavelength laser*,” 16th European Conference on Integrated Optics (ECIO), Sitges, Spain, April 2012.

G. Carpintero, K. Balakier, Z. Yang, R.C. Guzmán, A. Corradi, A. Jimenez, G. Kervella, M.J. Fice, F. van Dijk, C. C. Renaud, A. Wonfor, E.A.J.M. Bente, R.V. Penty, I.H. White and A. J. Seeds, “*Microwave Photonic Integrated Circuits for Millimeter-Wave Wireless Communications*,” IEEE Journal of Lightwave Technology, vol. 32, issue 20, May 2014.